UNIVERSITAT POLITÈCNICA DE CATALUNYA
BARCELONATECH

MASTER THESIS

Characterization and Improvement of Thrust Balance Measurement Technique for SX3 Applied-Field Magnetoplasmadynamic Thruster

Akash Mankar

SUPERVISED BY

Jordi L. Gutiérrez

Universitat Politècnica de Catalunya

Dr.-Ing Georg Herdrich
Adam Boxberger
Institute for Space Systems, University of Stuttgart

Master in Aerospace Science & Technology
December 2018

This Page Intentionally Left Blank

Characterization and Improvement of Thrust Balance Measurement Technique for SX3 Applied-Field Magnetoplasmadynamic Thruster

BY

Akash Mankar

DIPLOMA THESIS FOR DEGREE

Master in Aerospace Science and Technology

AT

Universitat Politècnica de Catalunya

SUPERVISED BY:

Jordi L. Gutiérrez
Department of Physics
Universitat Politècnica de Catalunya

Dr.-Ing Georg Herdrich
Adam Boxberger
Institute for Space Systems, University of Stuttgart

This Page Intentionally Left Blank

To my new wisdom tooth...

(Pretty sure it grew out due to new found wisdom in electric propulsion!!!)

ABSTRACT

Steady state applied-field magnetoplasmadynamic thruster promises good compromise between thrust density and specific impulse, making them relevant for interplanetary missions requiring high thrusts. The IRS $100\ kW$ gas-fed steady-state AF-MPD SX3 thruster has shown promising results in previous held test campaigns. Experimental results in those campaigns showed non-linear behavior of tare forces, resulting in respective error in the thrust measurement and this error then propagates in further calculation of Isp, thrust efficiency, etc. This motivated improvement in the thrust balance and measurement technique. Various error sources in the thrust measurement technique were identified and solutions to mitigate them were presented. A number of changes in the thrust balance were made in order to improve the measurement technique and data quality. The effectiveness of improvements had been experimentally characterized and presented. Previously the thrust measurement technique featured manual control of the measurement setup which led to complex and inconsistent test procedures. A new programmable electronic control unit was specifically designed for more consistent and automated measurement and calibration procedure. Potential error sources of the measurement chain have been systematically identified, characterized and discussed. The analysis tool for thrust characterization was redesigned which gives fine control of the interval selection and data export, this ensured accurate thrust and calibration calculations. The new code is more modular to adapt for changes and is very flexible with user interaction reducing complexity while still retaining the functionality. To further improve the measurements accuracy some suggestions are made.

ACKNOWLEDGEMENTS

I would like to acknowledge my indebtedness and render my warmest thanks to my supervisors, Dr.-Ing Georg Herdrich, Adam Boxberger and Jordi L. Gutiérrez, who made this research possible. Their guidance and help have been invaluable throughout all stages of the work.

I wish to express my undying gratitude to Adam Boxberger who constantly kept me pushing to reach the goals and mentored me on every step of the research. I also wish to thank Partho Upadhyay who constantly engaged in lengthy and detailed discussions out of the scope of my thesis so I can better understand the research. I also want to thank every member of electric propulsion group who entertained my queries and showed me around their setup. This research has been fundamental milestone in determining my career goal.

Special thanks are due to my family for their continuous support and understanding during this long research. Their encouragement kept me going. I want to extend my thanks to all my friends for their constant motivation.

This thesis has been possible because of the Erasmus Exchange program, I sincerely thank the administrative staff of both the universities, because of them the exchange was possible and the transition was smooth.

Stuttgart December 15th, 2018.

Akash Mankar

Table of Contents

List of Symbols

Sign	Description	Unit
B	Magnetic Field Strength	T
F	Force	Newton
P	Power consumption	kW
V	Voltage	Volt
$\dot{m}$	Mass flow rate	mg/sec
π	Geometrical value	
h	Height of tower	m

Acronyms

μC Microcontroller

DAC Digital to Analog Converter

DAQ Data Acquisition System

DOF Degrees of freedom

FEEP Field-Emission Electric Propulsion

FS Full Scale(refers to full scale measurement of device)

GND Electrical Ground

IRS Institute of Space Systems(IRS), Stutgart, Germany

MHD Magnetohydrodynamic Theory

MIPS Million Instructions per Second

MPD Magnetoplasmadynamic Thruster

PCB Printed Circuit Board

PID ProportionalIntegralDerivative Controller

PWM Pulse Width Modulation

SPI Serial Peripheral Interface

UART Universal Asynchronous Receiver/Transmitter

List of Figures

List of Tables

Chapter 1

Motivation

Future manned and heavy cargo missions, for example an establishment of Martian base, will require power sources in MW power range and high power electric propulsion concepts.Here for, based on manned Mars mission analysis a thrust of $100\ N$ and specific impulse of $3000\ s$ will be required [24].

Thrust of a rocket engine is given by classical equation,

$$T = \dot{m} u_e. \tag{1.1}$$

where, $\dot{m}$ is the rate of change of rocket mass by exhaust of propellant and u_e is the exhaust velocity relative to the rocket.

Integral of this thrust vector over the mission duration is termed as total impulse and is given by,

$$I = \int_{t_0}^{t_f} T dt. \tag{1.2}$$

It is evident from Eq. 1.1, to achieve higher thrust we have to maximize the exhaust velocity with minimum propellant mass flow. Electric propulsion devices efficiently addresses this by coupling different energies into the propellant at an expense of electrical energy. More broader definition of electric propulsion devices according to Robert Jahn, the author of *Physics of Electric Propulsion* is:

The acceleration of gases for the propulsion by electric heating and/or by electric and magnetic body forces [6].

The electric propulsion devices are categorized according to the acceleration mechanism they employ.:

1. **Electrostatic Propulsion** Ionized propellant mass is accelerated by direct application of electric body forces. Hall effect thrusters, FEEPs and Gridded Ion Thrusters (GIT) utilizes electrostatic acceleration.
2. **Electrothermal Propulsion** Propellant mass is heated electrically and then expanded in a nozzle. Resistojets, Arcjet and Helicon thrusters are examples of this type of acceleration mechanism.

3. **Electromagnetic Propulsion** Ionized propellant is accelerated with interactions of external and internal magnetic fields. MPD thrusters, Pulsed Inductive thruster (PIT) are some examples that employs electromagnetic acceleration of the plasma obtained through ionization of the propellant mass.

Applied field magnetoplasmadynamic thrusters promise a good compromise between thrust density and specific impulse. Additionally, AF-MPD thrusters do not rely on rare Xenon and can be operated with various types of propellants such as Argon, Hydrogen and also with Lithium. Therefore, AF-MPD thrusters fit better into requirements of possible manned Mars mission compared to other conventional electric propulsion systems.

To investigate AF-MPDs, a $100\ kW$ steady state AF-MPD thruster SX3 has been built at the Institute of Space Systems for experimental investigations. The SX3 has been initially characterized in 2016 with thrust levels up to $3.5\ N$ and thrust efficiency in range of $20-50\ \%$. During the previous test campaigns, it was observed that the tare forces behave non linearly with the arc current and peculiarly at $500\ A$ there was a drop in the tare forces. This drop in the tare forces propagated to all subsequent calculation of thrust and performance parameters. Also the active cooling circuit of the thruster imparted oscillations in the thrust balance and affected the measurement technique by increasing noise in the data. Thus additional improvements of thrust balance and measurement technique are warranted for more reliable evaluation of thrust and thrust efficiency. An attempt to minimize or characterize these and other error sources in the measurement technique was made in the framework of this research.

Chapter 2

Introduction to Applied-Field Magnetoplasmadynamic Thruster

This chapter elaborates the magnetohydrodynamic theory and intoduces the physics behind SX3 AF-MPD that is being researched in IRS in University of Stuttgart. These concepts are necessary to understand the different effects of the thruster on the thrust balance and thrust measurement technique.

2.1. Magnetohydrodynamic Theory

Electric propulsion encompasses acceleration of ionized gas by means of electric and magnetic fields. The physics involves closely coupled compressible gas dynamics, ionized gas physics and electromagnetic field theory. Approaching such complex phenomenons, either for theoretical understanding or numerical analysis calls for simplification and some assumptions are made regarding the nature of the flow and processes. A widely used method to study this problem is the Magnethohydrodynamic theory, also called Magnetoplasmadynamic theory.

AF-MPD thrusters are categorized as the electromagnetic thrusters as the acceleration of the propellant is driven by the interaction of an electric and the magnetic field and generally MHD theory is used for simulations and theoretical analysis. The MHD theory calls for a quasineutral gas plasma exhibiting collective behavior. Quasineutrality is defined as having net neutral charge in the domain, this calls for same number of positively and negatively charged particles though the local concentration in regions might change. The uniform interaction of particles and the external fields through the discharge domain constitutes the collective behavior of the plasma.

2.2. Working principle of AF-MPD

AF-MPD thrusters are devices which employ coupling of both electric energy and magnetic field to accelerate the ionized gas. A high current is passed from cathode to anode which causes the ionization of the propellant, this plasma then interacts with an externally applied magnetic field and electric field. This results in a very high velocity exhaust, even when compared to other electric propulsion devices the AF-MPD has one of the highest exhaust velocities. As seen in the Fig. 2.1 following are the acceleration mechanisms [6][8].

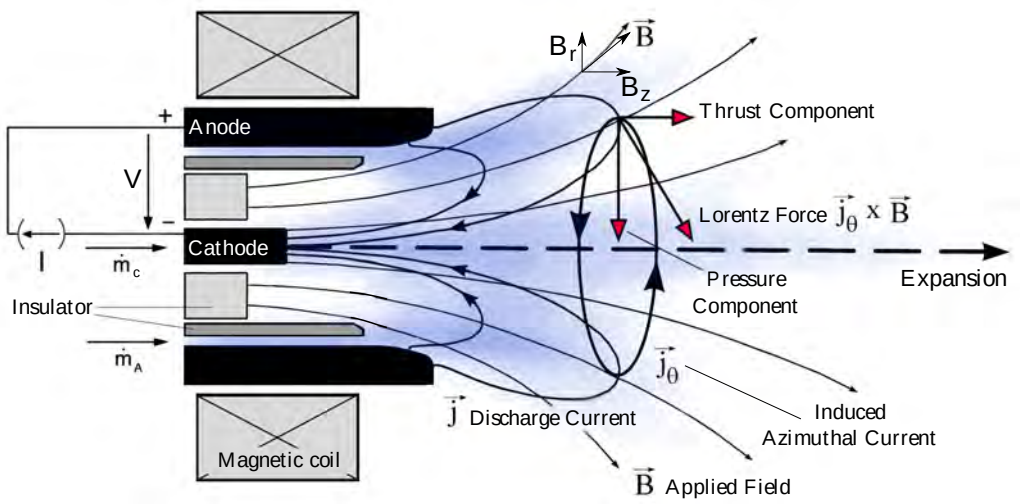

Figure 2.1: Acceleration mechanisms in AF-MPD [1]

1. **Electrothermal Acceleration** The electrothermal effect caused by Joule heating and dynamic gas exapansion in physical or magnetic nozzle. This acceleration mechanism contributes a small component in total thrust for low to moderate propellant flow.
2. **Self-Field Acceleration** The electric current flowing from anode to cathode induces an azimuthal magnetic field that interacts with the current itself resulting in a Lorentz force from the $\vec{j} \times \vec{B}$ product. The axial component of this product, $j_r B_\theta$ contributes directly to thrust, whereas the radial component $j_z B_\theta$ contributes indirectly by creating a pressure gradient on the cathode jet.
3. **Swirl Acceleration** When the applied magnetic field (with components $\vec{B}_z, \vec{B}_r$) interacts with the discharge current ($\vec{j}_z, \vec{j}_r$) results in a Lorentz force from the cross products of $\vec{j}_r \times \vec{B}_z$ and $\vec{j}_z \times \vec{B}_r$, which points in the azimuthal direction, causing swirl in the plasma. This induced rotational energy contributes into axial kinetic energy through the expansion of plasma in a physical or magnetic nozzle.
4. **Hall Effect Acceleration** For low mass flow rates and high Hall parameter and strong applied magnetic field, an azimuthal current j_θ is induced, referred as Hall current. Its interaction with the applied magnetic field ($\vec{B}_z, \vec{B}_r$) produces two electromagnetic force components similar to the self-field acceleration: a thrust component ($\vec{j_\theta} \times \vec{B}_r$) and a pressure component ($\vec{j_\theta} \times \vec{B}_z$).

2.3. Hall parameter and current distribution

Since the electrical conductivity σ determines the joule heating, it represents an important macroscopic quantity when describing the plasma flow of an AF-MPD thruster. It depends essentially on the temperature and density of the electrons [15]. Since the mobility of the electrons is considerably greater than that of the ions due to the lower mass in the plasma, the electrical conductivity can be increased with the electric field and is given by,

$$\sigma_0 = \frac{n_e \, e^2 \, \tau_e}{m_e}. \tag{2.1}$$

where m_e stands for the mass of an electron, n_e for the electron density and τ_e for the mean collision-free flight time of an electron between two collisions in which an electron and a heavy particle collide. Assuming a completely simple ionized plasma, the mean free flight time of the electrons can be determined and the electrical conductivity is [15]:

$$\sigma_0 = \frac{1,53 \cdot 10^{-2}\ {T_e}^{3/2}}{\ln\Lambda} \tag{2.2}$$

and

$$\Lambda = \frac{12\pi}{{n_e}^{1/2}} \left(\frac{\varepsilon_0\ k\ T_e}{e^2} \right)^{3/2}. \tag{2.3}$$

This indicates that the electrical conductivity for a simple fully ionized gas is approximately proportional to $T_e^{3/2}$. In the case of a strong applied magnetic field, the isotropy of the plasma is impeded, so that the electrical conductivity is reduced across the lines of force of the magnetic field. Thus the conductivity can no longer be treated as a scalar quantity and must now be treated as a tensor [15], [6]. Consequently, the conductivity in a IR^3 space can be expressed as

$$\tilde{\sigma} = \begin{bmatrix} \sigma_{xx} & \sigma_{xy} & \sigma_{xz} \\ \sigma_{yx} & \sigma_{yy} & \sigma_{yz} \\ \sigma_{zx} & \sigma_{zy} & \sigma_{zz} \end{bmatrix} \tag{2.4}$$

For simplification the electrical conductivity across the magnetic field lines can be expressed with the help of Ohm's law as a function of the Hall parameter [15], [4]:

$$\sigma_\perp = \frac{\sigma_0}{1 + (\omega_e \tau_e)^2} \cong \frac{\sigma_0}{(\omega_e \tau_e)^2}. \tag{2.5}$$

Since the Hall parameter increases with increasing magnetic flux density B, it leads to a reduction of the conductivity perpendicular to the magnetic field. As a consequence, the streamlines are carried further downstream with increasing B.

Based on the Ohm law, the Hall parameter $\omega_e \tau_e$ in the presence of strong magnetic fields is an important factor in assessing the Hall current. The formation of Hall currents is the main prerequisite for an additional plasma acceleration, caused by the resulting $\vec{j} \times \vec{B}$ forces.
For the Hall currents to form, the gas must be ionized as simply as possible and the individual particles must collide with each other as rarely as possible. The Hall parameter is the ratio of the gyration frequency ω_e of the electrons to their impact frequency ν_e and is defined by [15]:

$$\omega_e \tau_e = \frac{\omega_e}{\nu_e} = \frac{e\ B}{m_e} \frac{\sigma B}{e^2\ n_e} = \frac{\sigma B}{e\ n_e}. \tag{2.6}$$

The Hall current or azimuthal current can therefore develop better, the greater the gyration frequency and the lower the shock frequency.

Chapter 3

Experimental Setup and Existing Measurement Technique

This chapter focuses on introducing the SX3 experimental apparatus and elaborates on existing measurement technique that is used for the thrust measurement and calibration.

3.1. Experimental Setup

3.1.1. SX3 Experimental Setup (Tank 8)

SX3 is a steady state Applied-Field Magnetoplasmadynamic thruster designed and developed in IRS in 2011 through the framework of EU HiPER and ESA AF-MPDT program. The design is optimized for high applied magnetic flux density at relatively low discharge currents. SX3 operates on moderately high power ranging around $100kW$ for reasonably long periods due to the active water cooling employed. Fig. 3.1 shows the schematics of the SX3, the thruster and thrust balance is hosted in a vacuum tank of $2\ m$ diameter and $5\ m$ in length. The vacuum port is connected to the central vacuum facility which has 4 root pumps capable of drawing vacuum at the rate of $250000\ m^3/h$ at $10Pa$, resulting in minimum achievable pressure of $0.5\ Pa$ simulating high vacuum regime of space. The thruster is powered by a high current facility which can provide upto $6\ MW$ DC. Any variation of current and voltage can be used within the maximum power ceiling of $6\ MW$. As the coil and the thruster needs different current levels, two independent electrical circuits are connected to high current facility can be operated separately. The coil is designed to operate upto $2000\ A$ while thruster can operate upto $100\ kW$ of DC power. But due to restriction of current carrying copper strips, the facility always operates under these values. The coil circuit is designed to carry only $2.5\ kA$ while the coil is designed to carry $1.5\ kA$. Additionally different circuits are isolated using Plexiglas® enclosures and wrapped with Kapton® foil, closing all the gaps to avoid undesired discharge arcs. The current generation AF-MPD operates around $100\ kW$ due to the cooling limitation of the tank and thruster apparatus.

Tank and thruster apparatus are connected to central cooling facility which has a $25\ bar$ high pressure cooling circuit and a low pressure $4\ bar$ cooling circuit. This closed circuit has its own water storage and a heat exchanger which distributes the water to several other tanks as well through a piping network. Temperature probes are installed on inlet and outlet hose of all vital components to monitor the temperature and assess the cooling and terminate the operation if

the outlet temperature exceeds a certain point. At the tank level, the incoming water is split into a high pressure and a low pressure line, the high pressure line cools down the thruster and coil, while the low pressure line cools down the current decoupling unit and heat shield. The water feedthrough inlet is connected to hexagonal distributors which in turn connects to Polyamid 12(PA) pipes carrying cold water. The lower end of the pipes are connected to fixed structure and upper end is connected to moving thrust balance. So, these pipes are wound in a coil formation around the thrust balance to avoid unnecessary forces acting on thrust measurement due to the stiffness of pipes or their weight. As a safety feature, pressure gauges are installed in the tank to terminate the vacuum pressure in case of pressure loss due to the water leakage.

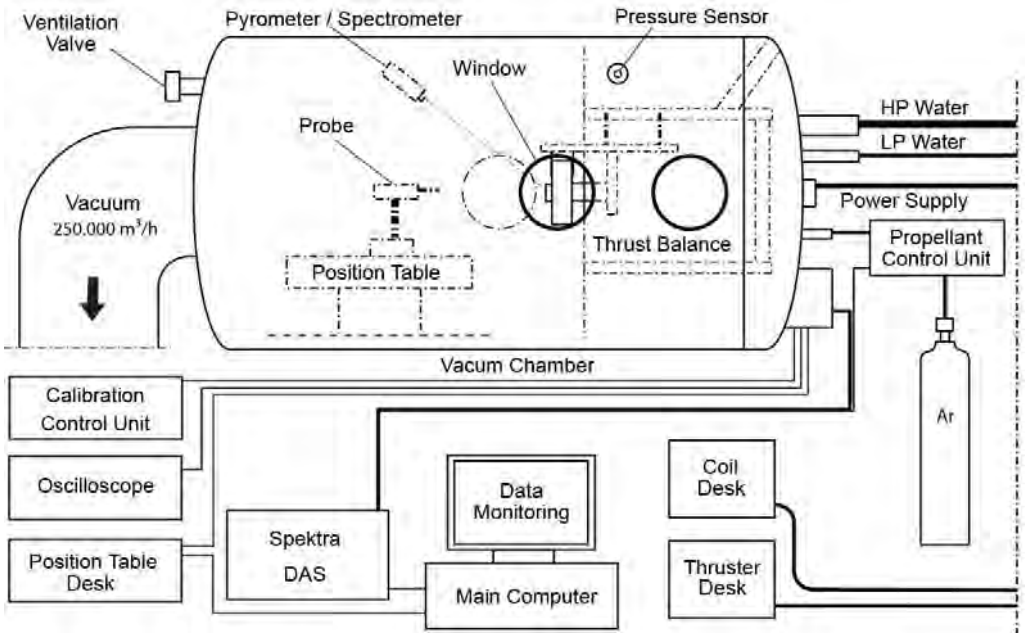

Figure 3.1: Subsystems of SX3 test stand [2]

Fig. 3.1 shows different systems required for the control, monitoring and measuring of the test apparatus, these systems assist the experiments. For data acquisition, msl Datascan 7320[1] is used with two 7021[1] modules for extension, this is connected to a computer via RS232 to Modbus TCP Ethernet adapter. Computer uses an in-house developed program for data monitoring and recording. The 7320 module is connected to self powered sensors and has 16 channels for sensing while the 7020 can provide electrical power to sensors as needed for temperature sensors and load cells in certain configurations. A precise pulsed excitation voltage of $1.8V$ is supplied to the sensors [16]. These modules can acquire data at 12- or 14-bit rate. This method cumulatively with DAQ and program acquires at a sampling frequency of $18\ Hz$, but this value is dependent upon the number of channels. For very high frequency measurement, oscilloscope is used. Beside physical channels the measurement program can also include virtual channel, allowing to calculate real time operational parameters of the test.

The position table is a two-axis translation stage is planned for future experiments for characterization of the plume and magnetic field. Various probes like pitot tubes, wedge probes, enthalpy probes, Hall probes, electrostatic probes can be mounted. The table is controlled with stepper motor controller connected to computer, software can be controlled manually with GUI. The controller can also interpret CNC machining code to aid the automation of measurement.

[1] Please refer Annex F for detailed information and technical specification.

The setup uses two Bronkhorst F-201CV[1] precision mass flow controllers to regulate the propellant feed rate for thruster's anode and cathode. The mass flow can be controlled from 0.5 to 100 mg/s of Argon with the accuracy of ± 0.5 % of reading plus ± 0.1 % of FS reading .

PT100 temperature sensors are used for temperature monitoring in both probes and foils form. These PT100 sensors indicate the temperatures of heated up water for respective parts. Currently there are 12 sensors installed, five of those are placed in water outflow pipes of the cathode,the main liner, the anode, the coil and the decoupling unit. The actual component temperature is higher than the water temperature but this indicative temperature represents the cooling that the part is getting and should be monitored through out the experiments as improper cooling of the thruster could severely damage the components. Foil type sensors are mounted on the exteriors of PA pipes, their temperature affects the internal nominal working pressure as well as stiffness of the pipes. Considering these factors, maximum surface temperature of pipes is determined to be around $60\,℃$. A foil type PT100 is used to measure the temperature of the force sensor mount, the measurement is affected due to thermal drift of the sensor. This temperature measurement is needed to characterize the force sensor measurement accuracy.

The setup uses a S-beam load cell KD40s-5 [1] force sensor from *ME-Messsteme* which can measure a nominal force of $5\ N$. The sensor is calibrated by the manufacturer and the calibration sheet is attached in the Annex F. The force sensor is optimized to measure axial loads along the principal axis[2]. The rated output of the sensor is $0.4914\ mV/V$ at full scale with an accuracy of 0.1 %. Detailed characterization of the measurement technique is discussed in later chapters.

An effort is made to ensure that the most of the components inside the vacuum tank is nonmagnetic, ensuring least interference with the strong applied magnetic field. Otherwise the interaction between the coil and components may introduce uncharacteristic error in the thrust measurement.

3.2. Thrust Balance

Traditional high thrust propulsion devices typically employ load cells for measurement. But with electric propulsion devices, the thrust produced is smaller compared to its weight and direct laod cell measurement is not possible or is inaccurate. So most of the electric propulsion devices are characterised using thrust stands that employs motion of a pendulum and then inferring that motion in terms of force. Accurate thrust measurement is one of the critical aspect of thruster's initial charecterization, and one of the most difficult measurements to make [23].

The thrust balance for SX3 AF-MPD is a hanging parallelogram pendulum thrust balance. A schematic representation of the thrust balance can be seen in Fig. 3.3, it also shows the characteristic forces of the thrust balance. The hanging structure is supported on the knife edges at three points, this reduces the frictional losses to a single line contact. All fixed support components are mounted on the vacuum chamber's lid and thruster is mounted on the moving part of the balance. As previously described in 3.1.1, the design is made considering that the current coupling and water circuit should be isolated from imposing any force on the balance.

The thruster and magnetic coil is mounted with its symmetric longitudinal axis inline with the force sensor's principal axis. The thrust balance oscillates and the angular movement is very small, eliminating need of complex analysis due to angular component, the movement at the

[2]Principal axis of force sensor refers to a reference axis through which load is to be applied, in this particular case it is concentric with the thread where the force is introduced.

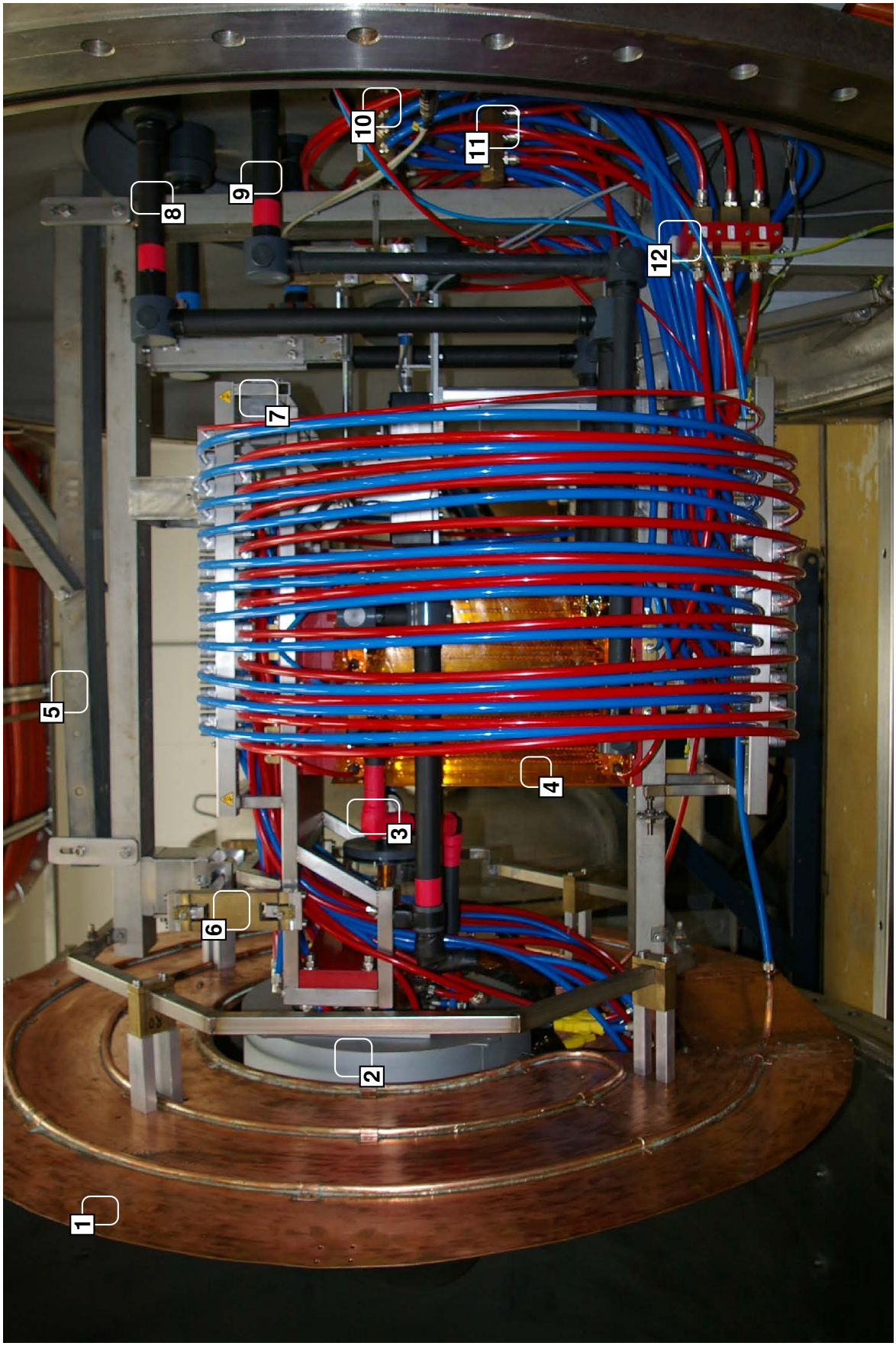

Figure 3.2: **Actual SX3 Test apparatus** – (1) Heat shield (2)Magnetic coil (3)Thruster (4)Decoupling unit (5)Fixed support Structure (6)Free moving arm of thrust balance (7)Counterweights (8)Coil current supply (9)Thruster circuit (10)High pressure water (11)Low pressure water (12)Temperature probes

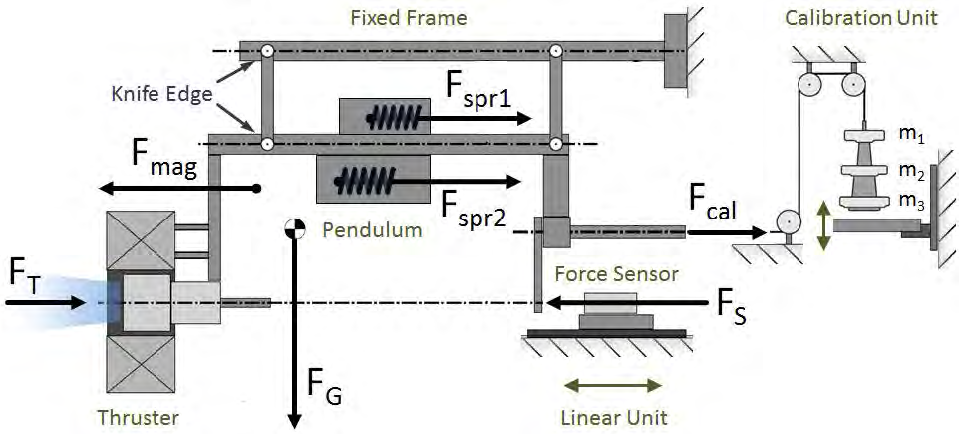

Figure 3.3: Schematic representation of thrust balance and characteristic forces [2]

Component	Mass [in g]	Equivalent Force [in mN]
Pyramid	50.87 ± 0.001	499.01 ± 0.00981
m_1	91.95 ± 0.001	894.79 ± 0.00981
m_2	98.61 ± 0.001	967.39 ± 0.00981
m_3	98.61 ± 0.001	967.39 ± 0.00981

Table 3.1: Calibration Masses

force sensor is considered linear. A small plate attached at the back transfers the oscillations of the thrust balance to the force sensor. A tip is designed for the force sensor that allows small contact point , enabling the force to be introduced at the inner threads of the force sensor[3]. For safety from erratic loads generated when the applied magnetic field is turned on, the force sensor is mounted on a translation stage driven by a geared motor, when the measurement procedure is initiated the force sensors moves in a predefined place to facilitate the measurement.

Other main component of the thrust balance is calibration unit. The calibration process produces the relationship between sensor output with the thrust produced, it also helps characterize other thrust balance parameters like accuracy, precision and repeatability by establishing a baseline for the measurement against the known masses [23]. Thrust balance is connected to a calibration unit with a fine Spectra® fiber[4] line through 2 pulleys. Calibration unit has a specially designed pyramid that can accommodate three different known masses made out of copper. The mass of each component is listed in Table 3.1, the errors are also listed and represents the measurement error caused by the weighing machine. Even though a high precision, self calibrating SHIMADZU weighing machine is used, the error needs to be characterized as this will be helpful later in determining propagation of uncertainty. A vertical, linear moving plate picks up or drops the masses on the cylinder. Depending on the direction it is moving, the plate loads or unloads the force sensor by adding or removing the mass.

The characteristic forces of the thrust balance can be seen in Fig. 3.4. Principal force exerted on the thrust balance is F_T and it represents the thrust produced by the AF-MPD thruster. The F_{mag} represents the force exerted on thrust balance due to the interaction on strong magnetic

[3]The specification sheet mentions the force introduction at the inner thread, Refer Annex F

[4]It is commonly used as a fishing line, The used fiber has $0.13mm$ diameter and is rated for $8kg$ load.

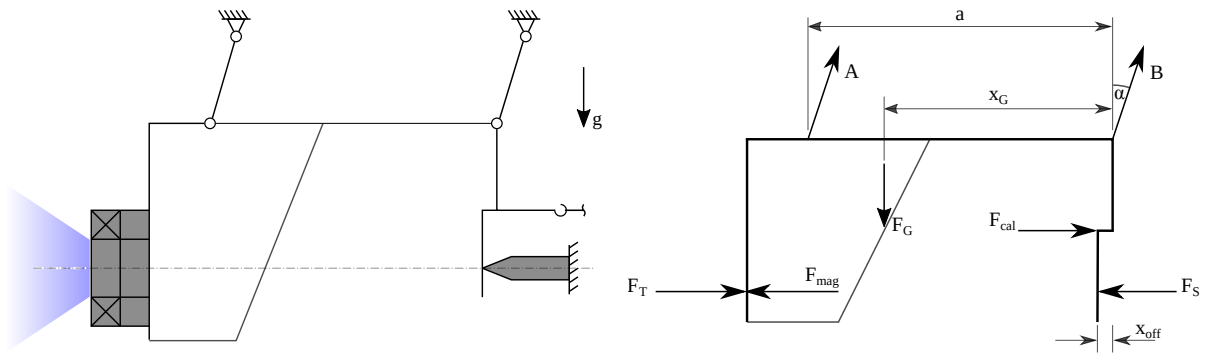

(a) Oversimplified thrust balance schematic (b) Simplified forces notation

Figure 3.4: Thrust Balance Force Notation

field with various components, this force is dynamic and strongly depends on the *B-field*[5] of the coil and its interaction with other components, for ease of calculation it is represented as a static unidirectional force. F_{cal} is the force created by the calibration unit on the thrust balance due to application or removal of m_1,m_2,m_3 on the pyramid. The F_{spr_1} is a representative force that is induced on the thrust balance due to coil like formation of the water cooling circuit. Though this force has a very low amplitude, it induces oscillations in the measurement and needs to be accounted from a theoretical standpoint. The F_G represents the total mass. The thrust produced is transferred to the force sensor and it is represented in figure as F_S. Detailed thrust balance statics and dynamics is discussed in coming sections.

3.3. Thrust Balance Statics

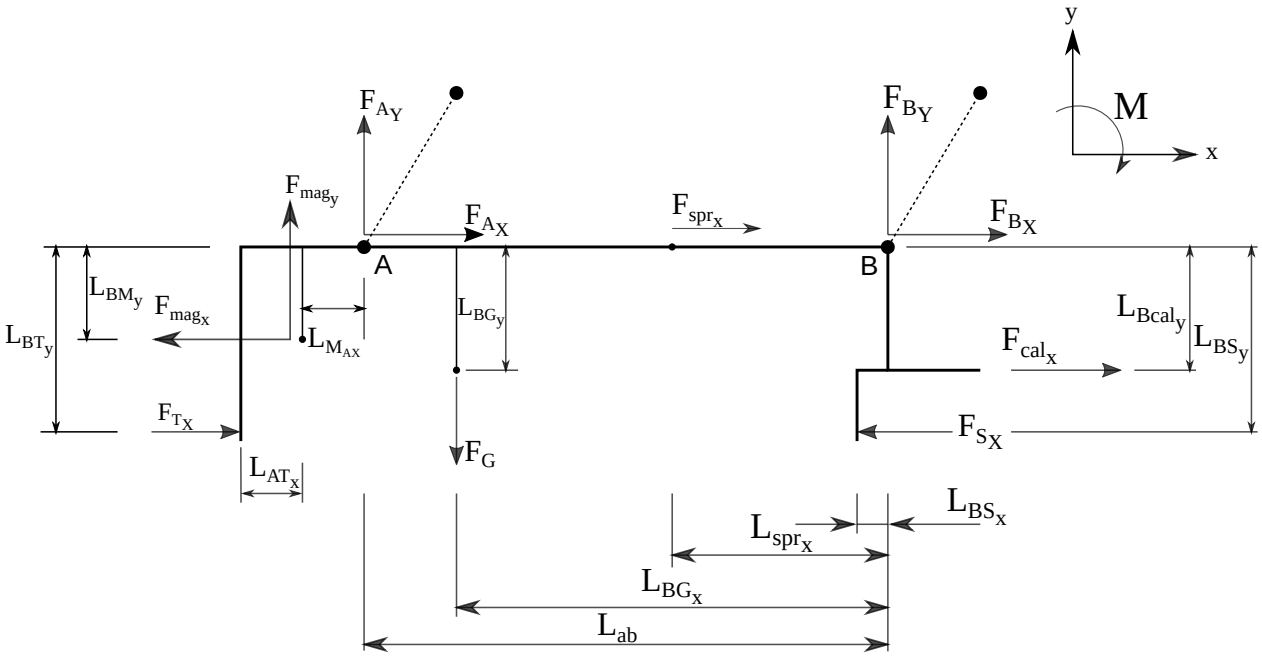

Figure 3.5: Thrust balance statics

The static state of the thrust balance and forces involved is represented in the Fig. 3.5, the

[5]B-field is the notation of strength of magnetic field and is measured in tesla.

coordinate system for the forces and moments is also shown. The forces with x subscript denotes $x-axis$ component of the force while the forces with y subscript denotes the $y-axis$ component of the force. Similar notation style is used for the lengths. The length measurements has been previously quantified and added in the Annex B for convenient reference. To solve the statics of the system, we resolve the forces and moments.

Equating forces in x direction,

$$\sum F_x = 0,$$

which gives,

$$F_{S_x} = F_{T_x} + F_{cal_x} + F_{A_x} + F_{B_x} + F_{spr1_x} - F_{mag_x}. \tag{3.1}$$

Similarly, equating forces in y direction,

$$\sum F_y = 0,$$

$$-F_G + F_{A_y} + F_{B_y} - F_{mag_y} = 0. \tag{3.2}$$

Taking moment at the hinge point A (knife edge),

$$\sum M_A = 0,$$

$$\begin{aligned}&(L_{ab} - L_{BG_x})F_G - L_{BT_y}F_{T_x} - L_{ab}F_{B_y} - L_{Bcal_y}F_{cal_x} + L_{BS_y}F_{s_x} + ... \\ &... + L_{BM_y}F_{mag_x} + L_{MA_x}F_{mag_y} - L_{spr1y}F_{spr1_x} = 0.\end{aligned} \tag{3.3}$$

Similarly the moment at the hinge point B (knife edge) gives,

$$\sum M_B = 0,$$

$$\begin{aligned}&-L_{BG_x}F_G - L_{BT_y}F_{T_x} + L_{ab}F_{A_y} - L_{Bcal_y}F_{cal_x} + L_{BS_y}F_{s_x} + ... \\ &... + L_{BM_y}F_{mag_x} + (L_{ab} + L_{MA_x})F_{mag_y} - L_{spr1y}F_{spr1_x} = 0.\end{aligned} \tag{3.4}$$

The moment at the sensor contact point is given by,

$$\sum M_S = 0,$$

$$\begin{aligned}&-(L_{BG_x} - L_{BS_x})F_G + (L_{ab} - L_{BS_x})F_{A_y} - L_{BS_x}F_{B_y} + (L_{BS_y} - L_{Bcal_y})F_{cal_x} + ... \\ &... + (L_{BS_y} - L_{BM_y})F_{mag_x} + (L_{ab} + L_{MA_x} - L_{BS_x})F_{mag_y} + (L_{BS_y} - L_{spr1y})F_{spr1_x} = 0.\end{aligned} \tag{3.5}$$

This complex system can be simplified with attributing physical parameters of the setup in the equations. As the coil is axisymmetric to the thruster, F_{mag_x} is considered a part of the thrust component F_{T_x}. The calibration force F_{cal_x} is given by the forces imparted by the calibration pyramid and the masses.

$$F_{cal_x} = F_{cal_x0} + F_{cal_x1} + F_{cal_x2} + F_{cal_x3}. \tag{3.6}$$

To characterize the thrust balance, non-ignition condition of the thruster shades a light into the forces acting on the sensor. Putting $F_{mag} = 0$ and $F_{T_x} = 0$ into Eq. 3.1, Eq. 3.2 and Eq. 3.5 we get,

$$F_{S_x} = F_{cal_x0} + F_{cal_x1} + F_{cal_x2} + F_{cal_x3} + F_{A_x} + F_{B_x} + F_{spr1_x}. \tag{3.7}$$

$$F_G = F_{A_y} + F_{B_y}. \tag{3.8}$$

$$\begin{aligned}(L_{ab} - L_{BG_x})F_G - L_{ab}F_{B_y} - L_{Bcal_y}F_{cal_x0} - L_{Bcal_y}F_{cal_x1} + ... \\ ... - L_{Bcal_y}F_{cal_x2} + F_{cal_x3} + L_{BS_y}F_{s_x} - L_{spr1y}F_{spr1_x} = 0.\end{aligned} \tag{3.9}$$

We can use the Eq. 3.7, Eq. 3.8 and Eq. 3.9 to characterize the thrust balance and this force then can be calibrated out of Eq. 3.1 for different ignition conditions to get the final F_{T_x} which represents the force produced by the thruster.

3.4. Thrust Balance Dynamics

3.4.1. Analytic Approach - Governing Equations

The pendulum type thrust balance used in Tank 8 is a variation of spring-mass-damper system [23]. Dynamics of the thrust balanced can be studied with equations of motion of the ideal pendulum. For a second order system the equation of motion is,

$$I\ddot{\theta} + c\dot{\theta} + k\theta = F_T L. \tag{3.10}$$

where, θ is the angular position relative to the equilibrium position of the thrust balance,

I is the moment of inertia of the system,

c is the dampening constant of the balance,

k is the spring constant of the restoring forces,

F_T is the force acting on the balance due to thrust,

L is the distance from a pivot point where the force is acting.

The I and c parameters of the Eq. 3.10 are constant as the physical dimensions of the thrust balance do not change. The gravity induces a torque on the balance to restore the equilibrium, which is given by,

$$\mathcal{T}_g = mgL_{cm}\sin\theta. \tag{3.11}$$

where, m is mass of the system, g is acceleration due to gravity, L_{cm} is distance from center of mass to the pivot point. This gravity component is a dynamic function of the force applied and is a part of the spring constant k from the Eq. 3.10. Similarly, the coil shaped geometry of the water pipes contributes to the damping effect.

3.4.2. Experimental Setup Assessment

To ensure free oscillation of the thrust balance, proper weight distribution is needed. The thruster approximately weighs $14\ kg$ and the coil weighs about $38\ kg$ and both are mounted in front of the thrust balance. All other components were carefully weighed and wherever it was impossible to weigh, a CAD tool was used to approximate the mass of the components. The non homogenoeous distribution of mass makes the center of mass very close to the thruster. To counteract this, Lead blocks are used as counterweights. Previous study has determined 3 blocks of $11\ kg$ each are needed for the free movement [17]. This resulted in shifting the

center of the mass between two pivot points, and higher than before due to placement of counterweight blocks. An effort was also made to keep the components symmetric along the plane of movement.

3.5. Existing Operating Procedure

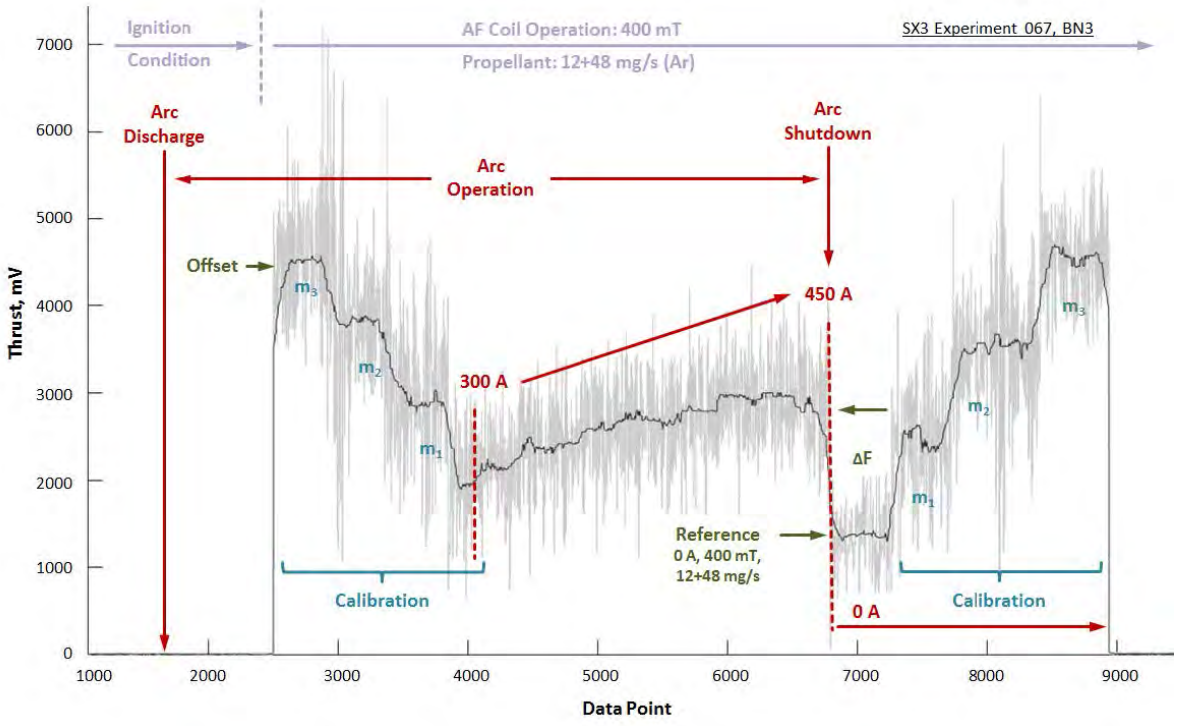

Figure 3.6: Typical raw data output for KD40s force sensor during experiment[6]

A typical operating procedure can be seen in the Fig. 3.6, it represents the time on the x-axis as datapoints and the output of the force sensor on y-axis. Different areas of thruster operations are marked on the figure as well. Notably, the thrust balance is locked until the applied field coil is fully operational. As the current supplied increases, the B-field increases, as the current levels are very high, a secondary magnetic field also induces around the cables and strips carrying the current, this effect is dynamic and the interaction between this field is uncharacteristic until a steady B-field is reached. During the ramp up, the interaction causes erratic motion in the thrust balance, to prevent the force sensor from damaging, thrust balance is kept in locked position until coil strength and ignition conditions are reached. Once the operational parameters are met, the thrust balance is decoupled for the measurement and downward[7] calibration is carried out. Then the arc current is increased in $25 - 50\ A$ increments until the onset of cooling capacity. After the shutdown of the arc, reference measurement is taken which is the reference for zero signal when the arc current is $0\ A$ and applied coil is till functional. After acquiring this reference signal, upward[8] calibration is carried out. Finally all the electrical systems are shut down. Still, this output voltage difference does not truly represent the thrust, a short circuit measurement is needed to ensure that the force sensor reading does not correspond to motion of thrust balance

[6] Image acquired from Adam Boxberger

[7] Downward calibration represents the masses being taken off the thrust balance, resulting in all the calibration masses placed on the lifting plate.

[8] Exactly opposite to downward procedure described above

due to electromagnetic forces. This test is carried out separately and characterized as Tare Forces, explained briefly in coming section.

3.6. Thrust Calculation

The raw data from DAQ is visualized with a program developed in-house in MATLAB® and it allows the interval selection for different conditions and stages of the experiment. After selection of intervals, the program calculates the mean values for those selected intervals which can be later used for the analysis and calculation of thrust. Detailed account of previous program and new program will be discussed later in next chapter.

The procedure of data post-processing includes calculating the linear drift of the force sensor, the influence of horizontal implementation, adjusting of calibration factor, calculation of force due to change in arc current, adjusting for tare forces and cold gas measurement. There is a drift for zero signal of force sensor caused by linearity and thermal drift of the sensor, this drift needs to be accounted for and adjusted in the final thrust measurement. This can be calculated by acquiring the zero signal at beginning and end of the test. Evaluation of the slope gives the drift factor and can be calculated as,

$$g_d = \frac{F_{s@(t_2)} - F_{s@(t_1)}}{t_2 - t_1}. \tag{3.12}$$

where, the subscript denotes the sensor output taken at the end and beginning of test. Linear interpolation of this drift factor then can be used to adjust the force sensor signal, as follows,

$$F_{s,cal@(t)} = F_{s@(t)} - g_d.t - (F_{s@t_1} - g_d.t_1). \tag{3.13}$$

where, the left hand side is the corrected force sensor signal and the term in bracket represents the zero signal at beginning of the test which is compensated for the drift. The vertical calibration of the force sensor and horizontal calibration factor showed a difference in previous experiments and this change in calibration factor is attributed to the friction between the pulleys and string, horizontal mounting of the sensor. Thus, it needs to be accounted for in the thrust assessment, this is adjusted as,

$$F_{s,cal(H)} = K_{VH}.F_{s,cal(V)}. \tag{3.14}$$

where the K_{VH} is the calibration factor determined experimentally by averaging the ratio of vertical and horizontal calibration for the same masses. Another major contributing factor to this calculation is Tare forces(discussed later, see 3.6.1) which is given by,

$$F_{T@B} = f_{T@B}.I_{arc}. \tag{3.15}$$

where, f_T is given by the slope of calibrated tare force at given strength of magnetic field B at the I_{arc} arc current. All these factors are adjusted in an equation to give final thrust calculation as,

$$F_{thr@I_{max}} = (F_{scal@I_{\max}} - F_{scal@I_{ign}}) - F_{T@B,I} + F_{cold(\dot{m}_c,\dot{m}_a)}. \tag{3.16}$$

where, the bracket represents the level drop in the force sensor output caused by the thrust produced between I_{max} and I_{ign} current (test condition maximum and ignition current) with applied coil strength of B Tesla. The F_T and F_{cold} represents the tare forces and cold gas thrust respectively and are quantified experimentally for different conditions. The need and quantification method for these forces is laid out in coming parts. This equation gives out the thrust produced for the given test condition. Many iterations of test conditions are carried out to see its effects on plasma mechanics of the thruster and the thrust is calculated as above.

3.6.1. Tare Forces

As explained earlier, electromagnetic interaction between the applied-field coil and current carrying chain imparts forces on the thrust balance. This behavior is dynamic and there is no certainty of direction or the amplitude. As the current grows, the applied field interacts with other induced B-fields and causes attraction or repulsion, but the strength varies as more current is applied, typically the current applied is in range of zero to thousand amperes. During 2016's test campaigns of this thruster, it was clearly established that the the tare forces can cancel out the force generated due to the thrust. So it is important to characterize these short circuit forces and are integral part of thrust measurement. For this, the length of the arc must be considered as the arc length in AF-MPD varies with applied field [9]. To accurately quantify the tare forces, a very close approximation of the arc length must be simulated to that of actual ignition and running conditions. Three different electrode interlinks with lengths of $25\ mm$, $75\ mm$ and $150\ mm$ have been previously designed and manufactured. Out of these, $25\ mm$ and $150\ mm$ were selected to simulate the arc lengths for $100\ mT$ and $400\ mT$ of applied field magnetic strength respectively. Previous tare force measurements show a negative trend, producing a force that cancels the thrust generated and ranges from $0.3\ N$ to $1\ N$ for the above mentioned magnetic fields. Previous test also showed a sharp drop in the tare forces for thruster currents above $500\ A$, making the regression fit very difficult. This could be attributed to variety of factors like magnetization of setup parts and mainly due to movement of current supply copper strips.

3.6.2. Cold Gas Measurement

Cold gas measurement represents the thrust generated by the gas dynamics in the thruster. To enhance the quality of fluid flow and mixing, a hollow cathode is used in the thruster, and propellant flow is controlled by two separate mass flow controllers which gives maximum achievable gas flow rate of $180\ mg/s$ for Argon. The force sensor is mounted in horizontal position and the signal. Data is acquired with an oscilloscope to ensure high frequency acquisition as the thrust produced by cold gas is relatively very low. Previous tests conducted determined the cold gas thrust in the range of $66\ mN$ for $200\ mg/sec$, this force was considered to be in the error range of the DAQ measuring chain, so it was omitted from the thrust measurement as seen in Eq. 3.16. New measurement technique error is very low and this thrust is significantly above the error and needs to be experimentally characterized again. Due to time constraints, it was not possible in the framework of this research but note should be taken to carry out these measurements, this will ensure more accurate thrust characterization.

Chapter 4

Improvement of Thrust Balance & Measurement Technique

Owing to previously identified error sources, a number of changes were made in the experimental setup for the thrust balance and the measurement technique. The need of these changes, the theoretical background and their implementation is discussed in this chapter

4.1. Improved Thrust Balance Design

As described earlier in 3.2, previous implementation of thrust balance used DC motors control with translation stages. New design was made to accommodate stepper motors for fine control over the position of the stages. Previously there were two translation stages, one each for Force sensor and one for calibration. A new microtranslation stage was designed for the distance sensor which is implemented for ProportionalIntegralDerivative Controller (PID) feedback and some other functions(discussed later), distance sensing and angle determination. Microtranslation stages, various mounts and adapters were designed for the new design, detailed account of their mechanical design is out of scope of this thesis. Analytical assessment of the microtranslation is needed to understand and determine the measurement procedure and the new implementation of their control (discussed in later sections).

Unit	Make & Model	Notation
Force sensor	Nanotec ST2818L1006-B	SM1
Distance sensor	Nanotec ST2818S1006-B	SM2
Calibration unit	Trinamic QSH4218-35-10-027	SM3

Table 4.1: Motors models for microtranlation stages

4.1.1. Microtranslation Stages

Previous linear stages was manually controlled by motors, there was no control over the position of the stage where the force sensor and lift-up stage of calibration unit was mounted on. The direction of movement was changed by reversing the polarity of the supply voltage. Limit switches

were used to switch on lights on the control box indicating the physical limits of the unit. The force sensor has a gear box with gear ratio of $1526:1$, which enabled fine resolution of movement. But positional accuracy and repeatability was erroneous because of the manual control. To overcome this, force sensor unit and calibration unit stages were adapted to accommodate stepper motors. A completely new microstranslation stage is designed for the distance sensor. The chosen motors can be seen in Table 4.1[1]. All the motors chosen has $1.8°$ step and depending on the motor driver used microstepping upto 256 can be realized, allowing very fine resolution for the movement. A detailed account of the movement resolution can be seen in Table 4.2.

Unit	Leadscrew pitch (in mm)	Gear ratio	Best possible micro-translation resolution[2] (in mm)	Selected micro-translation resolution (in mm)
Force sensor	2.5	1:1526	3.2×10^{-8}	8.2×10^{-6}
Distance sensor	0.25	1:1	4.9×10^{-6}	4.9×10^{-6}
Calibration unit	2	1:1	3.9×10^{-5}	2.5×10^{-3}

Table 4.2: Microtranslation stage resolution

4.1.2. Distance Sensor

Distance sensor implemented is being used for many things, including feedback for force sensor preload, distance sensing and as an analysis tool. It is also used for calculating the angular deviation of the thrust balance, which is useful for identification of thrust balance's dyanamic parameters. The distance sensor implemented is an eddy current(inductive) sensor. The used sensor is Micro-epsilon multiNCDT Series 300 with range of $1\ mm$ and output of $15\ V$ at FS.

4.1.2.1. Distance Sensor Calibration

To calibrate the distance sensor parts were designed and manufactured as seen in Fig. 4.1. A L-profile was used to mount the distance sensor on the PI M-105[3] microtranslation stage that is actuated by a micrometer screw. This microtranslation stage was mounted on another L shaped Aluminum profile, a circular Aluminum plate was mounted on this profile as sensing target. Another micrometer screw was also mounted for verification of the stage movement. Detailed mechanical drawings are added in the Annex E. The distance sensor is powered by the supplied power source and the output of the signal is taken on multiple voltage sensing devices for redundancy and accuracy. Philips PM2519 Ohm-defect multimeter and an oscilloscope was used for precise reading and to analyze the quality of the signal. As earlier discussed, the output of this sensor will also be used for PID feedback and control of the thrust balance stepper motors,

[1] Detailed technical specifications and their characteristic torque curves are added in Annex F

[2] This resolution doesn't represent one single step that can be taken from standstill. The motor needs to overcome the stalling torque of the motor, backlash of the gear and the starting torque of the leadscrew. These numbers best represent the finite movement of the stage when it is in motion. Theoretically, we can stop the stage at these increments, but the positional accuracy will be compromised by a minuscule amount due to mechanical limitations. When the pulses are stopped the holding current cant hold the microstepped position, it will go to the nearest $1.8°$ step equilibrium. Similar way if the the gearbox is implemented, there is a small backlash of the gear system, this is also a reason for positional inaccuracy at said resolution. This positional inaccuracy plays a very small role when compared with the thrust balance dynamics and other factors.

[3] See Annex F for more detailed specifications and drawings.

(a) CAD Design (b) Actual Setup

Figure 4.1: Distance Sensor Calibration Apparatus

voltage measurement on microcontroller was also carried out. Since the microcontroller can measure analog input signals upto $3.3\ V$, a voltage divider was used to step down the voltage from $15\ V$ full scale to $3.3\ V$ full scale. Therefore, the voltage divider was also calibrated owing to errors in manufacturing and thermal drift of the resistors, detailed description will be laid out in later parts. All these different measurements ensured accuracy of the calibration. The Fig. 4.2 shows the correlation between the micrometer movement and the output voltage of the distance sensor. Both the multimeter and microcontroller reading has almost identical linear regression and towards the end of range the readings are about $1.9\ \%$ of each other. Additionally, the signal of distance sensor was analyzed with the help of time resolved data recorded with oscilloscope.

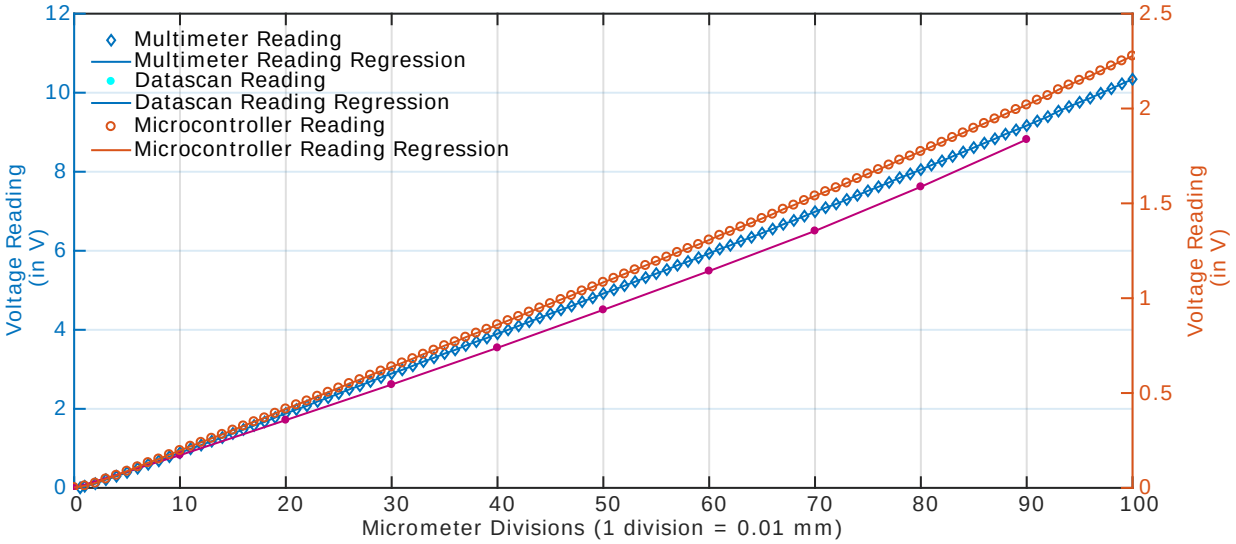

Figure 4.2: Distance Sensor Calibration
(Data:36.dat,manual reading,μC Script)

The average calibration ratios for full scale output is tabulated in Table 4.3. These factors correlate very closely to full scale reading[4] of the sensor, indicating direct linear relationship between output and distance. This data is used to analyze the oscillations of the thrust balance to characterize the thrust balance parameters like the spring constant, damping coefficient and the angle of the deviation as seen in Fig. 5.2.

[4]Here full scale refers to voltage reading after the voltage divider, the divider has a scaled full scale output of $10.4\ V$ from full scale $15\ V$.

Method	Calibration Factor (in mV/0.01mm)
DAQ	101.44
Multimeter	103.417
Microcontroller	103.5

Table 4.3: Distance Sensor Calibration Factors
(Data:36.dat,manual reading,μC Script)

4.1.3. Force Sensor Stylus Tips

Different force sensor stylus tips were designed and manufactured, their effectiveness is determined experimentally and is discussed in later chapter.

4.1.3.1. Static Stylus Tips

As seen in the Fig. 4.3, two different designs of static stylus tips were manufactured for the KD40s sensor. The pointy stylus tip facilitates the transfer of the force through very little contact avoiding the slip of the thrust balance onto the spike. On the other hand, the roundhead tip was already being used previously and has comparatively larger surface for contact. Detailed mechanical drawings of these styluse tips are attached in Annex E. Both stylus tips are machined with NC turning from Stainless Steel.

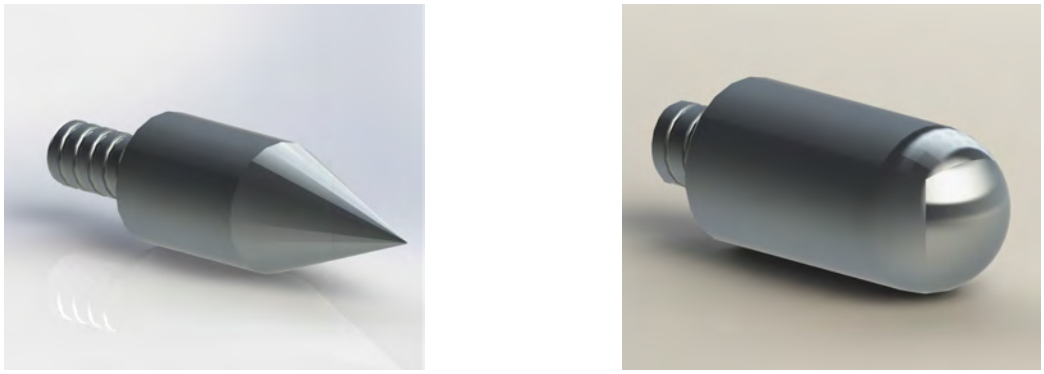

(a) Point stylus tip (b) Roundhead stylus tip

Figure 4.3: Static stylus tips for KD40s sensor

4.1.3.2. Rolling Stylus Tip

The thrust balance is designed to move linearly but as seen in Fig. 4.4, this movement causes a small angular displacement of the load plate which in turn induces a F_{s_y} component on the force sensor changing the axis of force application. To effectively transfer this y-component of the thrust onto the load cell, a rolling tip was made which can be seen in Fig. 4.5. The premise of this design is that it will transfer the y-component into the rolling motion of the bearing which will be transferred then to the axial x-component. Detailed mechanical drawings are attached in Annex E. Selection criterion for the bearing was that it should be non-magnetic, a stainless steel

[5]Zoomed in section of the thrust balance schematics, Refer original Fig.3.4

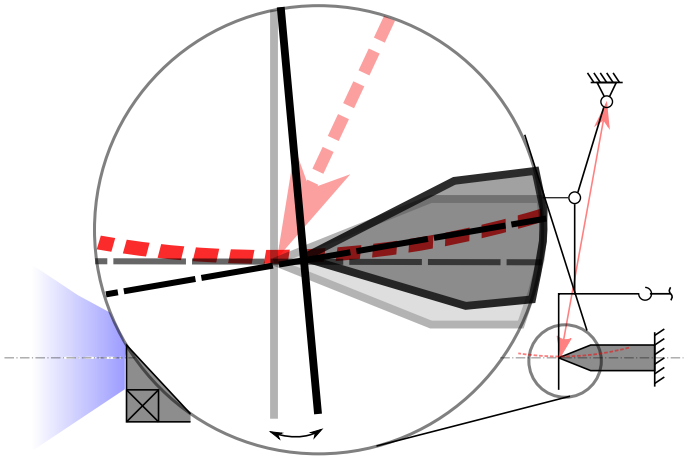

Figure 4.4: Influence of thrust balance movement on axis of force application [5]

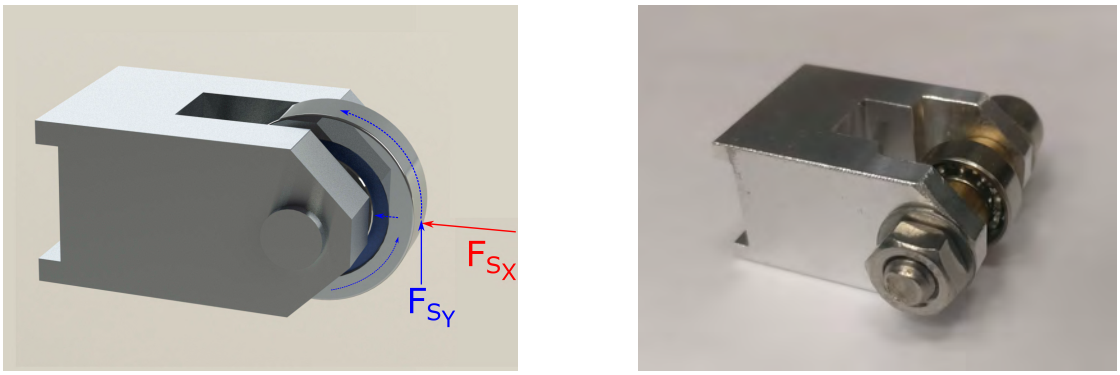

(a) Force schematic for bearing stylus tip

(b) Rolling stylus tip

Figure 4.5: Rolling Stylus for KD40s sensor

bearing *Groove Ball Bearing CE623*[6] is used. The bearing is placed symmetrically between the fork and effort is made while assembling to restrict all DOF except rolling with bronze bushings and thin stainless-steel washers, this ensures the force transference.

4.1.4. Force Sensor Horizontal Mount

Previously aluminum L-profile was used to mount the force sensor onto the linear movement unit. As the profile used was too thin a tiny displacement of 2×10^{-3} mm was observed through a simulation software, this would result in a force offset. To counteract this a bigger Aluminum block was designed and manufactured. The new design of the mount has a skirt on the bottom part to avoid swaying of the whole block on the microtranslation stage, force sensor is mounted with a M6 bolt(*DIN912*) and dowel pins, this ensures rigidity and that there will be no moment acting. Several spare mounts are made for future expansion considering a different sensor from same manufacturer, also spare holes are provisioned which can be used to make an adapter for different force sensors. A slit is made on top surface, close to where the force sensor is mounted, PT100 temperature probe is mounted here to monitor the temperature change in the force sensor mount. This temperature can be used as a reference for the force sensor temperature change, which then can be used to monitor and analyze the thermal drift of the sensor. Temperature

[6] Refer Annex F for detailed technical specification and drawings.

of the force sensor mount was found to be stable for long duration of experiments suggesting the new block design has improved the thermal mass for heat conduction and surface radiation, this will minimize the thermal drift of the sensor. Also the new mount doesn't deform itself on application of load as seen in Fig.4.6a, thus transferring all the forces to the sensor.

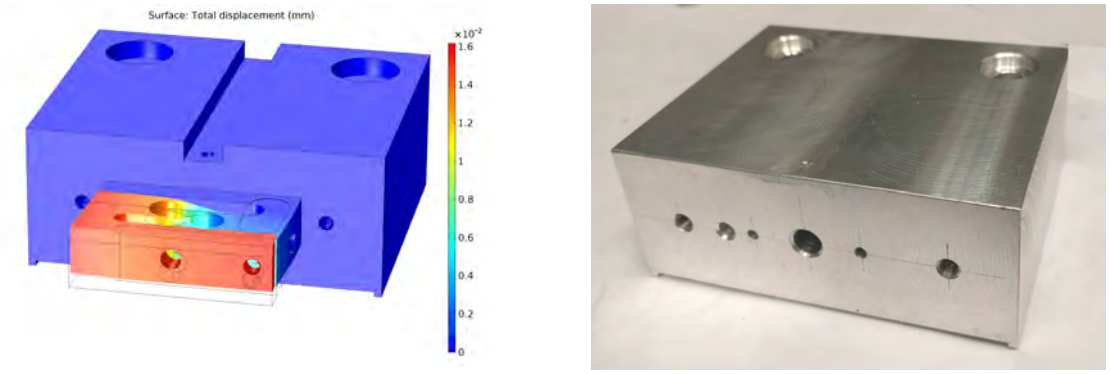

(a) Solid displacement of the mount (b) Force sensor mount

Figure 4.6: Force sensor mount

4.1.5. Force Sensor Vertical Calibration Mount

Vertical calibration of masses is necessary to ensure that force sensor sees true F_g force acting on the force sensor due to masses, neglecting all other influences like thrust balance statics, oscillations, friction in pulleys, pulley's side movement. For this a mount was made for the vertical calibration. As the force sensor is supposed to be preloaded when mounted in horizontal measurement position, provision was made in the mount to add extra mass as seen in Fig. 4.7b, thus imitating similar preload. Different nuts and washers were selected and weighed carefully to simulate the preload force. Similar preload is then used for the horizontal calibration, easiest way

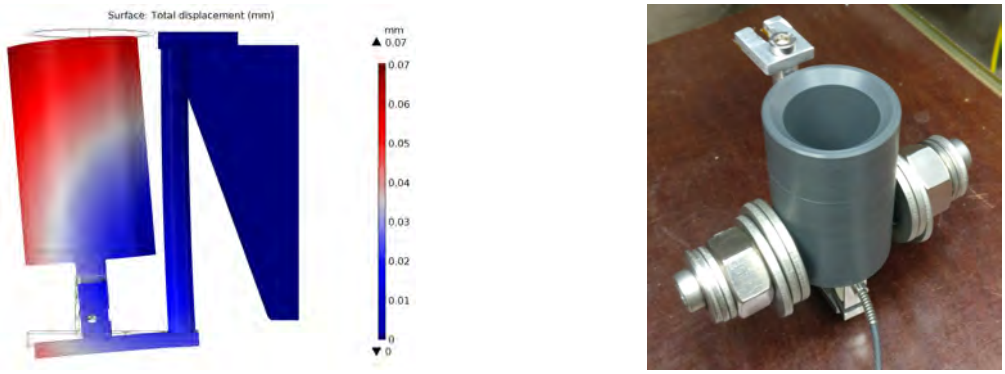

(a) Solid displacement of the mount (b) Mount with approx $5\ N$ vertical preload

Figure 4.7: Vertical calibration mount

to match the preload is to look for similar force sensor reading[7]. The vertical calibration is then compared to calibration done with horizontal position. This helps out determining the calibration ratio that is caused due to above mentioned reasons. As seen in Fig. 4.7a the displacement of

[7] Underlying assumption is that total force is transferred, which is not the practical case, but preload force only improves the DAQ measurement range and does not affect the thrust measurement

the mount is less than the nominal creep ($0.2\ mm$ for FS load), the force measurement error due to deformation of the mount is negligible.

4.2. Cooling Circuit Improvement

As earlier introduced, the test setup uses two water circuit for cooling, one is high pressure of $20\ bar$ and other is low pressure of $5\ bar$. Low pressure cooling circuit circulates water for the tank, current decoupling unit and heat shield. The high pressure water circuit cools the thruster and the coil. High pressure water circuit is a closed loop system connected to building's cooling circuit which employs a heat exchanger capable of cooling the water down to $17\,°C$. The plumbing system has very complex layout and this leads to a very high turbulent flow. Beside this, there are valves and flow control devices inline inducing shock waves in the flow. Also, as the hydraulic pump is positive displacement pump, it introduces a small pressure differential in the flow due to acceleration and deceleration of the pumped fluid[3]. As the flow reaches the tank, the pressure pulsations are apparent in the form of vibrations of the cooling circuit. This in turn causes oscillation of the thrust balance and it can be seen on the force sensor output and the deviation is significantly high. During previous tests it was roughly in the range of $1\ N$[8]. To stabilize the flow and the pressure, re-laminarization filters and a pulsation dampener is proposed.

4.2.1. Re-laminarization filter

Relaminarization filter works by forcing the fluid flow through parallel channels which reduces the relative velocity and parallelizes the direction of fluid particles thus smoothing the flow. Use of large number of small diameter flow channels makes the flow laminar. An abstract visualization of the process can be seen in the Fig. 4.8. Similar honeycomb structured filters are widely used in wind tunnels for laminarization of the air flow. All the water inlets at the tank feedthrough are chosen to be fitted with this filter.

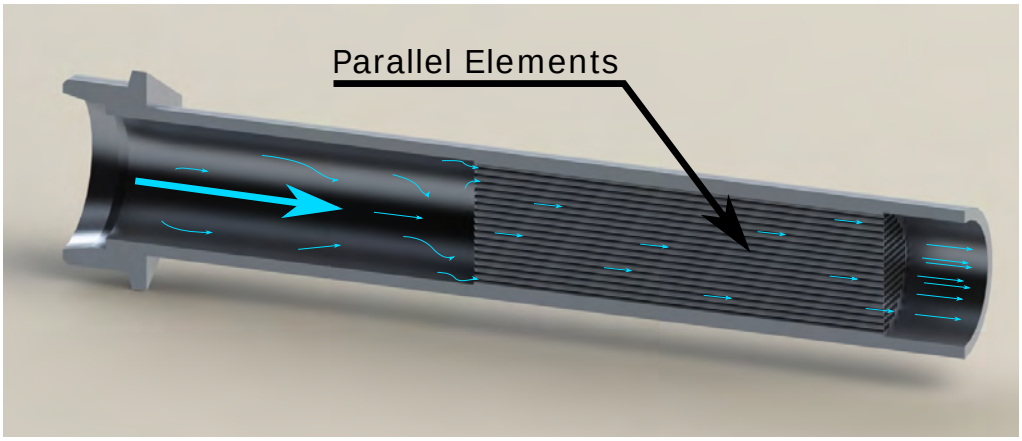

Figure 4.8: Sectional View of Re-laminarization filter

[8]Calculated with calibration factors from previous experiments, new method uses different connection thus changing the output and it is recharacterized and discussed in later chapter.

4.2.1.1. Working Principle

An important dimensionless parameter to characterize the flow regime is the Reynolds number(Re). Lower Re flows are laminar flows and as it gets higher it becomes turbulent, more turbulent flows carries of lot of turbulent kinetic energy which causes flow anomalies. These anomalies causes erratic motion in the flexible cooling circuit and imparts vibrations on the thrust balance, so laminar flow is favored in the cooling circuit. The Reynolds number of a flow is governed by the following equation,

$$R_e = \frac{\rho v d_H}{\mu} \tag{4.1}$$

where, ρ is the density of the liquid, v is velocity of the fluid, d_H is effective hydraulic diameter, μ is dynamic viscosity of the fluid.

It is apparent from the above equation that for same mass flow of the fluid the hydraulic diameter(d_H) plays a bigger part in determining whether the flow will be laminar or not. By forcing the flow through smaller diameter pipes, we reduce the Re for individual pipes and as the flow exits it looses all the turbulent kinetic energy and we get a laminar flow at the end[18]. A 2D simulation was carried out using loosely coupled fluid mechanics in COMSOL®. As seen in Fig. 4.9, there is clear difference in turbulent dynamic viscosity of the fluid and the fluid theoretically looses all the turbulence after the parallel elements.

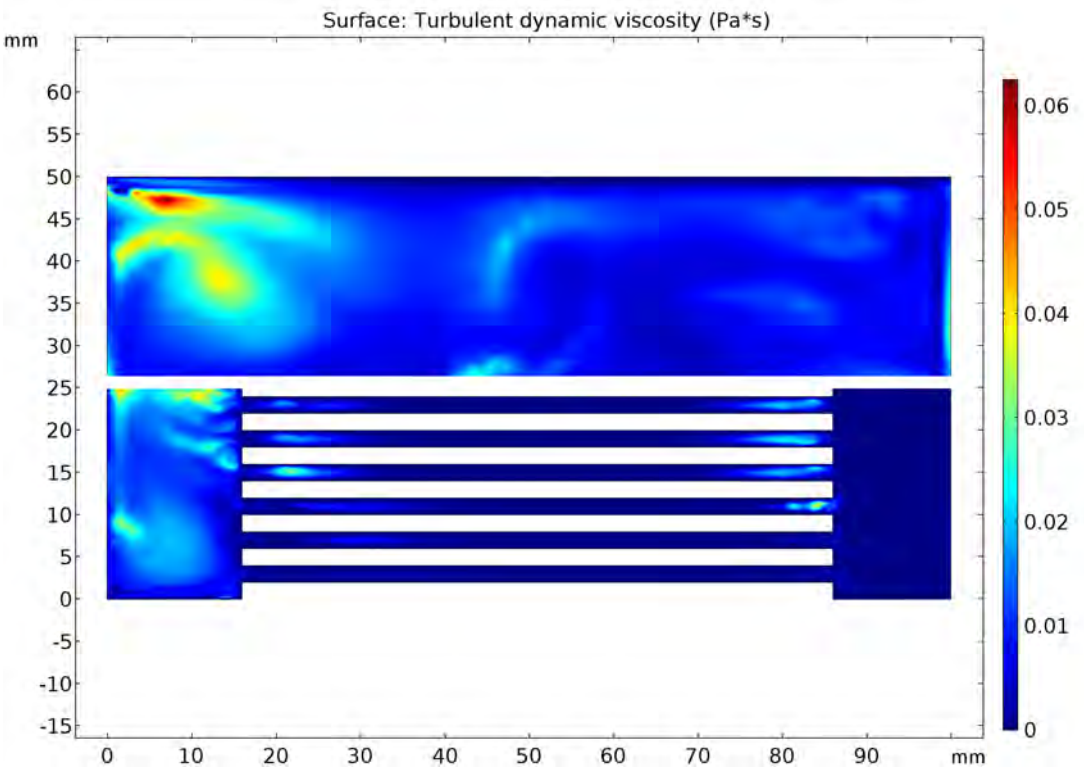

Figure 4.9: Turbulent dynamic viscosity in flow through (Top)Normal pipe flow (Bottom) Parallel elements

The length of the filter elements(pipes) is characteristic and contributes in laminarization. According to many previous researches[12][11], the length should be atleast 6 to 8 times the diameter of the element. This length also plays a role in pressure drop due to change in fluid

flow area. The pressure drop per element can be calculated using,

$$\Delta P = \frac{32\mu l v}{d^2} \tag{4.2}$$

4.2.1.2. Implementation

The filter design implemented is similar to a honeycomb, many small diameter pipes are fitted inside a larger pipe to provide multiple parallel channels. Interestingly, circle in circle packing is a mathematical complexity and a MATLAB® script was made to visualize the tessellation. To accommodate the filter in the water feedthrough, stainless-steel pipes of $\phi 40 \times 2\ mm$ were used. Smaller $\phi 6 \times 2\ mm$ stainless steel pipes were used for the filter elements. For these pipes, the script found the tessellation limit to be 29 with a packing fraction of 0.67. Depending on the availability of the materials, three different characteristic lengths of $140\ mm$,$100\ mm$ and $60\ mm$ were chosen for the filter elements and are for Coil,Thruster,Rest[9]

A coarse grid metal mesh is installed before the filter, this mesh takes out some of the turbulence from the flow before entering the filter, thus aiding the laminarization. The metal mesh used is $1 \times 1\ mm$ and it is cut roughly to similar diameter as that of the filter's outer diameter, every filter uses 4 of such mesh placed at an angle with each other and can be seen in Fig. 4.10 along with the filters. The smaller stainless steel pipes were cut to specific lengths and then a very tiny countersunk groove was made to assist the flow entry and exit. All the smaller pipes were placed carefully parallel to each other and was TIG welded together. The spot welding was paced out to avoid weld distortions ensuring the elements remain parallel.

Figure 4.10: Re-laminarization filter elements with metal mesh

Pressure drop calculated with formala from Eq. 4.2 also agrees with an online pipe parameters calculator[20] giving roughly similar values of $4.0484 \times 10^{-3}\ bar$ per element for $140\ mm$ elements, $2.8917 \times 10^{-3}\ bar$ per element for $100\ mm$ elements and $1.735 \times 10^{-3}\ bar$ per element for $60\ mm$ elements. It also indicates the flow will be laminar ($Re \approx 2300$). Total pressure drop across the filter and mesh is approximated around $0.1\ bar$ for each filter, this pressure drop is insignificant and will not affect the cooling performance.

[9] Rest here refers to tank,current decoupling and heat shield cooling circuit.

It is important to notice that there is a distributor suddenly after the filter and the flow is separated again in multiple flexible pipes for distribution. Even though this might impart some turbulence in the flow, the turbulence will be very nominal. Other flow anomalies will have already be diminished by then and the flow is less likely to effect the quality of the measurement.

4.2.2. Pulsation Dampener

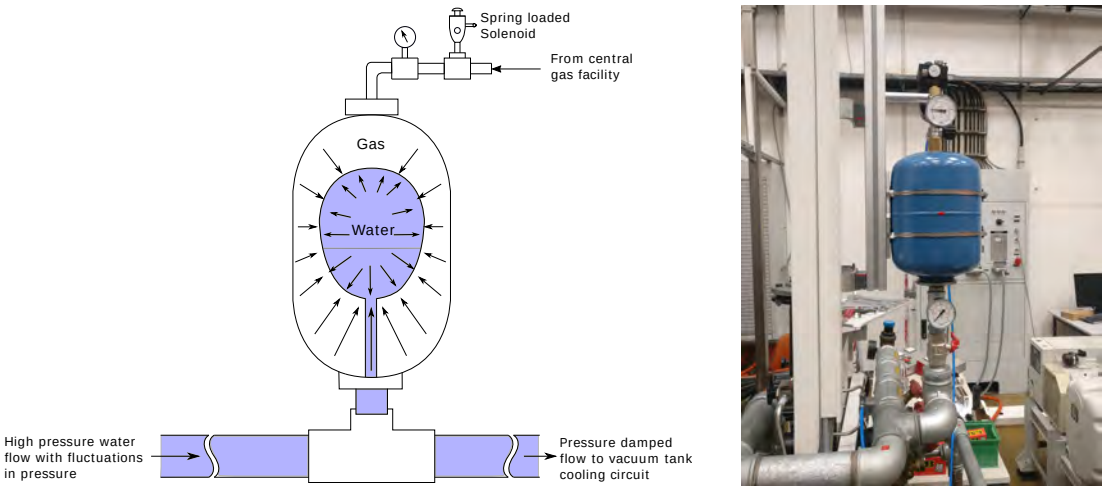

(a) Working of pulsation damper (b) Implementation of pulsation dampener

Figure 4.11: Pulsation dampener for water cooling circuit

As introduced, the pulsations are caused by dynamic pumping of the fluid, these pressure spikes have very low amplitude but their frequency can be very high, analogous to the speed of the pump. The solution to reduce these pulsation is to install a pressure pulsation dampener. As seen in Fig. 4.11, a hydropneumatic dampener is employed, it comprises of a pressure vessel containing a compressed gas which is separated from the pumped liquid by an elastomeric bladder. When pulse reaches the dampener, water enters the vessel and fluid compresses the gas and absorbs the shock. Conversely, when the pressure drops the gas expands and pushes fluid back adding in to the line pressure. This results in steady fluid flow. At the setup, this dampener is fed gas from the central gas facility through a spring loaded solenoid valve which vents out the gas pressure in case of sudden drop[10] of water pressure, thus saving the bladder from entering the water stream. Detailed account of installation of this device is out of the scope of this thesis. The effectiveness of the device is discussed in later chapter.

4.3. Electronics Control

As discussed before, electronics control of the thrust calibration is needed, a new electronic control box is designed to move the stepper motors attached to microtranslation stages as discussed in 4.1.1. Block schematic of the electronic control can be seen in Fig. 4.12, each of the stepper motors connected to force sensor,distance sensor, calibration's microstranslation stages have their own motor drivers which is connected to μC. The control signals are sent via STEP/DIR interface and drivers are connected via SPI interface for the configuration and feedback. The

[10] Sudden drop of the water pressure refers to closing of the water flow by means of valve or shutting down the pump.

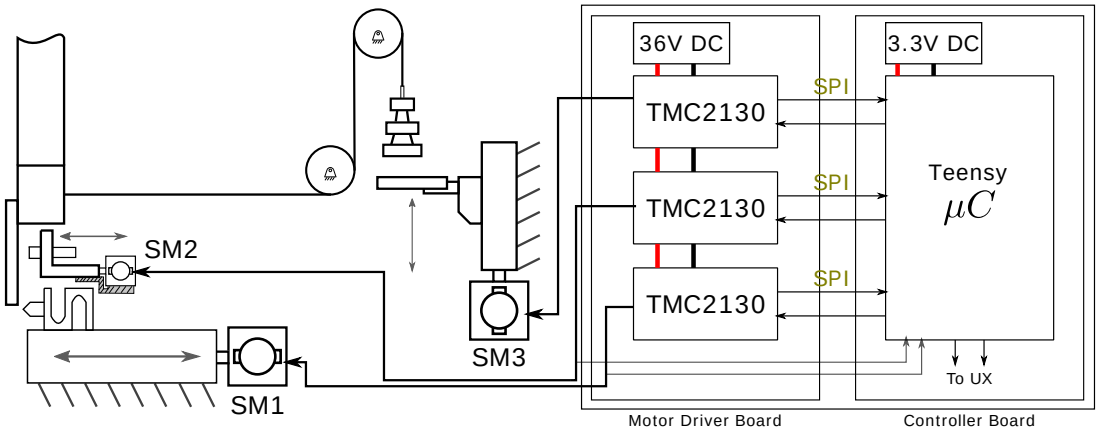

Figure 4.12: Electronics control

user interaction with the electronic control is with switches and an OLED display which displays the information, as seen in Fig. 4.13. The μC is programmed with Arduino IDE and Teensy Loader[21] via USB interface. First, all the connections were tested on breadboard and Printed Circuit Board (PCB) was designed. For modularity and efficient thermal management, separate PCBs were designed each for logic controller and motor controller. The control box was then assembled in house, power supply circuit was provided by the e-Lab of IRS, it includes a safety loop which can be connected to central safety loop of the test apparatus.

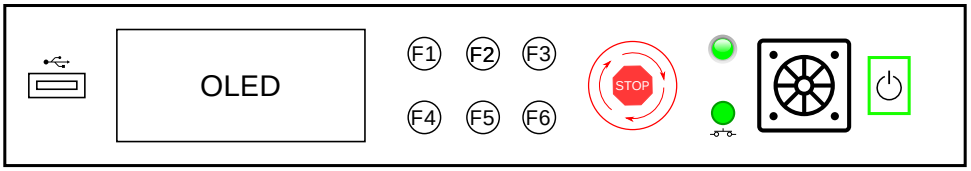

Figure 4.13: User interaction(UX) panel for electronics control(Main calibration program)

Switch	Function
F1	Lock Thrust Balance
F2	Decouple Thrust Balance
F3	Calibrate
F4	Load Force Sensor
F5	Deload Force Sensor
F6	Cancel Preload/Deload

Table 4.4: Current switch mapping for UX

4.3.1. μC Selection

Initial prototyping was done with Arduino UNO and it was quickly realized that a better platform was needed to accommodate all the functionality. Wide variety of platforms were assessed and then **Teensy 3.6** by PJRC was chosen, it has 32-bit ARM Cortex-M4 processor and has plenty of pins and ample communication protocols.

Figure 4.14: Electronic control box for thrust measurement and calibration

Processor	**Clock Speed**	**Flash Memory**	**RAM**
NXP MK66FX1M0	180 MHz	1 MB	256 KB
Operating Voltage	**GPIO**	**Analog Inputs**	**DAC**
3.3 V	58	25	2
PWM	**UART**	**SPI**	**I^2C**
22	6	3	4

Table 4.5: Salient features of Teensy 3.6 [22]

A synthetic benchmark tests was carried out with Arduino and Teensy 3.6 (hereafter referred as Teensy). A C language implementation of Whetstone benchmark by SyncChannel [25] was used, it showed Arduino processes 6.23 Million Instructions per Second (MIPS) in 16049 milliseconds while Teensy processes 438.60 MIPS in 228 milliseconds. Arduino Due was also a viable option but Teensy is faster. Beside the speed, it also hosts two Digital to Analog Converter (DAC), which will be very useful for faster acquisition of voltage signals of force sensor and distance sensor which is planned to be used for the PID feedback and other control logic. Other salient features of Teensy 3.6 are tabulated in Table 4.5. The number of peripherals planned to be attached to the μC and the speed requirement suggests Teensy is the right choice

4.3.2. Motor Controller Selection

From H-bridge circuits, there are many control options available for controlling the stepper motors but designing switching circuit is very crude and there are plenty powerful ICs available commercially that provides plethora of features. The stepper motors chosen for the translation stages are bipolar stepper motors so constant current microstepping drivers were elected. The motors selected for the translation stages have amperage rating of $1\ A$ per phase, accordingly appropriate current and voltage rating driver must be chosen.
A very popular choice is *Pololu Drv8825*[11], it was used to test and prototype the connections. But finally the *SilentStepStick* from *Watterott* featuring *TMC2130*[12] was implemented on the PCB. TMC2130 is a high performance driver IC for two phase stepper motors from Trinamic Motion Control. It has some unique features like CoolStep™ which ensures optimized current control for

[11] Full technical datasheet can be found online at http://www.ti.com/lit/ds/symlink/drv8825.pdf
[12] Full technical datasheet can be found online at https://www.trinamic.com/fileadmin/assets/Products/ICs_Documents/TMC2130_datasheet.pdf

energy savings and in turn the motor runs cooler, this feature will aid in reducing heat generation which is particularly important in vacuum. Another feature is StallGuard™ which does high precision sensorless motor load detection based on back EMF. stealthChop™ is another feature that is wideley appreciated in the 3D printing community, it guarantees silent motor operation and is based on voltage chopper principle, it also improves microstepping performance thus increasing reliable microtranslation.

Both the motor drivers has a potentiometer to set maximum current draw per phase. Minimum connection is made to the driver which includes powering it up and hooking it up with a microcontroller and enabling it. Then the voltage is measured along $V_{\texttt{ref}}$ potentiometer and `GND`, relation between the current and this voltage is available in individual datasheets of the product.

4.3.3. DC Power

Motor and the μC both needs DC power supply, in case of μC it is necessary to power it externally for standalone operation. Motor power supply requires a high voltage and high current power supply. A $200\ W$ single output switching power supply *LRS-200-36*[13] was chosen by IRS's electronic lab for powering the motor. The output of the power supply is fed to motor driver via terminal blocks. A large value electrolytic capacitor is added across the `VM` and `GND` of the controller which shields the driver from the LC surges that arises due to switching on the power.

Similarly a $20\ W$ power supply was provided and it supplies a $+12\ V$ DC voltage for the μC. This is again stepped down to $+5\ V$ DC via *TRACO POWER TSR 1-2450* DC to DC Converter and then routed to the breakout board. Teensy has an onboard PPU which further steps it down to $3.3\ V$ DC.

Interestingly, while decelerating the motor's momentum generates energy. Due to the efficiency, motor has no means of dissipating this energy. So the motor generates very large back EMF which might destroy the power source's capacitor, affecting the delivered power quality or this might break the power supply. But at any given time only one motor is operated, so other motors act as the sink for that generated excess energy as they are connected to the same power supply.

4.3.4. Electronic Schematics

Two PCBs were designed, prototyped and manufactured for the electronic control of the calibration procedure. One PCB hosts microcontroller, communications interfaces and pins for peripherals connection. This board also connects to the UX panel. Another PCB only has motor drivers with capacitors. They take control signal from other PCB and outputs the power to the motors. Two different PCBs were designed to manage the cooling efficiently.

Logic Controller

The logic controller PCB mainly hosts the heart of the logic controller, the Teensy 3.6 and the block schematic can be seen in Fig. 4.15[14]. Its mounted on the breakout board to facilitate easy replacement. On the UX side, OLED is connected to the hardware SPI. In case of switches, resistors are added inline for limiting the current and hardware debouncing. As previously mentioned there is a DC-DC converter on the PCB which powers the Teensy. The force sensor input is directly connected to `ADC0` and the distance sensor input is connected

[13] See Annex F for detailed specifications

[14] Detailed electronic schematics and pinouts are attached in Annex C.1.

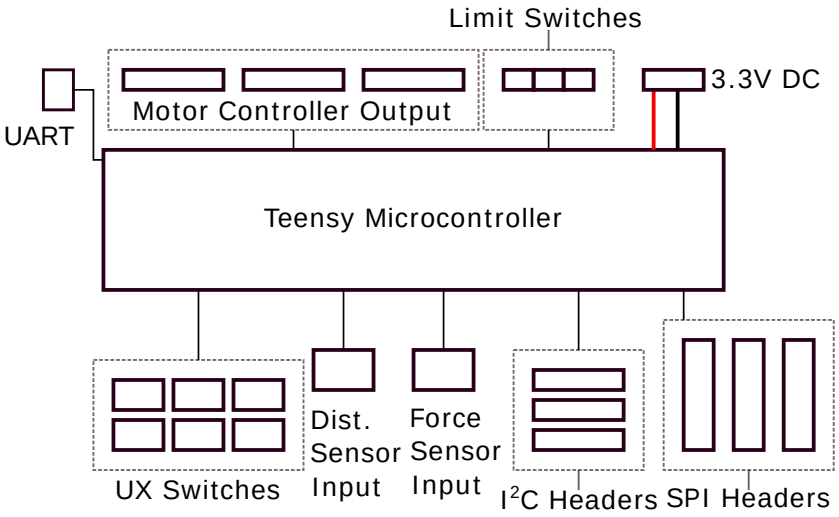

Figure 4.15: Logic controller PCB schematic

to ADC1 through the voltage divider. A spare voltage divide is also provisioned on the PCB for additional input. Limit switches are also wired in and connected to the board with molex connectors. Other communication interfaces are brought out and plenty spare headers are made for future expansion.

Motor Controller

Motor control PCB's block schematic can be seen in Fig. 4.16[15]. It hosts 3 stepper motor drivers and these are powered by $+36\ V$. The control signals for these drivers comes from other PCB via molex cables. Heat sinks are glued to the drivers with thermally conductive and electrically isolating adhesilve from *fischer elekronik*. All motors except force sensor are connected to drivers via full winding. Whereas the force sensor is connected via half winding, this is done to ensure high speed operation of the motor an in turn the translation.

The PCB is connected with the peripherals with molex cables and lock connectors. The analog input cables viz., distance sensor and force sensor only uses shielded coax cables, shield is connected to the ground and core carries the signal, so the whole analog circuit always measures above GND and so the code uses default reference voltage for comparison.

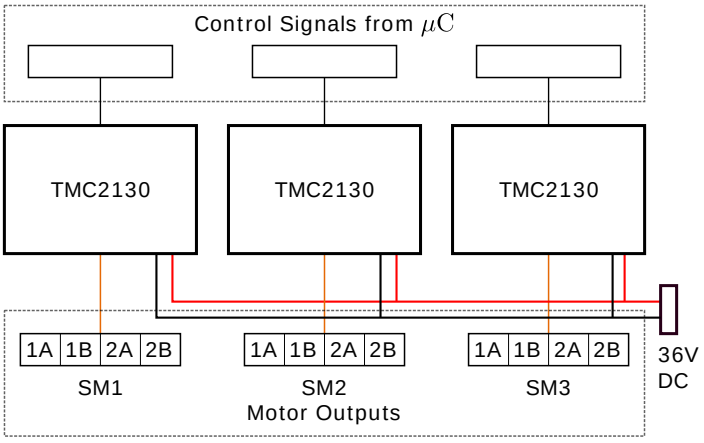

Figure 4.16: Motor controller PCB schematic

[15]Detailed electronic schematics and pinouts are attached in Annex C.2.

4.3.5. Voltage Divider and Calibration

As the Teensy pins are $3.3\ V$ tolerant, the external sensing voltage needs to be scaled down with voltage divider. Controller PCB currently connects the distance sensor through a voltage divider to scale full scale reading below $3.3\ V$ which will then be used for feedback for preloading the force sensor, so the voltage divider needs to be characterized and linearity of output must be guaranteed. To improve the accuracy of the voltage divider E96 resistors are used which has $\pm 1\ \%$ tolerance which results in $\pm 1.5\ \%$ error in U_a (see Fig. A.1). To further ensure fine control over output voltage, parallel resistors can be used across the dividing resistors as seen in Fig.4.17. R1 and R3 was identified using the 'Pointless Resistance[16]' tool for the required division, the values are $3.9\,\mathrm{k}\Omega$ and $1.1\,\mathrm{k}\Omega$ respectively. A 100 turns $50\,\Omega$ resistor is added across R3. Voltage divider was then powered with high precision power supply capable of delivering power in μV increments. The output was read on high precision ohm-defect multimeter, the R4 resistor was adjusted by turning until the output voltage meets the required divider ratio, the R4 value was found to be $47.6\,\Omega$.

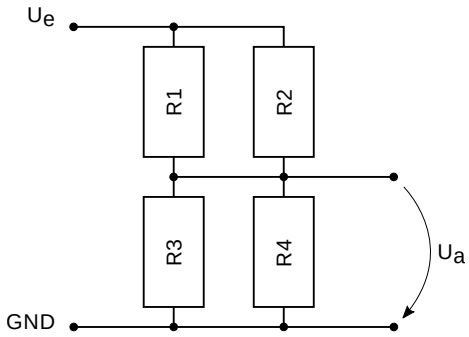

Figure 4.17: Voltage divider

Another modular voltage divider circuit is provisioned on the PCB for future use. Calibration resistor can easily placed in parallel or series with either of the dividing resistors and if needed, jumpers are also provisioned to complete the circuit.

4.3.6. Communication Interfaces

As seen in Fig. 4.15, the PCB designed hosts variety of communication interfaces for current and future use. Several spare headers for different communication interfaces are drawn out to fully utilize all the pins of the μC.

- **UART**
  Even though its not a communication protocol like others mentioned later, its a physical circuit in the microcontroller whose primary purpose is to transmit and receive serial data [13]. This necessitates both the peripherals to have similar baud rate. Behind the scenes, the onboard microcontroller is flashed with this method.
- **I^{2}C/Wire**
  This is a multimaster, multislave synchronous computer bus wideley used for connecting low speed peripherals like temperature sensors. All masters and slaves share data lines and each device has a address by which the data flow is controlled.

[16] Named after Star Trek reference 'Resistance is futile', found on https://www.muellerzumhagen.de/tools/widerstand-ist-zwecklos-pointless-resistance/

- **Serial Peripheral Interface(SPI)**
  This is most commonly used interface to connect with peripherals like sensors, ADCs, DACs, registers, SRAMs,etc. SPI is a synchronous interface where μC and the peripheral share clock and data lines and synchronization occurs at rising or falling clock edge. This facilitates connection to multiple peripherals as only one pin(chip select/slave select) needs to be assigned for each peripheral. On the logic board, motor controllers are configured with the SPI interface. In this case, the protocol is emulated by ***Bit Banging*** [19], in the implemented library it is referred as software SPI. This was done to ensure compatibility with other motor driver controllers. OLED also uses the same protocol but through hardware SPI.

4.3.7. Sequential vs Parallel Code Execution

The μC can be programmed to execute the code sequentially or in parallel turning it into a state machine. Parallel execution of code imitates the modern operating system and uses timers and schedulers to keep track of the code execution. Current requirement of operating procedures does not necessitate the code blocks to be running in parallel, so sequential code execution is chosen. This not only ensures the reliability of the operation but also ensures the safety of the sensitive components and the setup.

4.3.8. Code Breakdown

The code is extensively commented making it easier to understand the logic. The code breakdown presented here helps identifying the file structure and their heuristic role in the programming and the calibration procedure.

4.3.8.1. `sx3_cal.ino`

This is the main file that holds the main logic of the operation and includes all other helpers files and other subroutines. The extension `.ino` is for the Arduino IDE files. The IDE compiles this file with `avrdude` and makes an executable hex file for the μC which is then flashed to the Teensy using Teensy Loader tool. This file has two parts, one is `void setup()` and `void loop()`. Prior part runs only once when the μC boots, so various initialization and flags are programmed here. The loop part of the program runs continuously unless hardware interrupts are detected. The loop in the program constantly checks rise and fall of the switch signals on the UX and translation stage's limit switches. Different functions are called for execution for different switch press. Most of the motor functions are coded in a way that if a change in the limit switch is detected the function exits and goes back to the main loop. Additional sanity checks are added to ensure safety of the components and for a uniform operating procedure.

4.3.8.2. `headers.h`

This file contains all the headers and includes other helper files, this is done to reduce the cutter in the main file. The headers will not change unless any hardware modifications are made or other libraries are implemented for the control logic.

4.3.8.3. `pcb_pins.h`

This file contains all the pin definitions that are required to send command signals over to the peripherals. The pin layout is fixed and the pinout for the PCB can be seen in Annex C.1 and C.2. Unless any physical re-routing of the cables is done in the electronic control box, the pin definitions will not change. These pin definitions are then used in other parts of program making code blocks modular.

4.3.8.4. `settings.h`

This is the helper files that helps set different configuration options. This variable definitions are then used in other files, it facilitates easy access to configurable options without scouring through the code. Many important control parameters of the control logic are abstracted out. It is important to know, these are not implemented everywhere, sometimes these are overridden and other values are hardcoded, this is dont to ensure safety or optimized operation of the calibration and measurement procedure.

4.3.8.5. `init.h`

This file initializes the class instances of the libraries that are included for the peripherals. It also sets different flags that are coded for variety of sanity checks that aids the control logic.

4.3.8.6. `functions.h`

Common control logics are abstracted out as functions and are stored in this file. This avoids repetitive code and improves readability of the code. Some functions are also overridden for the faster performance.

4.3.8.7. Important Notes

- Even though the PCB is designed to replace the motor drivers, there would be significant changes in the programming logic and the code needs to be adapted for new motor drivers.
- Precaution must be taken not to plug the distance sensor cable into force sensor port on the control box, the port is routed to the μC pin which is only $3.3\ V$ tolerant. The coax cable and the port are both clearly labeled, **S1** for **Distance Sesnor** and **FS** for **Force Sensor**.
- Mostly the variables from settings.h are used but in some cases they are modified and hardcoded in some functions. Do not change these hardcoded variables as they might alter the functioning or compromise the safety, e.g. through extensive trial and error optimum signal frequency and delay intervals were found for decoupling the thrust balance, if these are changed it will cause the thrust balance to bounce hard on the force sensor.

4.3.9. Effects of electronic control on thrust measurement

Operating the motors on the microtranslation stage affects the force sensor measurement. Probable cause of this is GND interference, cable shield interaction or EM interaction at feedthrough. As the thruster's tests require to switch to High power ground from normal ground, all the electrical circuits and electronic components share the same electrical ground, so using separate GND circuit for individual component is improbable. But there are no adverse effects

seen of this common grounding. Typical current levels to power the motor are in range of $1\,A$ and this induces tiny magnetic field around the cables, so shielded cables are used to reduce induced field influencing other signals. Cables are also carefully placed in parallel side-by-side reducing any external interference. Even with all these measures, experimentally it is observed that motor movement adds small noise in the force sensor measurement. The programming is optimized to counteract these effects by logically switching off the motor drivers, this also ensures that motor is not powered up thus improving thermal performance in vacuum. Drawback of this powering down is that no holding torque is present. But the gear box of force sensor translation unit and starting torque of the calibration unit and distance sensor unit ensures positional reliability of the individual units.

4.3.10. Force Sensor Preload

Initially force sensor preload was designed to be carried out via PID logic. The microtranslation stage will slow down as preload on the force sensor approaches the set value in the `settings.h` file and tune the movement to reach the preload as close as possible, in turn giving very accurate preload. But currently the force sensor microtranslation stage employs a gear with gear ratio $1:1526$ this makes the resolution very acute but this results in very slow movement. The motor rotation can be sped up by sending STEP signals really frequently but it is also limited by the current ramp up time for the given power supply at set voltage. If the control signals are sent too fast, the driver could not ramp up the current fast enough to build any torque with the coil which is required for rotation. Determining the pulse frequency is an iterative process,and if any control logic is changed, the frequency changes drastically. The fastest signal frequency that can be sent to the drivers is a signal of $400\ \mu sec$ each (optimized for speed), which roughly translates to $185\ rpm$ motor speed and force sensor translation of $0.4\ mm/min$. Very fine movement of the force sensor results in requiring very long duration to preload. The force sensor can not be coupled before turning on the applied-field coil to ensure safety of the sensor. Preloading the force sensor after the coil is running will result in loosing cooling power and onset will occur sooner. Things get further complicated with high amplitude oscillations due to cooling circuit, making the PID logic very complicated. So the current implementation of force sensor preload does not employ the PID logic. Now, the switches on the UX panel are configured to preload the force sensor based on the distance sensor reading[17]. The PID control can be revisited after the gear is replaced with low gear ratio gearbox.

4.4. Measurement Technique Improvement

4.4.1. Connection Selection

With the DAQ module, there are three possibilities ways of connecting the force sensor to the DAQ. The various methods gives out different errors, so it is necessary to characterize respective errors to choose a method of least error. The three possible connection for the force sensor which are tested are as follows.

[17] There is a known issue with this, as the thrust balance decouples it bumps against the distance sensor briefly, the sensor is not likely to break with this force but repetitive bouncing causes the fastening to loose up. This causes the distance sensor to move causing it to output different position requiring constant updating the set value in the program. A rubber shock absorber installed around the distance sensor will fix this problem, care should be taken that this absorber will not restrict the movement of the force sensor or the thrust balance.

[18] Please see Annex C.3 for detailed electronic schematic.

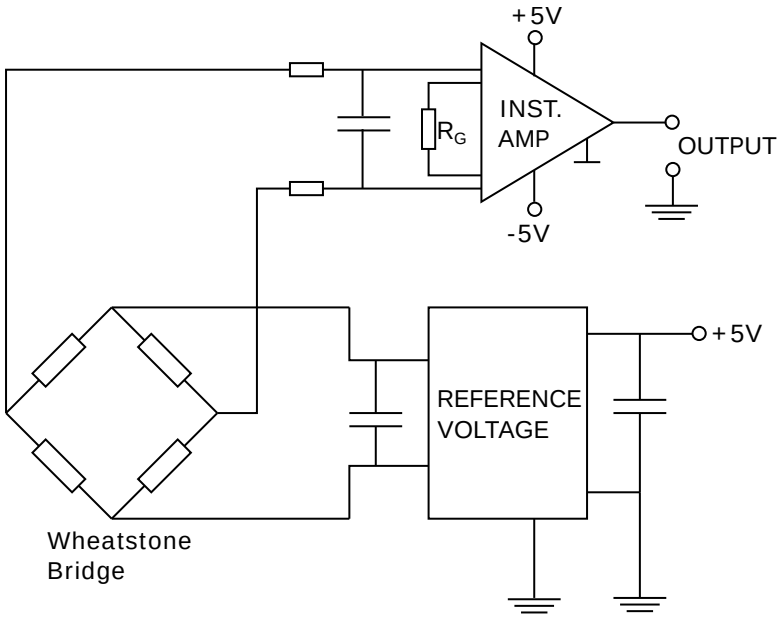

Figure 4.18: Signal amplifier schematic[18]

- **Amplified Mode**

  Amplified mode is same as that of fullbridge mode except a external power source is used and then signal is amplified using electronics. The Wheatstone bridge is excited with a continuous reference voltage, capacitor is added across the output for power quality. The unbalanced voltage of the bridge is then fed to an instrumentation amplifier. The amplification factor is adjustable with a resistor and is a function of the individual amplifier. Discussion about gain determination will be carried out later. Schematic of this circuit can be seen in Fig. 4.18. Both the reference voltage and instrumentation amplifier used are precision grade. But due to the use of resistors and capacitors the error of the circuit is approximated to $0.2\ \%$, to accommodate linearity and thermal drift of the ICs and resistors, for the calculation of analytical error.

- **Unamplified Mode**

  Unamplified mode connects the '+','-' of DAQ with force sensor. The force sensor is powered by the above mentioned amplifiers reference voltage. But, biased voltage of the bridge is not amplified resulting in the output signal to be in the range of few millivolts. Due to the low range of measuring voltage the error is relatively higher.

- **Fullbridge Mode**

  The wheatstone bridge of the force sensor is energized with the DAQ power supply and connected at '+','-' of the DAQ, The sensing terminals 'S+' and 'S-' are shorted with '+','-' which assures precise excitation of the bridge circuit. The unbalanced strain gauge voltage is measured at 'H' and 'L' of the DAQ. During the test, the excitation voltage was found to pulsed, a $1.8\ V$ power is applied just for $8\ ms$. This is done to reduce the heating effects of the sensor, thus resulting in accurate reading. The output signal is then used internally by DAQ to calculate the microstrain ($\mu\varepsilon$). Essentially, this connection is similar to amplified mode but the energization is handled by DAQ and the energization is pulsed.

An experiment was designed to characterize the error, force sensor was attached with a stage

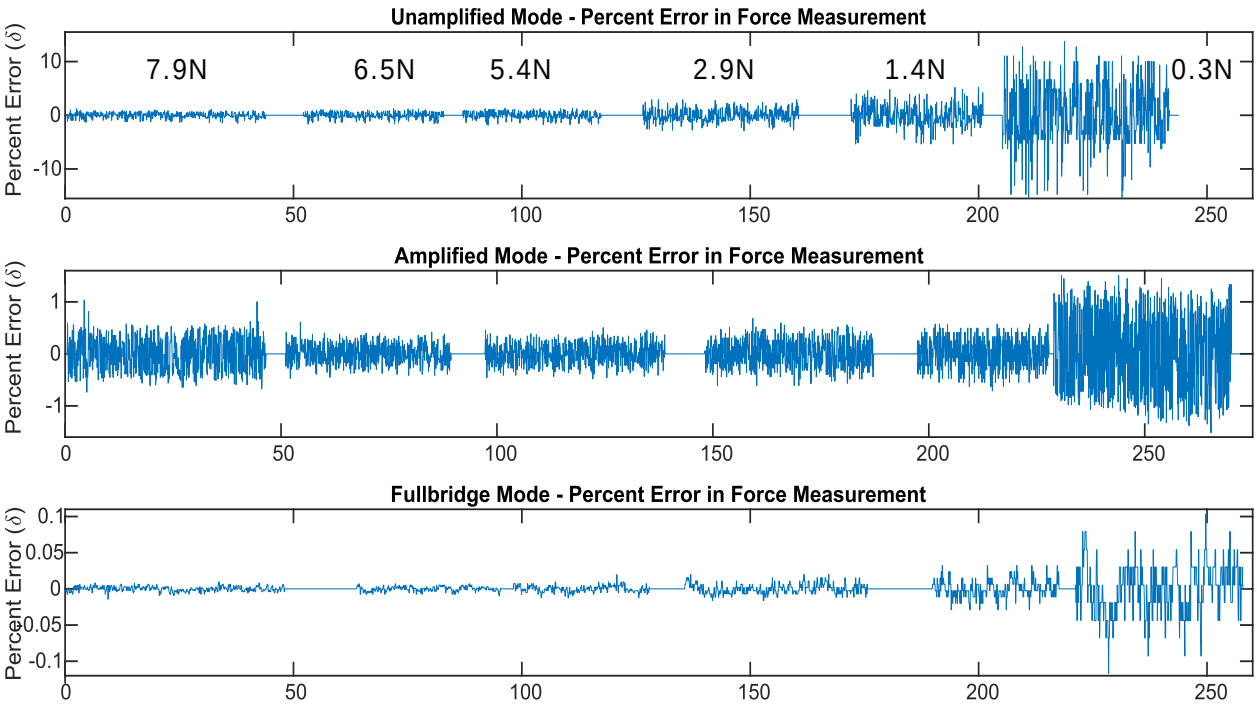

Figure 4.19: Experimental verification of DAQ measurement error (Data:05.dat,06.dat)

and mounted vertically, signal was acquired with DAQ by manually putting the known masses. The error in measurement can be seen in Fig. 4.19, same weights were used for all three connections and plotted against the time. The plots shows the relative error in the measurement and the oscillations due to the error. It is clear from this test that the full bridge mode connection has the least error, typically less than ± 0.05 %. This method has the least error due to pulsed excitation. But the microcontroller can't register this voltage[19] for the PID feedback, so separate preload performance was carried out with the amplified mode. Finally, the fullbridge connection was chosen for the thrust measurement where the error oscillates between ± 0.01 %. For all three methods, the error has inverse correlation with the loading due to the range of measurement necessitating range selection for the measurement, this is discussed in next part.

4.4.2. Measuring Range Selection

As seen in the specification sheet the DAQ is autoranging. There are different measuring ranges and depending on the bit-rate of acquisition the error for each range changes. Main signal types that are being acquired on the DAQ is voltage and force sensor. The voltage reading is used for various sensors and gauges. The Fig. 4.20 shows the analog to digital conversion error for the installed DAQ device. It is evident from the figure that, low voltage gives out highest error. As previously discussed, force sensor is set to use the full-bridge mode of connection for the DAQ. Percentage error in estimating the microstrain has a constant error, this is illustrated in the Fig. 4.21.

It is apparent from these plots that DAQ is more precise in acquiring high voltage and force

[19] Hardware interrupt can be utilized to register these pulses but this will complicate the programming for other functions as force sensor will be always be on, thus interrupting the processes every $100\ ms$

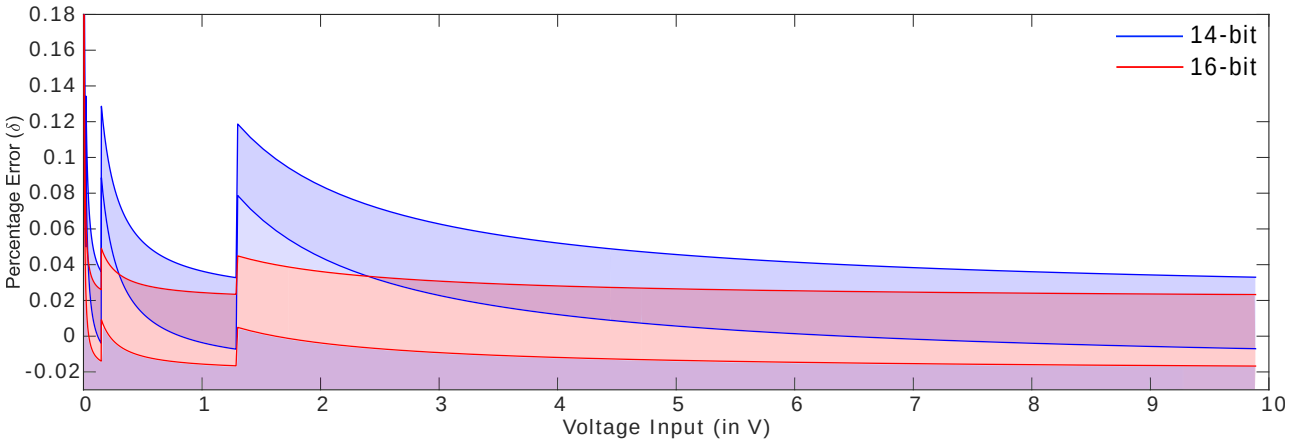

Figure 4.20: Datascan ADC error - Voltage measurement

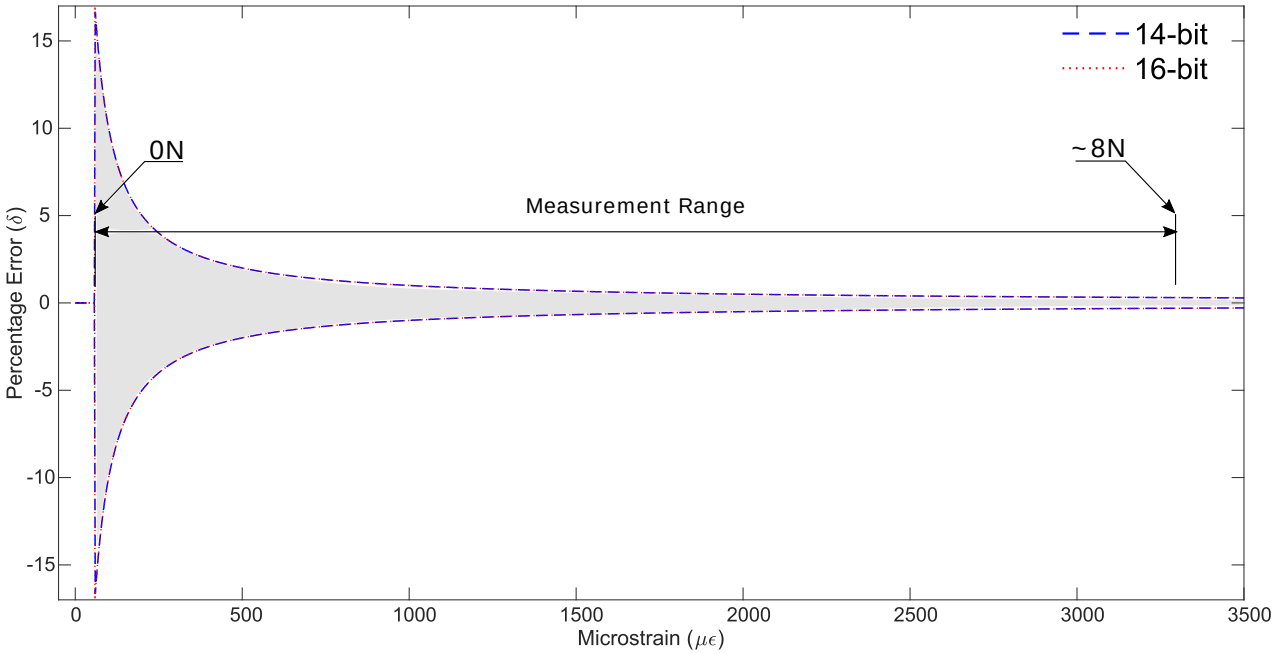

Figure 4.21: Datascan ADC Error - Fullbridge measurement

values. This effect is also visible in experimental verification as seen in Fig. 4.19, as the mass gets lower, the percentage error increases. So the the high measurement range is selected. In case of force sensor, the high measuring range is ensured by preloading the force sensor which will result in giving out higher $\mu\varepsilon$ values. This will result in very low error data acquisition. In case of voltage readings, sensor are chosen carefully that outputs higher voltage or parts of the previously discussed amplifier circuit could be utilized and then the gain can be easily adjusted to get higher higher voltage output, but this method also adds in uncertainty as amplifier circuit also has an error.

4.5. Data Analysis

MATLAB scipts was previously written for interval selection and anlysis of the experiment data, though the process was automated and there was no fine control over the selection procedure, calibration and thrust calculation. And the SX3 test setup is too complicated and parameters and

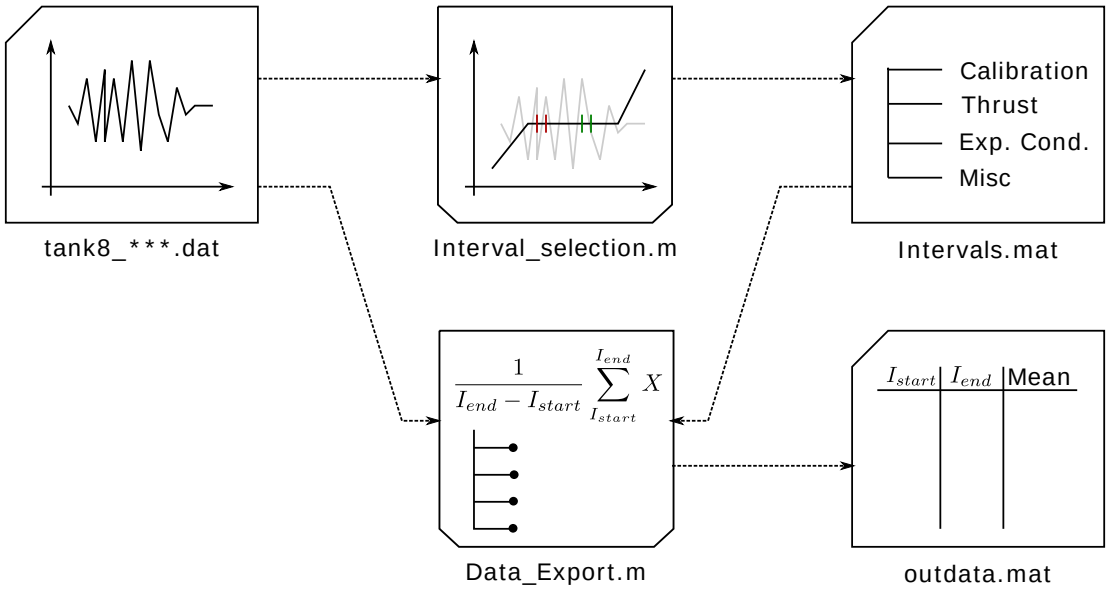

Figure 4.22: Data analysis Matlab

procedures keeps changing all the time, this necessitated complete reengineering of the interval selection and a new data export program. Now the rawdata file `tank8_xxx.dat` is loaded into `Interval_Selection.m`, program then displays all the channels. Careful interval selection then can be made by checking and verifying data over different channels. There are four different interval selections namely, Measurement Data, Thrust measurement, Calibration, Experimental Condition and Misc. They facilitate identifying different interval selections for different analysis. Experiment condition is set in a long duration test where the same data file is used to acquire data for different conditions. Calibration intervals are selected where the calibration are carried out, the newly implemented distance sensor aids in the selection process as it shows slightest of the deflection. Thrust measurement interval is selected before and after turning off the arc current. Misc intervals can be selected for anything that needs special attention. The intervals are then saved in a MATLAB Struct based on the interval selection data, their data point row numbers are saved. Next the `Data_Export.m` script is run and the same rawdata file is provided as input. Based on the interval selection from the previous script, the means are calculated for the intervals and are saved in a MATLAB `.mat` file. The script also does export these data in an Excel file, which improved the readability and accessibility of the data for the analysis process. The script is extensively commented and refer Annex D.1 to know how to access the code.

4.6. Tare Force Measurement Improvement

As previously discussed in 3.6.1, tare force characterization is vital for the thrust measurement and it also evident from Eq. 3.16. The transient magnetic interaction can not be characterized, as a result the transient force change is hard to characterize. The primary interaction that causes these forces is between the applied-field coil and the copper strips that carries the current to thruster and the coil. As there are many current carrying conductors for different parts(can be seen in 3.1.1(4)), they themselves observe the pinch effect[20]. Due to this effect,

[20] A high current carrying conductor induces magnetic field around them and also induces a force which can be calculated by right hand rule. If the conductors carry current in same direction they attract each other or repel if current direction is opposite.

they attract each other. Also, the resultant induced B-field interacts with the coil's magnetic field, making the transient behavior unpredictable. But a quasi-steady state force caused due to these interactions can be characterized by exciting the coil at constant current and measuring the change in the force sensor reading. To further facilitate this measurement and to avoid relative movement, connecting links made from copper plates are implemented between the different strips forcing them to move in the same direction. Detailed description for design of the part is out of scope of this research. But this improvement will affect the tare forces measurement (different from previous test campaign) and it is validated through the experiments(discussed in coming chapter), so it is necessary to take note of the cause.

4.7. Propagation of Uncertainty

Finally, with this improved measurement technique determining propagation of uncertainty is needed to quantify the analytical error for the new technique. The total uncertainty function for the measurement error is given by,

$$f = f_{ADC}(f_{amp}(f_{fs}(f_{mass}))). \tag{4.3}$$

where, $f_{mass} = m_{mass} \pm \Delta m_{instr.}$ is the error function of mass measurement and corresponds to the individual error of the measuring instruments i.e. SHIMADZU self-calibrating precision scale and Kuchenwagge-JBA11041 weighing machine. The Δm represents the error and the values are absolute.

$$\Delta m_{instr.} = \left| \begin{array}{ccc} 0.1mg & & m_{mass} < 220gm \\ 0.01mg & \rightarrow & m_{mass} < 82gm \\ 1gm & & m_{mass} > 220gm \end{array} \right. .$$

Also, the f_{fs} from 4.3 is the error function of force sensor for a applied mass is given by,

$$f_{fs} = f_{mass} \pm 0.1\% f_{mass}.$$

The force sensor output is then amplified and the amplifier error adds into uncertainty, which can be attributed to different electronic components of the amplifier circuit and is given by,

$$f_{amp} = f_{fs} \pm 0.2\% f_{fs}.$$

Finally this signal is fed to DAQ and the ADC error propagates the incoming amplified signal. The error function of the ADC for f_{amp} (in mV)is given by,

$$f_{adc} = f_{amp} + \left| \begin{array}{c} \pm 0.02\% f_{amp} + 0.01\% f_{range} + 1.28 \\ \pm 0.02\% f_{amp} + 0.01\% f_{range} + 0.160 \\ \pm 0.02\% f_{amp} + 0.01\% f_{range} + 0.020 \\ \pm 0.02\% f_{amp} + 0.01\% f_{range} + 0.0025 \end{array} \right. \rightarrow \begin{array}{c} \{f_{range}, f_{fs} \in \mathbb{R} : f_{amp} < 10000\} \\ \{f_{range}, f_{fs} \in \mathbb{R} : f_{amp} < 1300\} \\ \{f_{range}, f_{fs} \in \mathbb{R} : f_{amp} < 150\} \\ \{f_{range}, f_{fs} \in \mathbb{R} : f_{amp} < 20\} \end{array} .$$

If the fullbridge connection is used for the force sensor then the error function is given by,

$$f_{adc} = f_{in} \pm 10.$$

Analytical assessment of the propagation of error puts the current measurement technique in the error range of 0.0213 % of full scale and in terms of force it is approximately $\pm \mathbf{1.0\ mN}$.

4.8. Improved Operating Procedure

With all the improvements and modifications in the test setup and measurement technique, an improved operating procedure is designed. This procedure is optimized for the safety of apparatus and least possible error in the measurement. The procedure is listed below, only consecutive changes in test conditions, if there are any, are mentioned below the procedure. I refers to the arc current and the respective positions of all the microtranslation stages are listed with their position and is denoted with '@'. Same notation from 3.6 is used to reference the characteristic forces for each step and are listed in brackets.

1. Force sensor zero signal acquisition ($F_{t@(t_1)}$)
   Force sensor @ Home, Calibration unit @ Bottom, Distance Sensor @ Set position
2. Magnetization of the setup

   $B = B_{expcond}$ for 15 minutes
3. Decouple the thrust balance

   Calibration unit @ top
4. Ignition condition

   $B = B_{expcond}$, $I_{arc} = 100A$
5. Test conditions - Arc current adjustment ($F_{t@I_{max}}$)

   from $I = 100A$ upto $I = 1000A$ or until cooling onset
6. Force sensor preload ($F_{t@(t_1)} \rightarrow F_{t,pre}$)

   Force sensor @ preload position
7. Preload force signal acquisition ($F_{t,pre}$)
8. Calibration ($F_{t,pre} + F_{m_1} + F_{m_2} + F_{m_3}$)

   Lift up stage @ calibration positions(transient)
9. Arc shutdown $I = 0A$
10. Thrust level signal acquisition ($F_{t@I_0}$)
11. Calibration($F_{t,pre} + F_{m_1} + F_{m_2} + F_{m_3}$)

    Lift up stage @ calibration positions(transient)
12. Thrust balance lock

    Lift up stage @ bottom
13. Homing force sensor and distance sensor

    Force sensor @ home
14. Coil current shutdown $B = 0T$
15. Force sensor zero signal re-acquisition ($F_{s@(t_2)}$)

The new optimized procedure for the SX3 setup can also be seen in the Fig. 4.23.

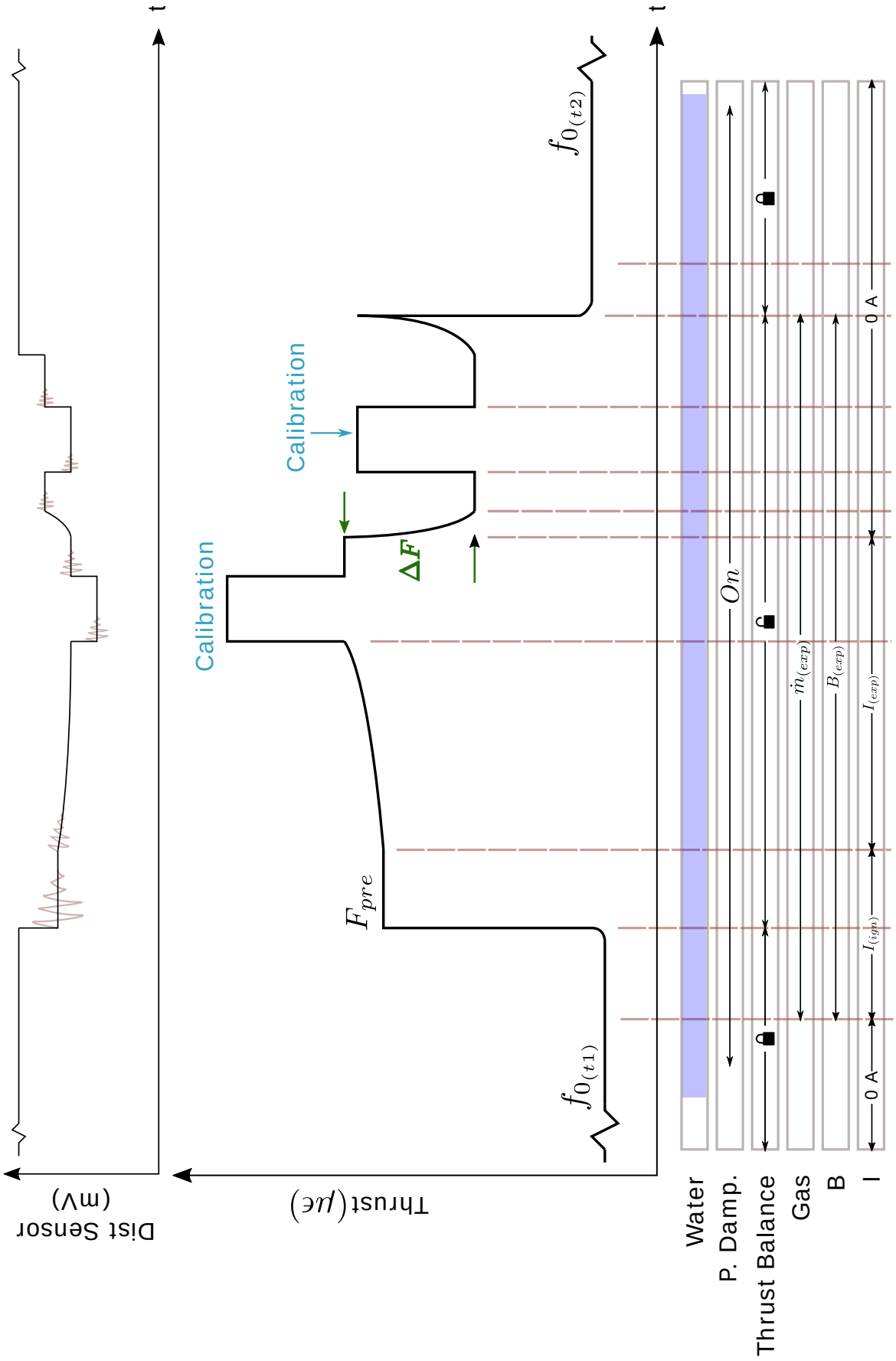

Figure 4.23: Optimized operating procedure, Characteristic forces and Experimental control parameters of an AF-MPD test apparatus

Chapter 5

Experimental Test and Analysis

Various experiments are planned in 2018 test campaign for SX3, thrust calibration is needed to assess the thrust produced. With previously recognized problems and the solution, overhaul was made in the measurement apparatus and number of changes were made in the measurement technique. These changes resulted in improvement of the quality of the measurement and calibration, the analysis of the experiments carried out for the calibration and characterization are discussed in this chapter.

All the experiments discussed here were carried out with the new KD40s-5N sensor connected to DAQ in fullbridge connection mode, if other methods are used it is specifically mentioned. Test procedure was optimized for safety with central safety loop. Wherever specifically mentioned, the thrust balance is locked with mechanical means[1], otherwise the thrust balance is free oscillating after decoupling. Three lead blocks of $11\ kg$ each are used as counterweights for damping. Otherwise mentioned specifically, all the tests were carried out in vacuum.

5.1. Oscillating Mass Approximation

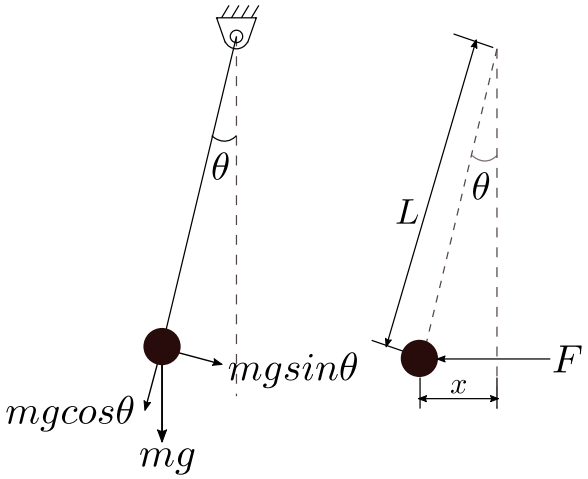

Figure 5.1: Free body diagram of simple pendulum

Previously individual thrust balance components were weighed and the approximate mass was found to be around $175\ kg$ [17]. This mass best represents the physical assembled components

[1] Using nuts and bolts with the frontal locking mechanism

of the thrust balance, but there is always some water in the cooling circuit which changes the oscillating mass, an accurate approximation is needed to calculate dynamic parameters of the thrust balance. The Fig. 5.1 represents the free body diagram of a simple oscillating pendulum. The applied force F causes the mass mg to move by x, trigonometric relations then are used to estimate the mass depending on the displacement. The thrust balance is set to freely oscillate and then calibration is carried out causing a displacement, the distance sensor data is then used to calculate the displacement. The displacement is then adjusted for the force sensor creep, according to data sheet the full scale creep is 0.1 %, assuming the creep is linear through the measuring range, equivalent creep is calculated and added into total displacement.

In reference with Fig. 5.1, for a $L = 150$ mm pendulum, the force applied incurs an angle θ due to x mm displacement and can be formulated as,

$$\sin\theta = \frac{x}{L}. \tag{5.1}$$

Experimentally x is determined with level difference of the reading for a specified force and then this voltage is calibrated using average of factors from Table 4.3 and then it is adjusted for the creep using linear approximation. Resolving the restoring forces for the same pendulum system, we get,

$$m = \frac{F}{g\tan\theta}. \tag{5.2}$$

Force N	Dist sensor mm	x^2 mm	Oscillating mass kg
0.902048	4.16×10^{-2}	4.18×10^{-2}	181.085
0.980529	4.69×10^{-2}	4.71×10^{-2}	184.036
1.01354	4.83×10^{-2}	4.85×10^{-2}	187.101

Table 5.1: Oscillating mass calculation
(Experimental data:#032)

Experiment was carried out and above mentioned method is used to calculate the oscillation mass, results are tabulated in Table 5.1, these calculated oscillating masses are 5 % more to that of the previously measured mass. Considering error in previous measurement, some unaccounted components and the water weight in the system, calculated mass seems more exact, the average of calculated mass 184.074 kg is considered as oscillating mass for further calculations.

5.2. Assessment of Thrust Balance Dynamics

The dynamics of the thrust balance was studied experimentally by moving the calibration masses and acquiring the free oscillation data from the implemented distance sensor(discussed in later chapter). A MATLAB® script was written to analyze the data by applying Fast Fourier transform(FFT) algorithm to identify the frequency of oscillation. As seen in the Fig. 5.2, we can

[2]Represents the total displacement, calibrated distance sensor displacement plus the force sensor creep (2.31×10^{-4} mm for FS)

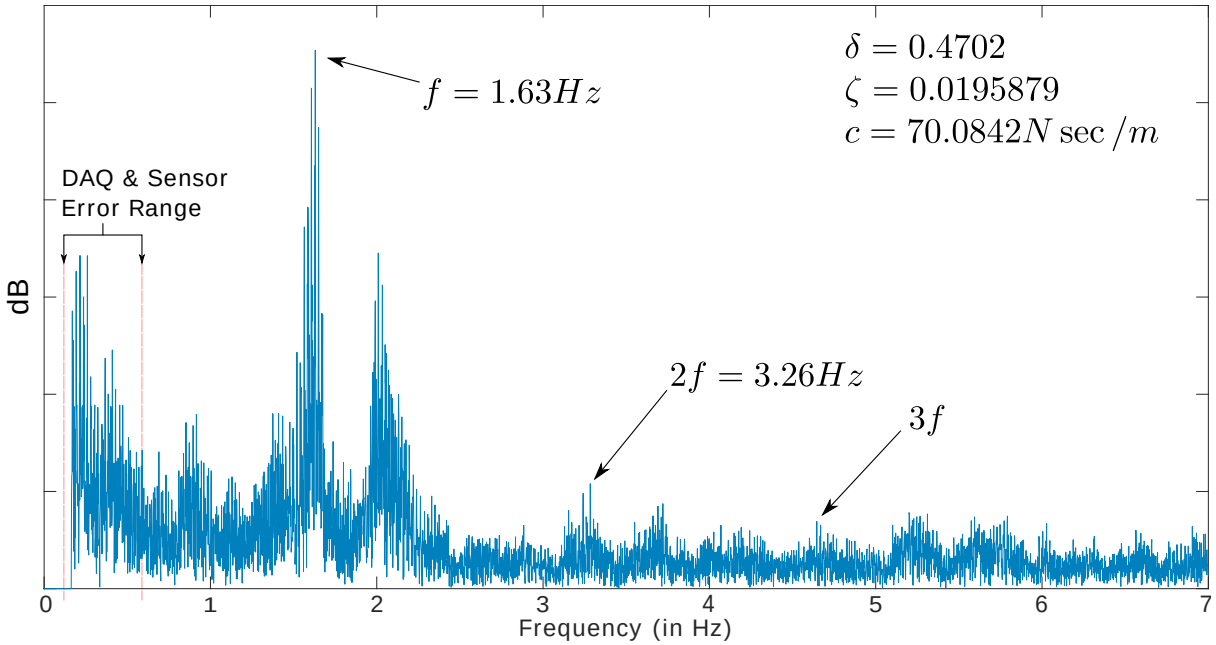

Figure 5.2: Dynamic parameters of the thrust balance
(Experimental data:#032)

see the natural frequency of the free oscillation is $f_n = 1.63\ Hz$. Noticeably, the left marked area in the figure shows peaks for very low frequencies, these are caused by the sensor output error which adds up in the DAQ ADC conversion error. Similarly a secondary peak can be seen just after the natural frequency which is also caused due to the same error. This effect is periodic and can be seen for harmonic partials at $2f$ and $3f$ with a very low amplitude.

For a underdamped system, the free oscillation amplitude(X_n) change over n cycles is given by [5],

$$n\delta = \ln\left(\frac{X_i}{X_{i+n}}\right).$$

Evaluating the amplitude change over 12 cycles, we get the value for logarithmic decrement(δ)as,

$$\delta = 0.4702.$$

With this we can calculate the damping factor and it is given by,

$$\zeta = \frac{\delta}{\sqrt{(2n)^2 + \delta^2}}.$$

This gives $\zeta = 0.0185879$, confirming that the system is underdamped. Now, we use this to calculate the damping coefficient for the thrust balance which is given by,

$$c = \zeta c_c.$$

where, c_c is critical damping factor and for natural frequency of f_n and a mass m it is given by,

$$c_c = 2mf_n 2\pi.$$

Finally, considering the oscillating mass of $184.074\ kg$ as previously calculated and the natural frequency of $1.63\ Hz$ found through the experiment, the value of damping coefficient is found to be,

$$c = 70.0842\ Nsec/m.$$

These dynamic parameters are useful if an active oscillation damping method like voice coil is employed for additional thrust balance movement, this is discussed in last chapter as a design suggestion.

5.3. Vertical Calibration

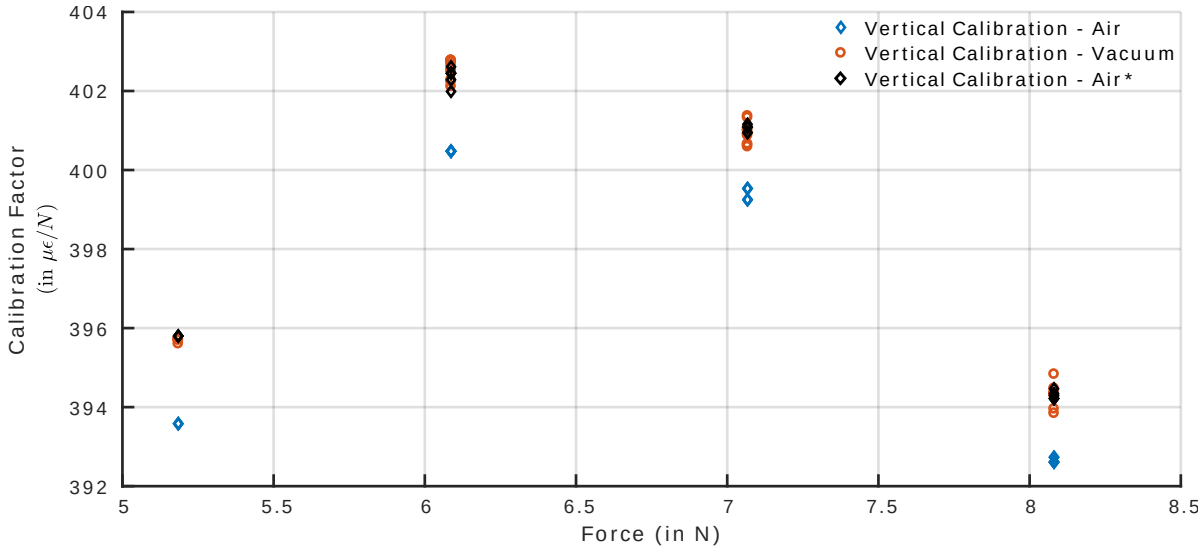

Figure 5.3: Vertical calibration
(Experimental data:#028,#029,#030)

Experiments were carried to to calibrate the output of the force sensor in terms of force. The newly designed vertical calibration mount discussed in 4.1.5 was implemented on the calibration unit. As discussed earlier, this method is the absolute metric of force calibration as 100% of the F_G is transferred to the force sensor. As seen in Fig. 5.3, test was first carried in the air then in vacuum and then again in air (marked in plot as Air*). Various known masses were put on the mount and then removed, this was done multiple times to have good statistical data. The change that is apparent for the same force for different conditions is due to the linearity of the force sensor. From the first air test it took quite a while to evacuate the tank so the linearity drift is large. Whereas the last air test was done within 30 minutes of the vacuum test so the linearity played a very little role and the calibration factors almost coincides with each other. The average vertical calibration factors are also tabulated in Table 5.2.

	Air	Vacuum
Average Calibration Factor	378.033	378.417

Table 5.2: Vertical calibration factors (in $\mu\varepsilon/N$)
(Experimental data:#028,#029,#030)

5.4. Horizontal Calibration

Horizontal calibration refers to calibration of the force when the force sensor is mounted horizontally on the force sensor microtranslation unit and the force is transferred to the thrust balance via thread and pulleys. As previously discussed, the horizontal and vertical calibration factors are not identical due to the mounting orientation of the sensor, friction in the lines and the play in the bearings of the pulleys. As the thrust produced by the thruster acts on the same plane as that of the calibration masses, the force experienced by the force sensor is same as that of the calibration masses. So it is safe to conclude that the factors from these tests can be used to calibrate the force and are presented in Table 5.3.

The horizontal calibration tests were carried out with different force sensor styluses in vacuum. As seen in Fig. 5.4, we can see that the calibration factors for different stylus are more uniform. The tests were carried out independently on separate occasions, so the linearity drift is not present in this calibration. The difference in the factors for the same stylus can be attributed to error in DAQ and statistical error in interval selection. This result is an improvement over the test campaign from last year. Even then these factors are different from the vertical calibration factors. To account for this change a correlation factor is used and is discussed in next part.

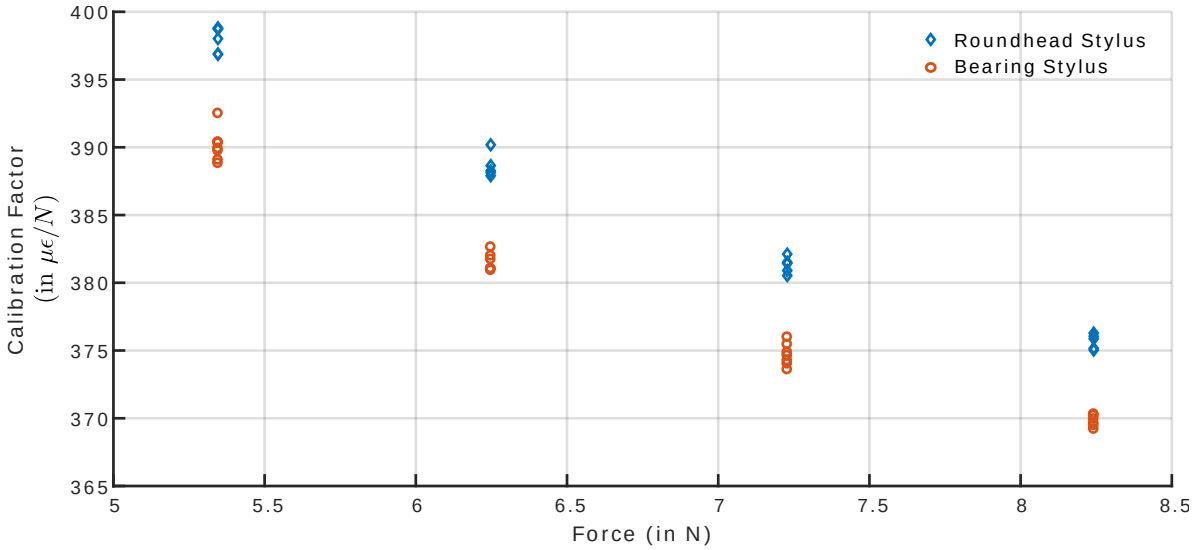

Figure 5.4: Horizontal calibration
(Experimental data:#032,#033,#034)

Stylus	Average Calibration Factor
Bearing	331.966
Roundhead	333.965

Table 5.3: Horizontal calibration factors (in $\mu\varepsilon/N$)
(Experimental data:#032,#033)

5.5. Calibration Correlation & K_{VH}

As previously discussed in 3.6, there is difference between the force that acts on the force sensor when mounted vertically as opposed to when it is mounted horizontally. The cause of this change is friction in the wire with the pulleys, the sideways play in the pulley due to tolerances, single bearing mounting system and most importantly the way strain gauge receives the force. This effect can be clearly seen through the difference in the calibration factors discussed previously. To calibrate the difference out K_{VH} is used for the thrust calculation as seen in Eq. 3.14. The K_{VH} for different styluses are tabulated below.

Stylus	K_{VH}
Bearing	1.139
Roundhead	1.132

Table 5.4: K_{VH} for different styluses
(Experimental data:#025,#028,#029,#030,#032,#033,#034)

5.6. Stylus Selection

Different styluses were tested for the force sensor in air and in vacuum, all the three styluses gave out different calibration factors. The change in factors is significant enough that we can not attribute the change to error in measurement chain or the statistical error in the analysis. The best metric is to choose the stylus which transfers the force closest to that of vertical calibration tests, in turn giving out higher calibration factors. Preliminary tests conducted in air showed that pointy stylus transfers the least force, so it was omitted from further vacuum tests. It can be seen in Fig. 5.4 that the Roundhead stylus has highest calibration factors of all, so the same is chosen for thrust measurement.

5.7. Pulsation Damper

A baseline reading was taken in vacuum without turning on the cooling circuit and then calibration was carried out. Then water pump was turned on and similar calibration was carried out. Lastly pulsation damper was activated and calibration was carried out. For measurement consistency, force sensor was coupled with thrust balance and preloaded to approximately $5N$ every time. The Fig. 5.5 shows the frequency analysis of the oscillations obtained from FFT of the distance sensor data. It clearly shows that pulsation damper improves the oscillations at the natural frequency and harmonic partials by averagely 40%, thus improving the measurement quality. Critically it is more important to characterize the calibration factors for the masses, for each of these routines. The calculated calibration factors from force sensor data are tabulated in Table 5.5.

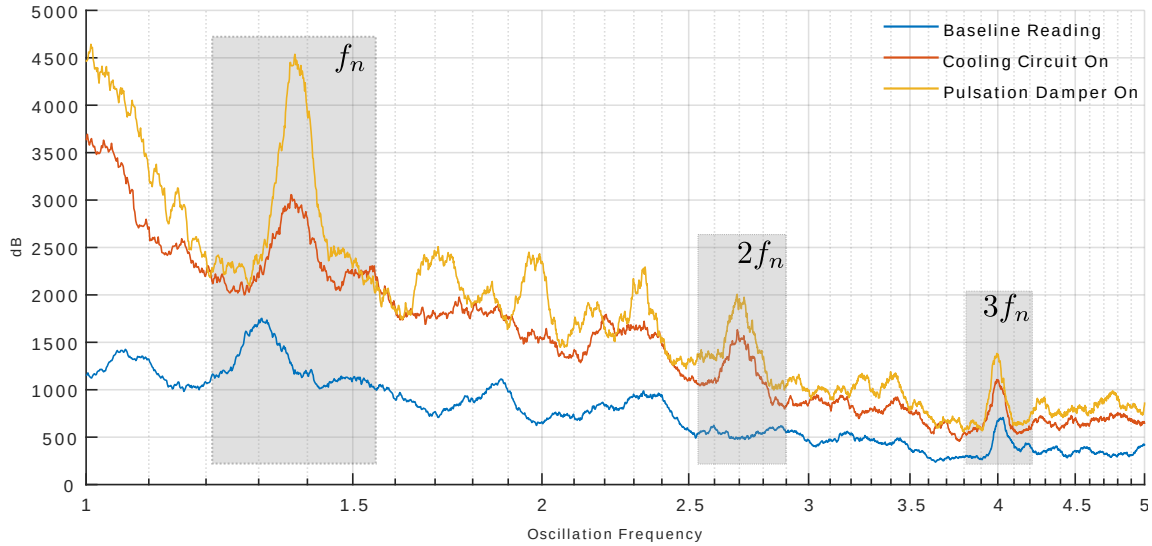

Figure 5.5: Frequency analysis of oscillations - Pulsation damper
(Experimental data:#037)

	Baseline	Water On	Damper On
m1	327.464	328.182	333.727
m2	334.404	349.214	329.424
m3	332.474	333.048	332.415

Table 5.5: Calibration factors (in $\mu\varepsilon/N$) - Pulsation damper
(Experimental data:#037)

5.8. Laminar Flow Filter

Similar to last section, laminar flow filters were tested by taking baseline reading of oscillation due to cooling circuit water and then with laminar flow filters installed. Calibration was carried out for each condition viz. just cooling circuit on, with laminar flow filters installed and then with filters installed and pulsation damper turned on. Force sensor was coupled with thrust balance and same preload was applied for all the conditions. The frequency analysis of the thrust balance oscillations was carried out. The distance sensor data for individual conditions was passed to a FFT function then averaged using moving average algorithm. This representative frequency response for different conditions of cooling circuit can be seen in the Fig. 5.6. Similar to previous test of pulsation damper, using just laminar flow filter shows significant improvement of oscillations at natural frequency and harmonic partials. Using laminar filter along with pulsation damper further improves the oscillations. This improved oscillation performance of the thrust balance as cooling circuit now imparts less oscillations in turn reducing the noise in the force measurement. More importantly the calibration factors, as seen in Table 5.6, is also showing upward trend compared to vertical calibration factors which suggests improved quality of the measurement.

	Baseline	Laminar Filter	Laminar+Damper
m1	327.464	331.563	337.818
m2	334.404	339.843	331.531
m3	332.474	338.143	341.199

Table 5.6: Calibration factors (in $\mu\varepsilon/N$) - Cooling circuit effects
(Experimental data:#037)

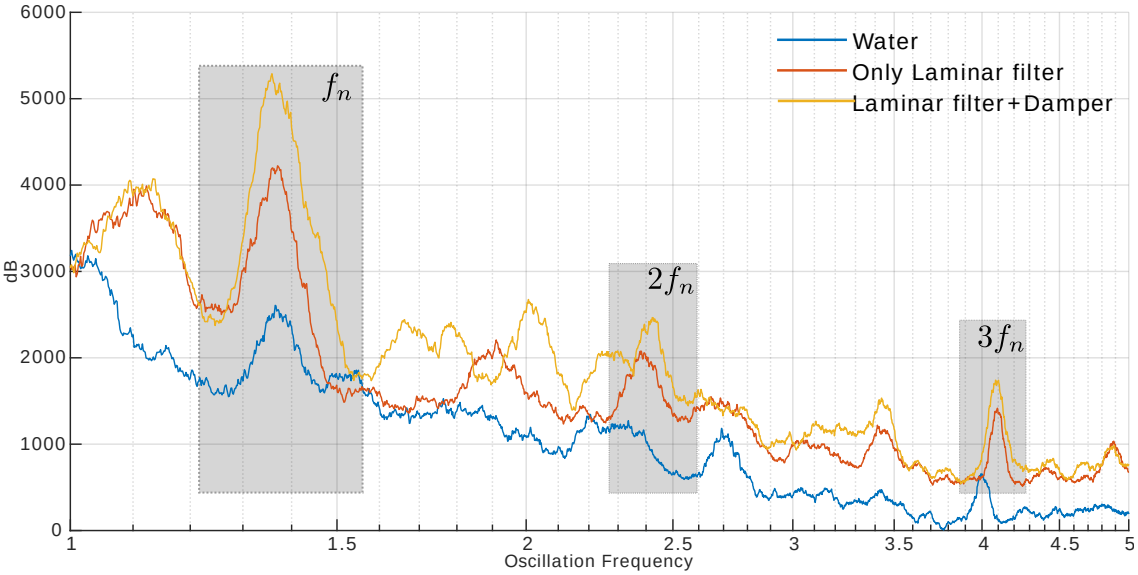

Figure 5.6: Frequency analysis of oscillations - Laminar flow filter and pulsation damper
(Experimental data:#037,#40)

5.9. Force Sensor Linearity

Previously it was observed that the linearity of the force sensor causes the f_0 to change and it is compensated by taking out the slope of the change from the mean data as seen in Eq. 3.12. During the experiments this was characterized and it was found that the linearity change is typically very low and is in the range of $1mN/h$ to $10mN/h$ which is lower than the accuracy of the measurement chain. Moreover one experimental condition's test is carried out in around $10-15min$ and the linearity observed is too small to account for in measurement. Moreover, the interval selection program facilitates accurate selection of adjacent data which further ensures very less relative error due to the linearity. Conclusively, it is safe to assume that the linearity change can be ignored from the thrust calculations.

5.10. Preload Thermal Drift

As the current increases, the thermal load of the system increases causing the water in the cooling circuit to heat up, in turn the PA pipes also heats up and that changes the stiffness of the pipes. As described earlier, this cooling circuit acts as a spring. With varying stiffness, the characteristic force (F_{spr}) changes causing the preload force (f_{pre}) to change. This effect can be seen in Fig. 5.7, even though there is an increase in the preload force, the change is linear with

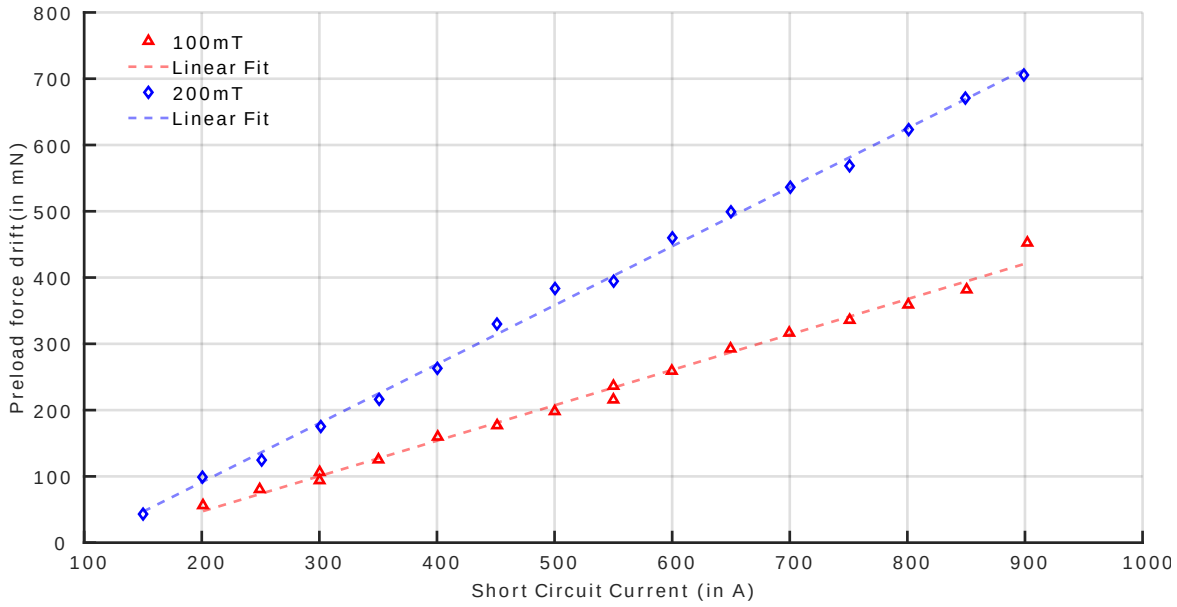

Figure 5.7: Thermal drift of the preload force from initial preset
(Experimental data:#048,#049)

the arc current(or short circuit current). Because of the linear trend in the preload drift, we can select the f_{pre} interval adjacent to the measurement interval and this preload drift wont induce any error in the thrust measurement.

5.11. Tare Forces

The magnetic interaction between the Applied field coil and the current carrying conductors causes forces to act on the thrust balance. These are essential to be characterized as they are significant and should be account for, as part of the thrust calibration process, this is also apparent in Eq. 3.16. Tare forces are characterized by using a short circuit interlink between thruster's anode and cathode and applying the current to the coil. In the experiments conducted, $150mm$ interlink is used to simulate analogous the arc length. Initial testing showed erratic and non-linear behavior of the tare forces even with the physical modifications made in the current decoupling unit. Previous research presented a solution of premagnetization the experimental setup. Long magnetization of diamagnetic and paramagnetic materials of the thrust balance components induces acute magnetic hysteresis and the interaction caused is then linear. Premagnetization is carried out before the actual ignition of the thruster, as the thruster keeps operating the B-field continues to magnetize the setup keeping the tare force constant. Different premagnetization time was tried out and conclusively the setup was premagnetized for $15min$(optimum time) with same B-field as that of experimental condition.

The plots of tare force characterization can be seen in Fig. 5.8,5.9,5.10 and they all show a linear trend due to premagnetization and changes made to the current decoupling unit. Previously there was a sudden drop around $600A$ for $400mT$ which propagated through whole thrust measurement and affected the accuracy of the measurement, compared to that current calibration method will lead to a very precise thrust characterization. The $F_{T@B}$ for different coil strengths are tabulated in Table 5.7 which represents the regression equation of the linearity of the data points. This table can be used to quickly calculate tare forces at individual B-field

strength for I_{arc} of arc current. Characterizing tare forces for $400mT$ was not possible due to cooling onset.

B-field (in mT)	$F_{T@B}$ (in mN)
100	$F_{T@100} = -0.0006 \cdot I_{arc} - 0.0005$
200	$F_{T@200} = -0.0012 \cdot I_{arc} + 0.0032$
300	$F_{T@300} = -0.0017 \cdot I_{arc} - 0.0372$

Table 5.7: Tare force $F_{T@B}$ for I_{arc} Arc current (in A)
(Experimental data:#045,#046,#048,#049,#050)

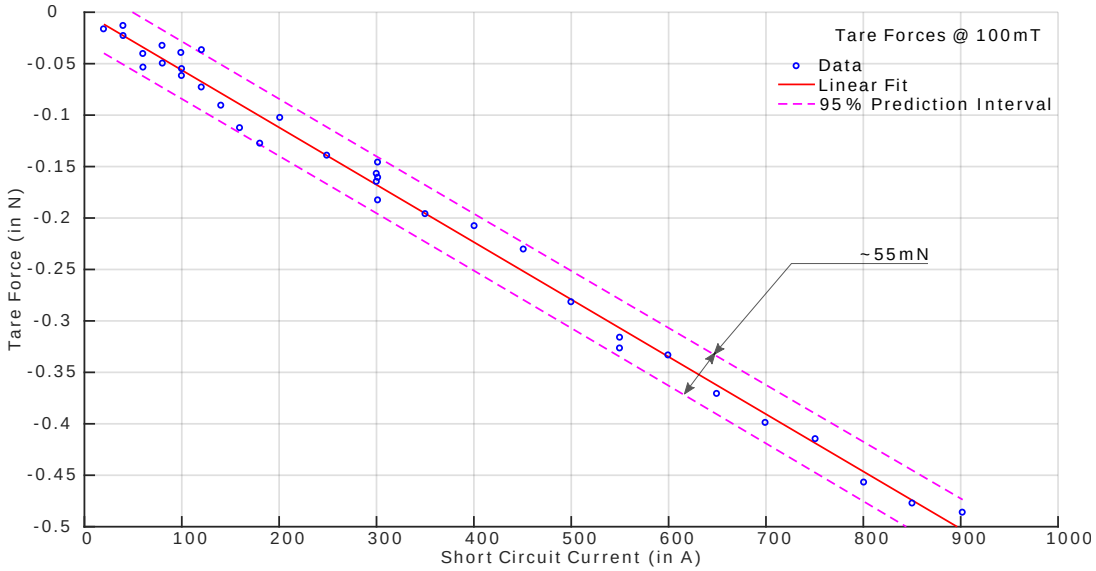

Figure 5.8: Tare forces for $B = 100mT$
(Experimental Data:#045,#046,#048)

5.12. Discussion

All the improvements in the measurement technique and experimental setup has enhanced the quality of the trust characterization and calibration. How these improvements changed commonly identified thrust stand performance metrics [23] are discussed here after.

Sensitivity

Sensitivity of the hanging pendulum primarily depends on the length of the pendulum arm [14], longer the pendulum arm higher is the oscillation frequency, in turn increasing sensitivity to the applied force. In case of SX3's thrust balance it is $150\ mm$ and no changes have been made to alter the sensitivity of the thrust balance, but as previously discussed thrust balance is already very sensitive and is susceptible even to building vibrations.

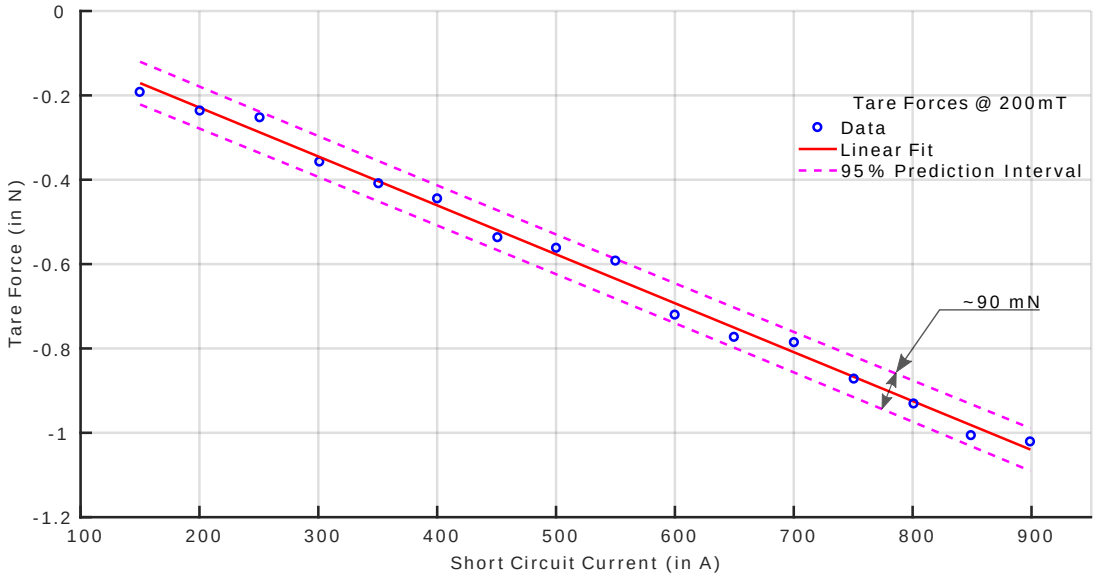

Figure 5.9: Tare forces for $B = 200mT$
(Experimental data:#049)

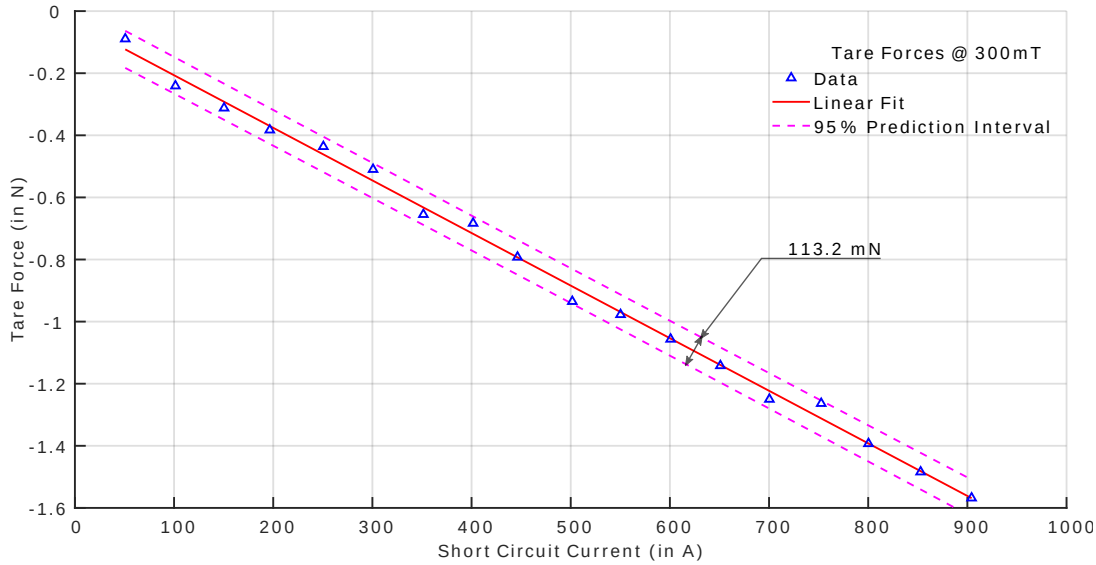

Figure 5.10: Tare forces for $B = 300mT$ (Experimental data:#050)

Repeatability

The use of electronics control in thrust calibration procedure has ensured the repeatability of the calibration. Linearity of the sensors employed to measure or aid the thrust measurement has no to insignificant role. Thermal drift of the preload force has linear characteristic and immediate interval selection will ensure no error in the measurement. Numerous tests and experiments show that the thrust balance repeatability has been improved due to precise characterization.

Accuracy

The errors in the thrust measurement chain is characterized and are quantified. Attempts are made to mitigate them with modification in the test setup. An optimized operating procedure is

determined for effective least error in the measurement. By preloading the force sensor high error regime of the DAQ is avoided in turn the accuracy is increased. Comparative analysis and selection of force sensor stylus enriched the force transference, reducing the error due to horizontal mounting of the sensor.

Propagation of uncertainty is studied for the static measuring chain which gives analytical error of $\pm 1.78\ mN$ which agrees with the experimental verification of $\pm 1.56\ mN$ for selected measuring range and method. Cooling circuit imparts vibrations on to the thrust balance and previously the oscillations typically added $\pm 800\ mN$ over the mean force, the flow irregularities further made the oscillations erratic. Implementation of pulsation damper and laminar filter arrested the pressure fluctuations and shocks which smoothened the flow and resulted in improving dynamic performance of thrust balance at the natural frequency. Distance sensor data shows great improvement in the thrust balance movement, it almost moves like free oscillating balance even with the cooling circuit turned on. With these changes, qualitative acquisition of force sensor data is assured because of the better oscillation performance. The cooling circuit now adds roughly $\pm 325.379\ mN$ over the mean force.
Selective quality data now has an average error of $\pm 145.147\ mN$, this is also the approximation of accuracy of the thrust balance coupled with preloaded force sensor and active high pressure cooling circuit.

Resolution

The force sensor data is acquired with 16 bit resolution, so for the static measuring chain the resolution is around $1.8834 mN$. For the actual thrust measurement setup, the resolution is affected by the high oscillations and determining exact resolution is difficult. Very crude approximation of the noise is taken out from the data and then some margin is added to it. Roughly $19.875\ mN$ is inferred to be the resolution the thrust balance.

Noise

Experimentally it is observed that the operation of the motors on the microtranslation stage adds very low amplitude noise typically in the range of $\pm 8\ mN$. Probable cause of this is GND interference of DAQ or shield interaction or EM interaction at feedthrough. Even though the noise is less than the resolution of the system, motor drivers are programmed carefully not to operate the motors between the acquisition period. Later, careful interval selection avoiding the translation region of the thrust balance will further assure noise plays no part in the measurement error. On the other hand, thruster's arc current and the strong B-field of the coil does not add any noise in the measurement.

Response Time

The thrust balance is very responsive and has almost negligible rise time and typically the settling time for $80\ \%$ of the overshoot(over mean force) is around $14\ s$. Electronics controller ensures longer calibration period to collect sufficient data points to reduce statistical error.

5.13. Further Improvement Suggestions

The results previously discussed has now made the thrust characterization and measurement more credible and repeatable. Even then some potential areas are found and further research is likely to further improve the measurement quality. These suggestions are drawn from problems faced while performing experiments and trends in recent research.

5.13.1. Active Damping

As previously determined there are significant oscillations in the force sensor signal, a voice coil and a permanant magnet mounted on the thrust balance can be employed to activeley damp the thrust balance oscillation. Even though the low amplitude and low frequency oscillations caused due to cooling circuit will not be perfectly damped. Even then, just by damping the natural oscillations of the balance the quality of data acqusition will increase multifold. Also recent studies has shown that force can also be calibrated using the same technique [10], a secondary verification method for calibration can also be implemented using the proposed setup. The basic premise to use the voice coil is that it is lightweight and will not add into the balance mass, this is critical factor for high resolution low range thrust balance. But as seen in the experiments the oscillations goes around $250\ mN$ in some region, this voice coil along with magnets should be able to produce the damping force in similar ranges or even more. But as the method uses magnets, the damping behavior in presence of strong B-field of coil might get affected and needs to be addressed.

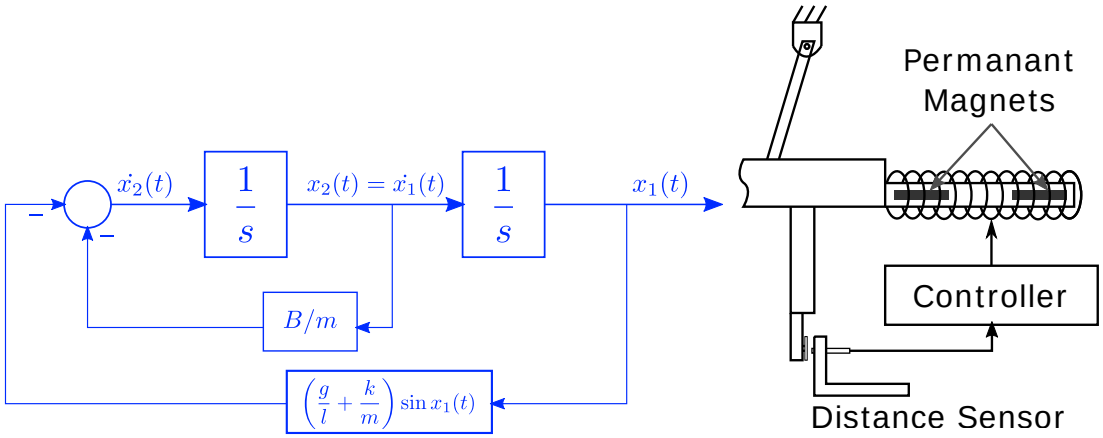

(a) Block diagram of the thrust balance

(b) Voice Coil

Figure 5.11: Active oscillation damping with voice coil

The thrust balance is modeled considering it as a mass, spring, damper system hanging on a simple pendulum and the block diagram of state variables of the system can be seen in 5.11a. For a thrust balance of mass m (kg) is hanging from pivot at length of l (meters), the applied force F induces an angular displacement θ from the equilibrium position and assuming viscous damping by gravity with the damping coefficient of B $(N - sec/m)$, the tangential velocity component $l\dot{\theta}$ restores the equilibrium, simplifying the system we get,

$$\alpha + \frac{B}{m}\omega + \left(\frac{g}{l} + \frac{k}{m}\right) \sin\theta = 0. \tag{5.3}$$

This equation along with block diagram can be used to code the PID logic of the controller that excites the voice coil, giving accurate active damping of the system. The transient performance of the model was tested in the MATLAB Simulink and can be seen in Fig. A.2.

5.13.2. Liquid Current Decoupling

The current decoupling unit currently employs copper strips for power delivery to the thruster and the coil. They experience Joule heating which changes the stiffness of the strips inducing a time varying force on the thrust balance. Especially hollow cathode configuration that is planned will increase this effect drastically as the heater and keeper circuit uses very high current levels. Way to reduce this effect is to use pool of liquid metal to feed the power, as the feed lines always float in the pool, it will not induce significant force on the thrust balance. Commonly tried liquid metals for this purpose are Mercury and Gallium. But using Mercury is hazardous for the setup and the environment, so use of Gallium or Galinstan alloy pools are suggested for the current decoupling.
But there are also known issues with this system, as the current increases, liquid metal heats up and changes the viscosity of the liquid metal which is similar to changing stiffness but the effect should be comparatively smaller. This will also affect the tare forces due to different diamagnetic properties of the Gallium, further characterization of such setup is warranted.

5.13.3. Better Pulsation Damper

The pressure fluctuation damper implemented does improve the dynamic performance of the thrust balance. But the throughput of the damper is simply not big enough to arrest considerable fluctuations and it is evident from the experiments. A bigger throughput damper is suggested to further improve the flow. An active damper can also be implemented that uses PID controller and actively adjusts the gas pressure in the bladder based on the pressure fluctuation change measured with a pressure gauge attached to the flow line.

5.13.4. Vibration Isolation

The thrust balance is quite sensitive and extremely susceptible to background vibrations and can also be seen visually in the distance sensor data. It induces noise in the force sensor data. Slightest of stomping on the floor is also visible on the force sensor, so is closing and opening of the lab door. Vibrations of the pump can also be felt on the tank surface, so the thrust balance needs to be better isolated from the support structure reducing transference of vibration to the thrust balance. Simplest way would be to add big rubber washers at the mounting points. But rubber washers may cause outgassing. Careful selection of the washer material can avoid this issue, FKM elastomers or Silicone rubber could be good considerations.

Chapter 6

Conclusions and Summary

Drawing motivation from the measurement inconsistencies found in tare force measurement of SX3 AF-MPD thruster, the main goal of this study was to improve the thrust balance and characterize the measurement technique. Based on the problems identified significant modifications and improvements have been made in order to guarantee accurate thrust measurement and thrust characterization. These include implementation of improved translation stages for calibration, new distance sensor, new force sensor stylus tips, cooling circuit improvement with laminar flow filters with pulsation damper, a new programmable electronic control unit for calibration and thrust measurement procedure. Modifications and optimizations were also made in thrust measurement chain, test operating procedure and MATLAB analysis tool.

The error sources at each stage of the thrust measurement chain were identified and partly compensated or quantified precisely. Propagation of uncertainty was studied and experiments identified the fullbridge connection as the least erroneous. The main reason being the force sensor circuit is supplied with precise $1.8\ V\ 8\ ms$ pulses which circumvents the self heating effects reducing error propagation due to linearity of the force sensor. To account for DAQ ADC conversion error preloading of the force sensor was realized which reduced the acquisition error for selected method by $80\ \%$ for the selected preload of $5\ N$. Preloading of the force sensor was originally designed to be controlled with PID for fine control of preload preset. But the current gear ratio of 1:1526 makes it impossible to carry out preloading within the time constraints of test due to slow movement. So, now the preloading is done manually and PID control can be revisited with a new gearbox with low gear ratio of 1:64. Thrust balance statics and dynamics was studied analytically with the help of free body diagrams and experiments, as a result the free oscillation frequency of $1.63\ Hz$ and a precise mass approximation of $184\ kg$ was found. Finally, the equations that bounds all the characteristic forces of the thrust balance and the thrust calculation procedure are listed.

Distance sensor implemented on motorized translation stage is serving multiple use in the measurement technique. It was also tested to be used as an indirect thrust measuring technique. Even though quality of the distance sensor signal is better than force sensor, the preloading of the force sensor changes the damping of the thrust balance limiting the distance sensor output to few hundread millivolts. So, the distance sensor is only used as a feedback, analysis and characterization technique. Different stylus tips were designed for the force sensor in order to characterize potential influence of vertical displacement of thrust balance. The roundhead stylus tip is chosen for the final measurement technique as it is more close to vertical calibration

factors. This research has also gone towards enhancing the influence of horizontal calibration by improving the force transference characteristics with design improvements like friction reduction, improved ceramic bearings and characterization. Because of these improvements the correlation between static vertical and horizontal calibration factors are in the range of approximately $11.75\ \%$ compared to previous $23.72\ \%$ [7]. With number of experiments, it was found that calibration using three masses versus just one mass does not affect the accuracy, so the calibration procedure now only implements one mass change reducing time required in the test procedure by $30\ s$ each test. The relevance of laminar flow filters and pulsation damper in improving the cooling circuit is validated by the experimental findings. The spectrum of oscillations due to the cooling circuit was spread out along wide frequency range. These additions in cooling circuit has significantly improved the oscillation performance of the thrust balance by almost $200\ \%$ at natural oscillation frequency and also the calibration factors are now within $10.63\ \%$ of vertical calibration. More importantly, the overall accuracy of thrust measurement for qualitative data is found to be $\pm 145.147\ mN$ with a resolution of $19.875\ mN$ and approximate noise around $\pm 8\ mN$.

The implementation of fully programmable electronic unit to control translation stages used for thrust measurement and calibration gives more flexibility to the measurement procedure. PCBs were designed from scratch to host the microcontroller and stepper motor drivers. Other sybsystems like PPU, user interaction switches and OLED display were prepared, assembled and programmed. The control unit can operate 3 stepper motors of translation stages with microstepping upto 256 giving very fine control over positioning via programming, with this the selected resolution of some of the translation is roughly in order of sub-micrometer. The programming of the motor control is optimized in a way to ensure high speed translation and safety of the setup. This new electronic calibration and measurement technique have an advantage of ensuring the accurate and reliable repeatability of the measurement.

Tare forces caused due to electromagnetic interaction between the conductors and applied-field coil imparts a negative force on the force sensor. So, it is an important factor for the AF-MPD thruster's thrust calculation that needs a precise quantification. Previous experiment's findings showed a non linear behavior of tare forces. This inconsistency was mitigated through design changes in the current decoupling unit and premagnetization of the setup was added in the operating procedure. With these modifications, the presented study has made significant contributions in improving the trend of the tare forces more towards linear behavior across all tested applied-field's magnetic strengths and arc currents.

The MATLAB based analysis tool was rewritten to give more control over the interval selection and analysis process. The new code structure for this tool is easy to adapt for changes like number of channel data, their order. The new version has also reduced code complexity as the automated thrust calculation part was taken out while retaining the core functionality. A new script was also written to export the mean data to an Excel file in effortless readable format, enhancing further the data analysis for thrust calculation.

In depth assessment of the influences within the setup and the experimental data led to a suggestion of implementing a voice coil for active damping of the thrust balance. This will lead to active damping of cooling circuit oscillations and seismic noise, resulting in improved quality of the force sensor signal. This investigation has paved a way for extensive experimental campaigns for complete characterization of the SX3 thruster.

Bibliography

[1] A. Boxberger. Experimentelle Untersuchung des Magnetoplasmadynamischen Fremdfeldtriebwerkes AF-MPD ZT1. Diplomarbeit - in german, Universität Stuttgart, 2011.

[2] A. Boxberger, P. Bambach, G. Herdrich, S. Fasoulas, M. Merino, and E. Ahedo. Experimental investigation of steady-state applied-field magnetoplasmadynamic thrusters at institute of space systems. *48th AIAA/ASME/SAE/ASEE Joint Propulsion Conference and Exhibit 2012*, (August):1–10, jul 2012. doi:10.2514/6.2012-4012. URL http://arc.aiaa.org/doi/abs/10.2514/6.2012-4012.

[3] D. Cui, F.-Y. Kong, and D. Liang. Pressure fluctuation and its influencing factors in circulating water pump. *J. Cent. South Univ*, 20:149–155, 2013. doi:10.1007/s11771-013-1470-6.

[4] D. Haag, M. Auweter-Kurtz, M. Fertig, and H. Kurtz. Development of an Applied Field Magnetoplasmadynamic Thruster Design Supported by Numerical Simulations at IRS. *29th International Electric Propulsion Conference*, pages 1–14, 2005. URL http://erps.spacegrant.org/uploads/images/images/iepc{_}articledownload{_}1988-2007/2005index/059.pdf.

[5] D. Inman. *Engineering Vibration*. Pearson, 2014. ISBN 9780132871693. URL https://books.google.de/books?id=OCg-XwAACAAJ.

[6] R. G. Jahn. *Physics of Electric Propulsion*. McGraw-Hill Book Company, 2006. ISBN 978-0486450407. doi:10.1115/1.3564751.

[7] P. Jüstel. *Charakterisierung des stationär betriebenen magnetoplasmadynamischen Fremdfeldtriebwerks SX3*. Master thesis - in german, Universität Stuttgart, 2017.

[8] A. D. Kodys and E. Y. Choueiri. A Critical Review of the State-of-the-Art in the Performance of Applied-field Magnetoplasmadynamic Thrusters. *41st AIAA/ASME/SAE/ASEE Joint Propulsion Conference & Exhibit*, (July):1–23, 2005. doi:10.2514/6.2005-4247.

[9] G. Krulle, M. Auweter-Kurtz, and A. Saosh. Technology and Application Aspects of Applied Field Magnetoplasmadynamic Propulsion. *Journal of Propulsion and Power*, 14:754–763, 1998. URL https://doi.org/10.2514/2.5338.

[10] J. K. Lam, C. Koay, H. Lim, and K. H. Cheah. A voice coil based electromagnetic system for calibration of a sub-micronewton torsional thrust stand. *Measurement*, 131:597–604, 2019. doi:10.1016/j.measurement.2018.09.029. URL https://doi.org/10.1016/j.measurement.2018.09.029.

[11] R. I. Loehrke and H. M. Nagrib. Control of Free-Stream Turbulence by Means of

Honeycombs: A Balance between Suppression and Generation. *Journal of Fluid Engineers*, 98(3):342–351, 1976. ISSN 00982202. doi:10.1115/1.3448313.

[12] J. L. Lumley and J. F. McMahon. Reducing Water Tunnel Turbulence by Means of a Honeycomb. *Journal of Fluids Engineering*, 89(4):764–770, 1967. ISSN 00219223. doi:10.1115/1.3609700.

[13] M. Margolis. *Arduino Cookbook*. Oreilly and Associate Series. O'Reilly Media, Incorporated, 2012. ISBN 9781449313876. URL https://books.google.de/books?id=nxxKNCYXRIwC.

[14] T. E. Markusict, J. E. Jones, and M. D. Cox. Thrust Stand for Electric Propulsion Performance Evaluation. In *40th AIAA/ASME/SAE/ASEE Joint Propulsion Conference*, page 10, Fort Lauderdale, Florida, 2004. NASA Marshall Space Flight Center, NTRS, NASA. doi:http://hdl.handle.net/2060/20040085923.

[15] C. Mayigué. *Numerical investigation of MPD thrusters using a density-based method with semi-discrete central-upwind schemes for MHD equations*. PhD thesis, UNIVERSITÄT BREMEN, 2018. URL https://elib.suub.uni-bremen.de/edocs/00106724-1.pdf.

[16] MeasurementSystemsLtd. Datascan Installation and User Guide. https://www.measurementsystems.co.uk/docs/DSCANUSR.pdf. Accessed: 2018-01-12.

[17] J. Miralles. *Experimental Characterization of Steady-State Applied-Field Magnetoplasmadynamic Thruster SX3*. Master thesis, Universität Stuttgart, 2016.

[18] R. Narasimha and K. R. Sreenivasan. Relaminarization of Fluid Flows. *Advances in Applied Mechanics*, 19(C):221–309, jan 1979. ISSN 00652156. doi:10.1016/S0065-2156(08)70311-9.

[19] Odunlade Emmanuel via CircuitDigest.com. Introduction to bit banging: Spi communication in arduino via bit banging. https://circuitdigest.com/article/introduction-to-bit-banging-spi-communication-in-arduino-via-bit-banging. Accessed: 2018-09-24.

[20] PipeFlowCalculations.net. Pressure drop in pipe calculator. http://www.pipeflowcalculations.net/pressuredrop.xhtml. Accessed: 2018-03-09.

[21] PJRC. Teensy Loader Application. https://www.pjrc.com/teensy/loader.html, . Accessed: 2018-09-24.

[22] PJRC. Teensy Technical Specifications. https://www.pjrc.com/teensy/techspecs.html, . Accessed: 2018-02-10.

[23] J. E. Polk, A. Pancotti, T. Haag, S. King, and M. Walker. Recommended Practices in Thrust Measurements. In *The 33rd International Electric Propulsion Conference 2013*, pages 1–24, 2013. doi:http://www.iepc2013.org/get?id=441.

[24] T. D. Schmidt and M. Auweter-kurtz. Adequate Electric Propulsion System Parameters for Piloted Mars Missions. *Proceedings of the International Electric Propulsion Conference 2005 (IEPC05)*, pages 1–12, 2005. URL http://erps.spacegrant.org/uploads/images/images/iepc{_}articledownload{_}1988-2007/2005index/219.pdf.

[25] SyncChannel. Whetstone Benchmark for Arduino. https://gist.github.com/SyncChannel/1e509ae9e8a34cc1e56a. Accessed: 2018-02-10.

Annex A

Extra Plots

A.1. Voltage Divider Error

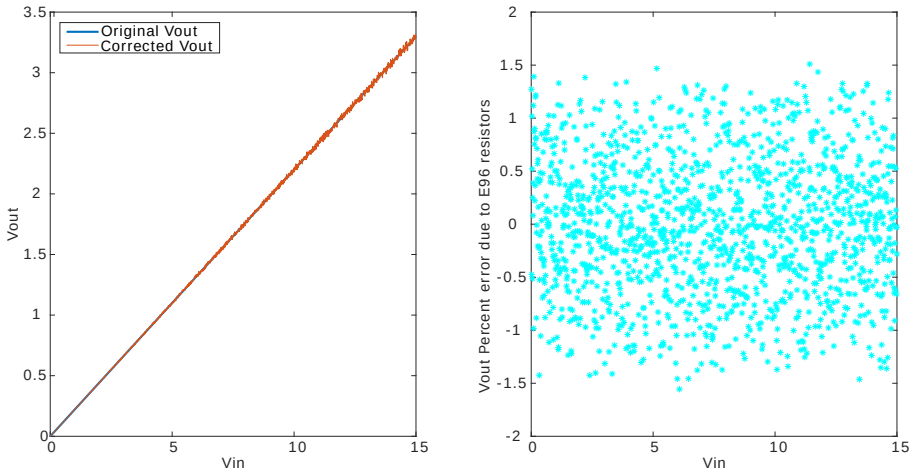

Figure A.1: Voltage divider output error due to E96 tolerance

A.2. Active Voice Coil Damping Performance

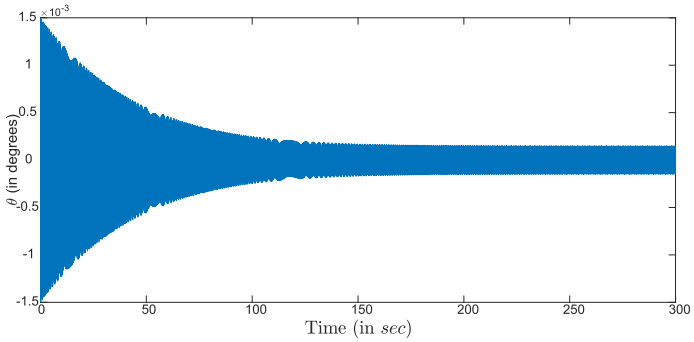

Figure A.2: Active Voice Coil Damping Performance

Annex B

Thrust Balance Lengths Measurement

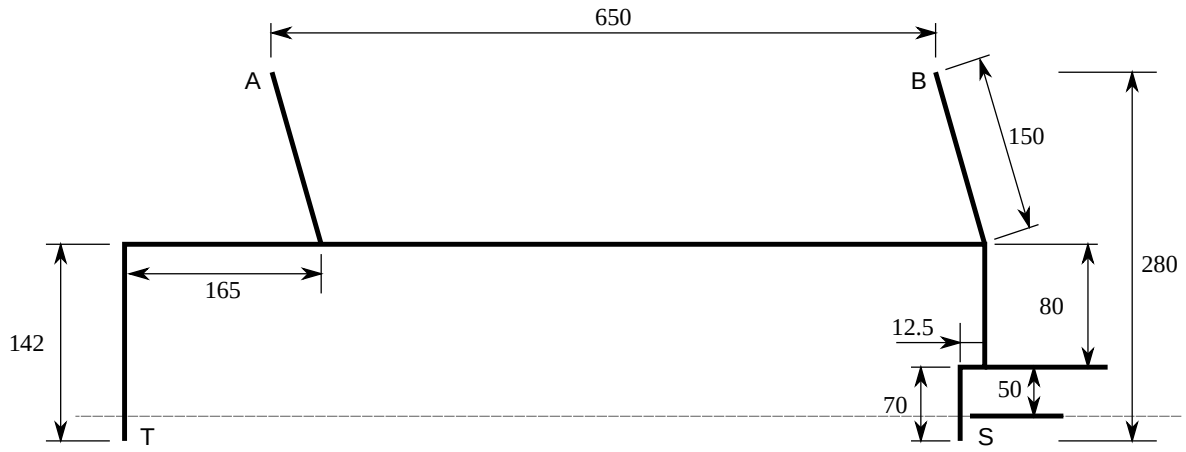

Figure B.1: Characteristic length measurements of SX3 AF-MPD Thrust Balance Apparatus (all measurements are in mm)

Legend

- **T** Thruster
- **A,B** Pivot points
- **S** Sensor

Annex C

Electronic Schematics

List of Schematics

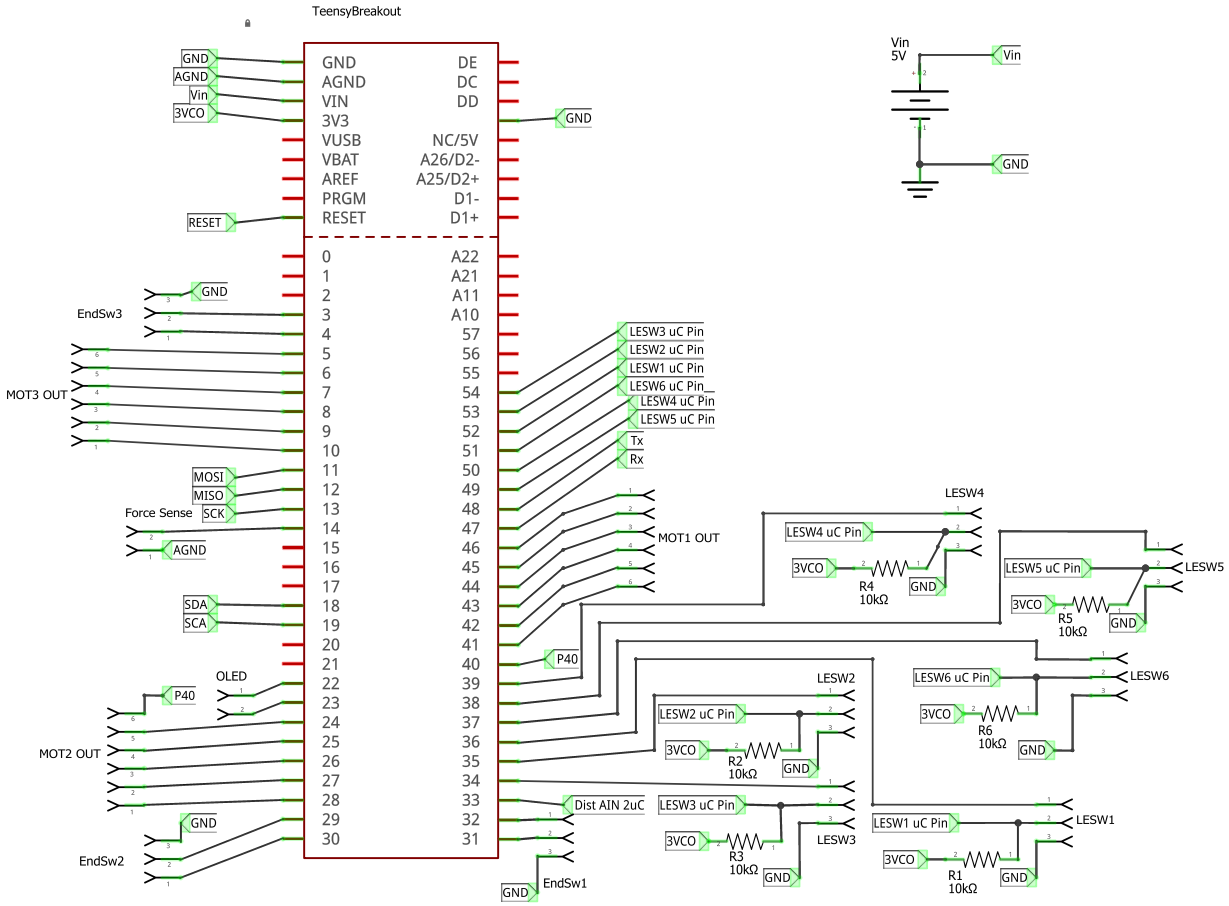

Communications Interfaces

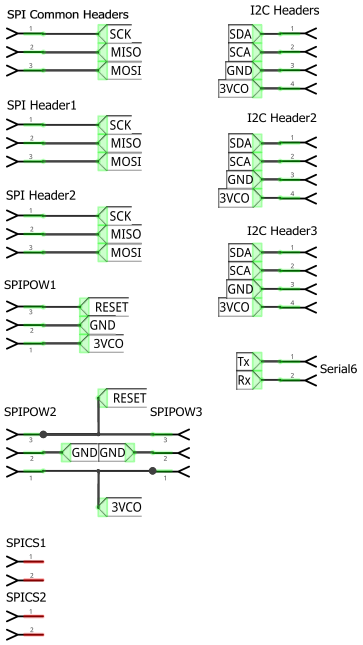

Distance Sensor Voltage Divider

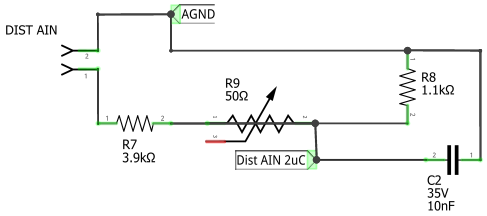

Force Sensor Voltage Divider

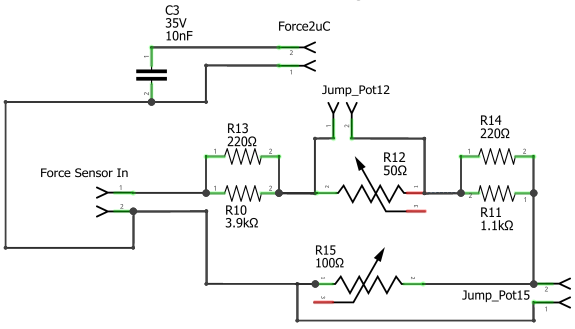

* All resistor values will change according to Voltage input

Nomenclature Reference

LESW - LED Switches
AIN - Analog Signal In
VCO - Controller Logic Voltage
2uC/uC Pin - Attached to microcontroller pin
AGND - Analog Ground

AFMPD Callibration Unit - Logic Board			
Project	AFMPD Tank8		
Filename	Controller Board.fzz	Rev	1
Date	22 May 2018 18:44:07	Sheet	1/1

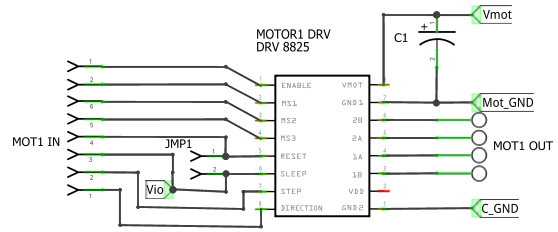

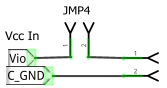

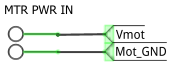

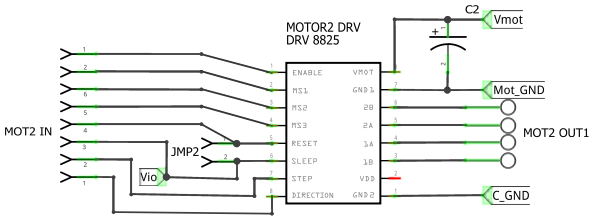

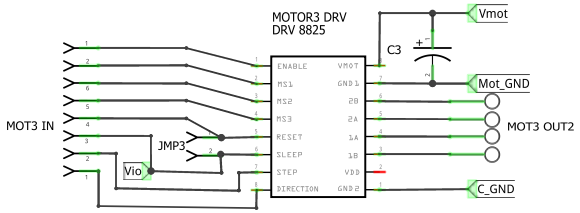

AFMPD Calibration Unit Motor Driver Board

Project	AFMPD Tank 8		
Filename	mot_driver.fzz	Rev	1
Date	24 Apr 2018 15:04:20	Sheet	1/1

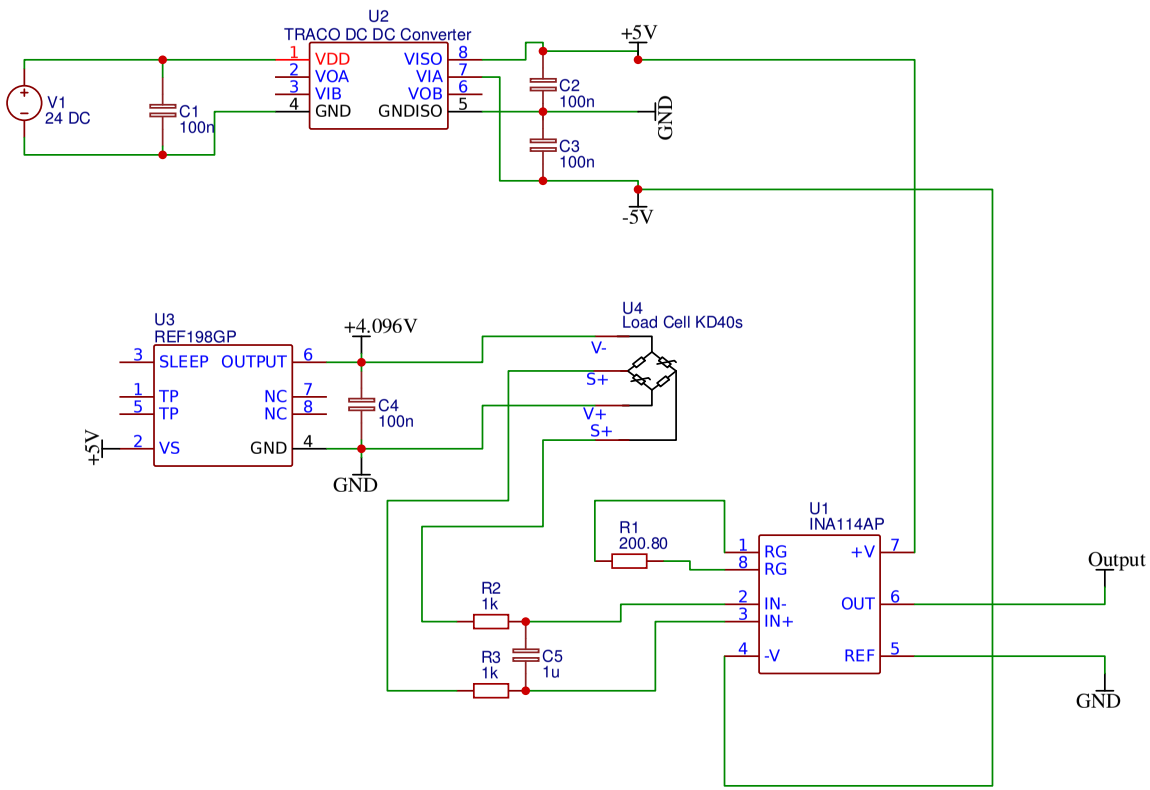

TITLE: Force Sensor Output Amplifier		REV: 1.0
Date: 2018-09-19	Sheet: 1/1	
Institute of Space Systems(IRS), Stuttgart	Drawn By: Akash Mankar	

Annex D

Programming Code

For ease of access, readability and archival, all the programs coded are hosted on the Github in individual repositories with permission from IRS and can be accessed via individual DOI links mentioned in each section.

D.1. Matlab Scripts for Interval Selection and Mean Export

The MATLAB script that is used for interval selection and mean export can be accessed via

DOI 10.5281/zenodo.1560701

Usage Instruction
Copy all the files into a folder and also copy the rawdata `tank8_xxx.dat` file into the same folder. Open the `Interval_Selection.m` and run the script, follow the prompts and you can select the intervals. After various intervals are selected, save the intervals, this will generate a MATLAB Struct file containing all the interval data. Then open the `Data_Export.m` and run the script and browse for the same rawdata file and the data will be extracted out and saved in an Excel file as well as a MATLAB Struct.

D.2. Vertical Calibration Teensy

DOI 10.5281/zenodo.1568400

Usage Instruction
Download the files and compile using Arduino IDE and upload to Teensy via Teensy loader. Make sure you have the support libraries (see D.4). Vertical force sensor mount (see 4.1.5) has to be implemented carefully avoiding slipping of the thread, care should also be taken to make sure that the homing sequence does not make the mount go all the way down and make contact with the force sensor translation unit.

Switch	Function
F5	Home calibration unit
F6	Calibrate

Table D.1: Current Switch Mapping for UX(Vertical Calibration)

D.3. Calibration and Measurement Program for Teensy

DOI 10.5281/zenodo.1570622

Download the files and compile using Arduino IDE and upload to Teensy via Teensy loader. Make sure you have the support libraries (see D.4).

Switch	Function
F1	Lock Thrust Balance
F2	Decouple Thrust Balance
F3	Calibrate
F4	Load Force Sensor
F5	Deload Force Sensor
F6	Cancel Preload/Deload

Table D.2: Current Switch Mapping for UX(Main Program)

D.4. Teensy Calibration Program Libraries Backup

All the libraries implemented in the main calibration program are open-source and they are constantly being updated, sometimes some function definitions or structure is changed which will make the main program obsolete, needing to recode again from scratch. This repository has all the libraries used in the main program, installing these libraries in the Arduino's library folder will ensure that the program keeps working.

DOI 10.5281/zenodo.1560705

Annex E

Mechanical Drawings

List of drawings

Sr.No.	Particular	Material
1	Round headed stylus for force sensor	Stainless Steel
2	Bearing spike for force sensor	Stainless Steel
3	Distance Sensor Calibration Unit	Aluminum
4	Distance Sensor Calibration - Base Plate	Aluminum
5	Distance Sensor Calibration - Counter screw mount	Aluminum
6	Distance Sensor Calibration - L Plate	Aluminum
7	Force Sensor Mount	Aluminum
8	Vertical Calibration Mount	Aluminum

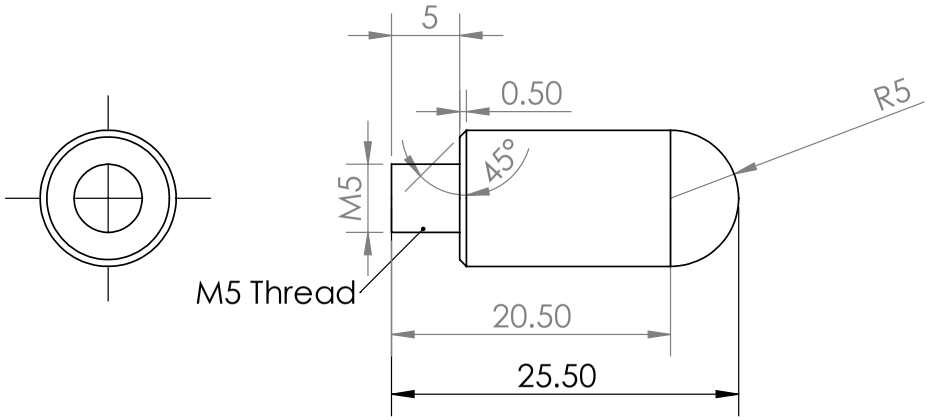

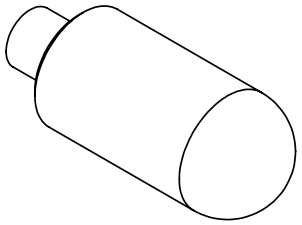

UNLESS OTHERWISE SPECIFIED: DIMENSIONS ARE IN MILLIMETERS SURFACE FINISH: TOLERANCES: LINEAR: ANGULAR:	FINISH:				DEBURR AND BREAK SHARP EDGES	DO NOT SCALE DRAWING / REVISION
	NAME	SIGNATURE	DATE			TITLE: Roundhead Spike for Force Sensor
DRAWN	Akash Mankar		24 Nov 2017			
CHK'D	Adam Boxberger			+49 (0) 711-685-62452		
APPV'D						
MFG						
Q.A			MATERIAL: Edelstahl / Hart Aluminium			DWG NO. roundendspike / A4
			WEIGHT:			SCALE:2:1 / SHEET 1 OF 1

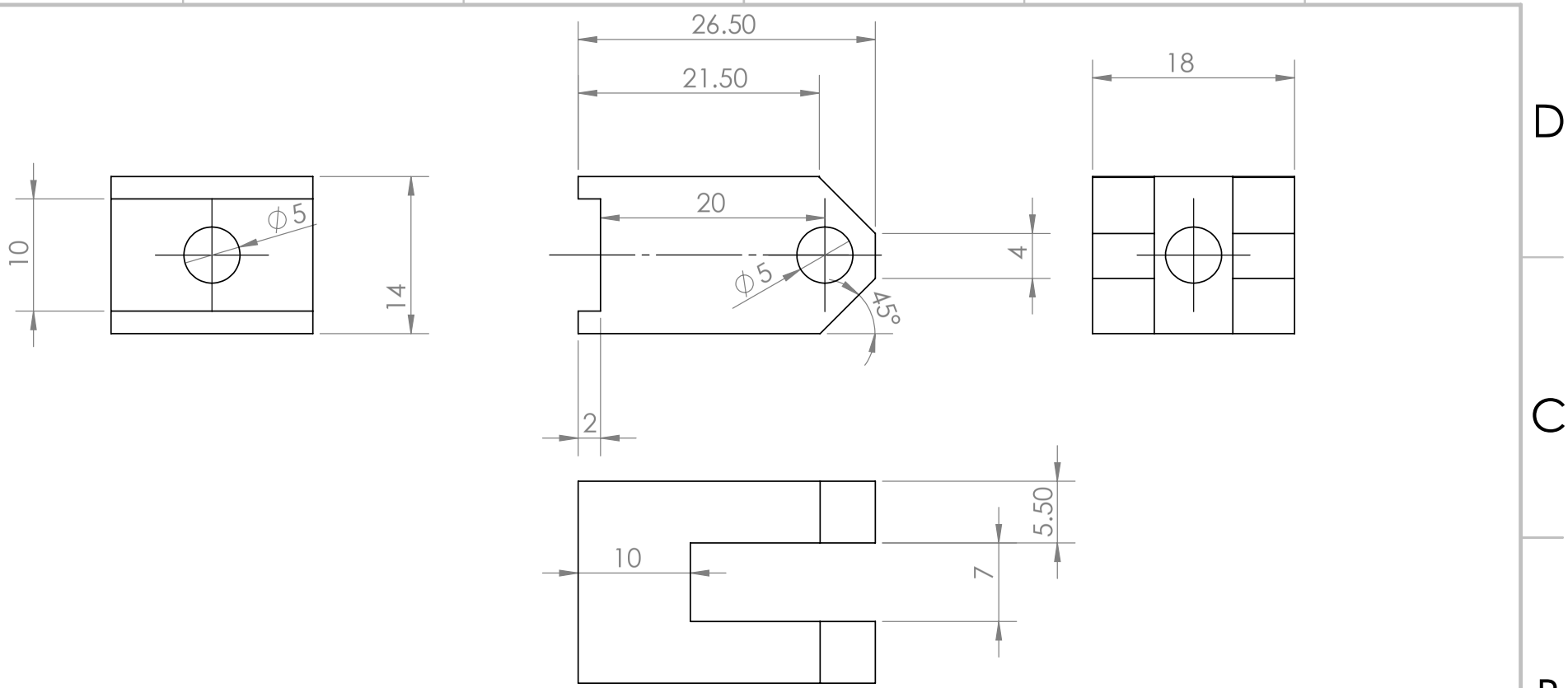

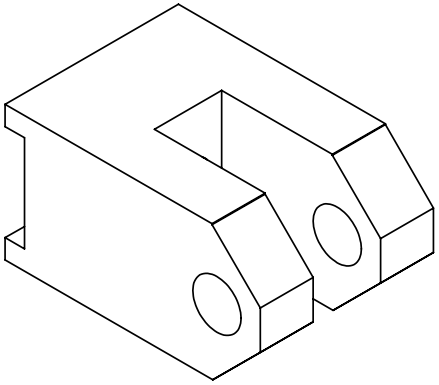

UNLESS OTHERWISE SPECIFIED: DIMENSIONS ARE IN MILLIMETERS SURFACE FINISH: TOLERANCES: LINEAR: ANGULAR:	FINISH:			DEBURR AND BREAK SHARP EDGES	DO NOT SCALE DRAWING	REVISION
	NAME	SIGNATURE	DATE		TITLE: Bearing type spike for force sensor	
DRAWN	Akash Mankar		24 Nov 2017			
CHK'D	Adam Boxberger			+49 (0) 711-685-62452		
APPV'D						
MFG						
Q.A				MATERIAL: Edelstahl / Hart Aluminium	DWG NO. bearingspike	A4
				WEIGHT:	SCALE:2:1	SHEET 1 OF 1

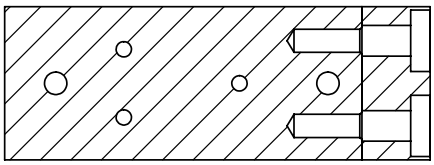

SECTION A-A

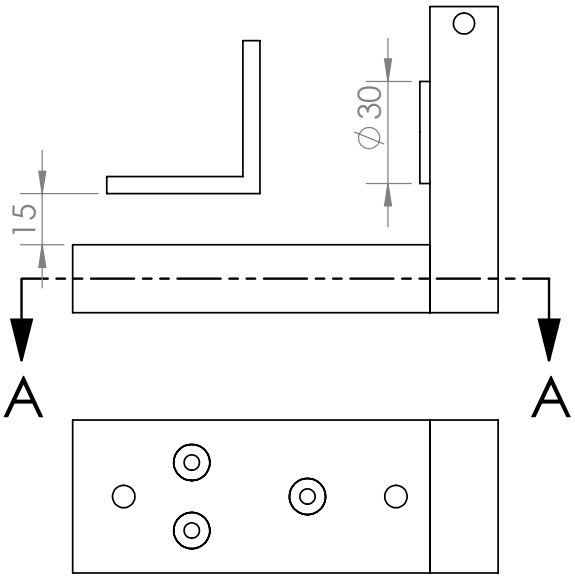

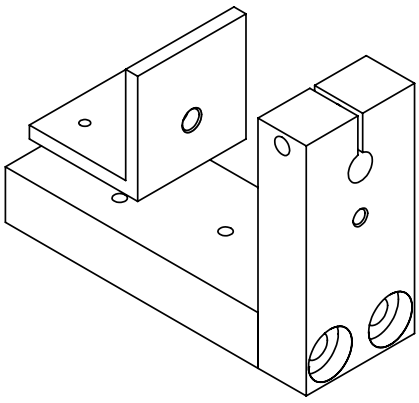

UNLESS OTHERWISE SPECIFIED: DIMENSIONS ARE IN MILLIMETERS SURFACE FINISH: TOLERANCES: LINEAR: ANGULAR:		FINISH:			DEBURR AND BREAK SHARP EDGES	DO NOT SCALE DRAWING	REVISION
	NAME	SIGNATURE	DATE			TITLE:	
DRAWN							
CHK'D							
APPV'D							
MFG							
Q.A				MATERIAL:		DWG NO. assembly	A4
				WEIGHT:		SCALE:1:2	SHEET 1 OF 1

SECTION H-H

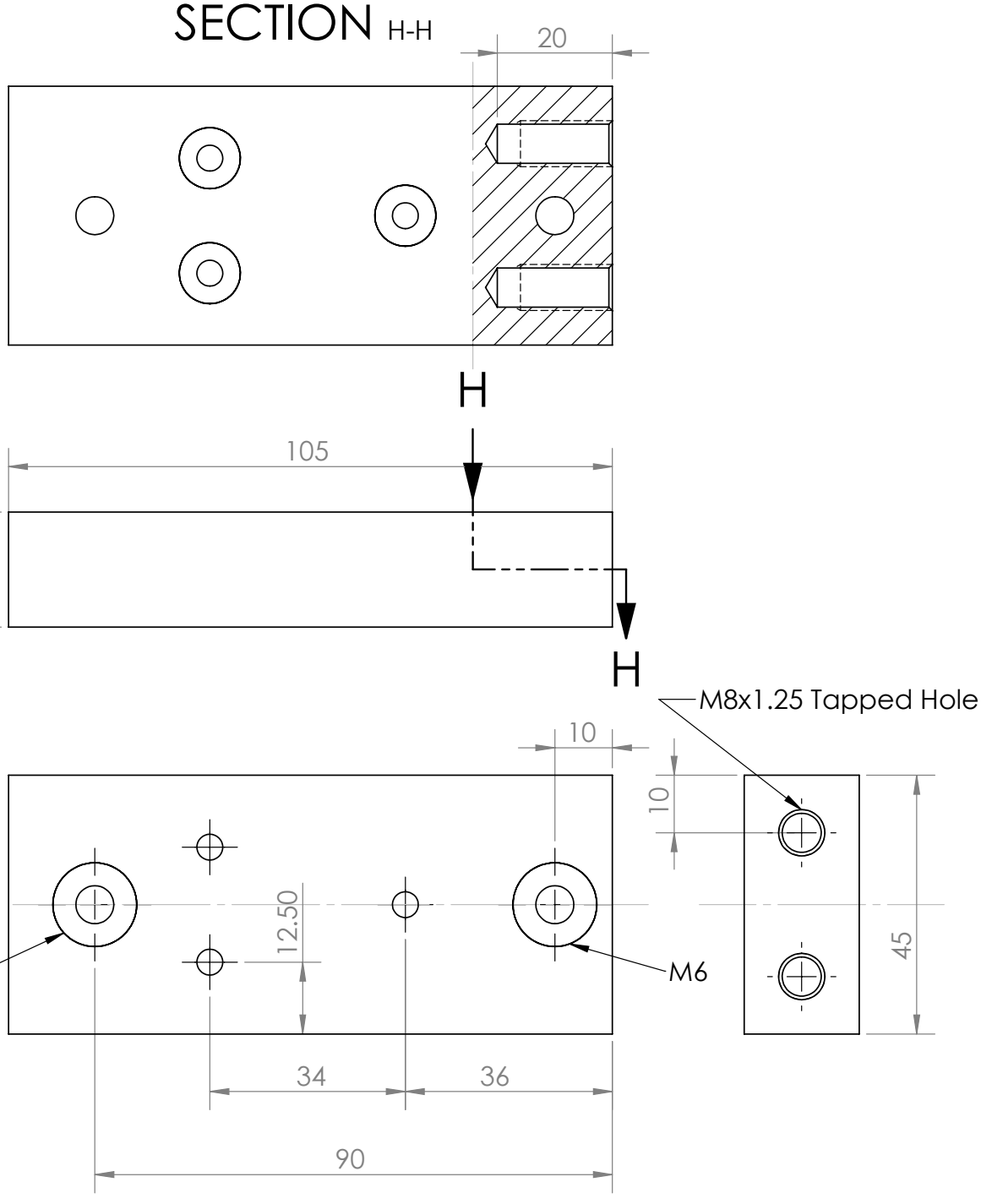

UNLESS OTHERWISE SPECIFIED: DIMENSIONS ARE IN MILLIMETERS SURFACE FINISH: TOLERANCES: LINEAR: ANGULAR:		FINISH:		DEBURR AND BREAK SHARP EDGES		DO NOT SCALE DRAWING	REVISION
	NAME	SIGNATURE	DATE			TITLE:	
DRAWN	Akash Mankar					Distance Sensor Calibration baseplate to mount microtranslation stage	
CHK'D							
APPV'D							
MFG							
Q.A				MATERIAL:		DWG NO. base_plate	A4
				WEIGHT:		SCALE:1:1	SHEET 1 OF 1

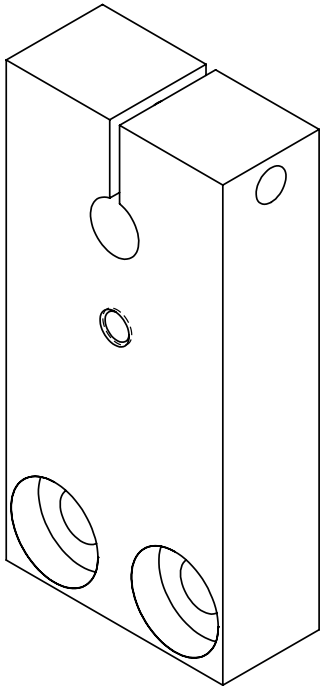

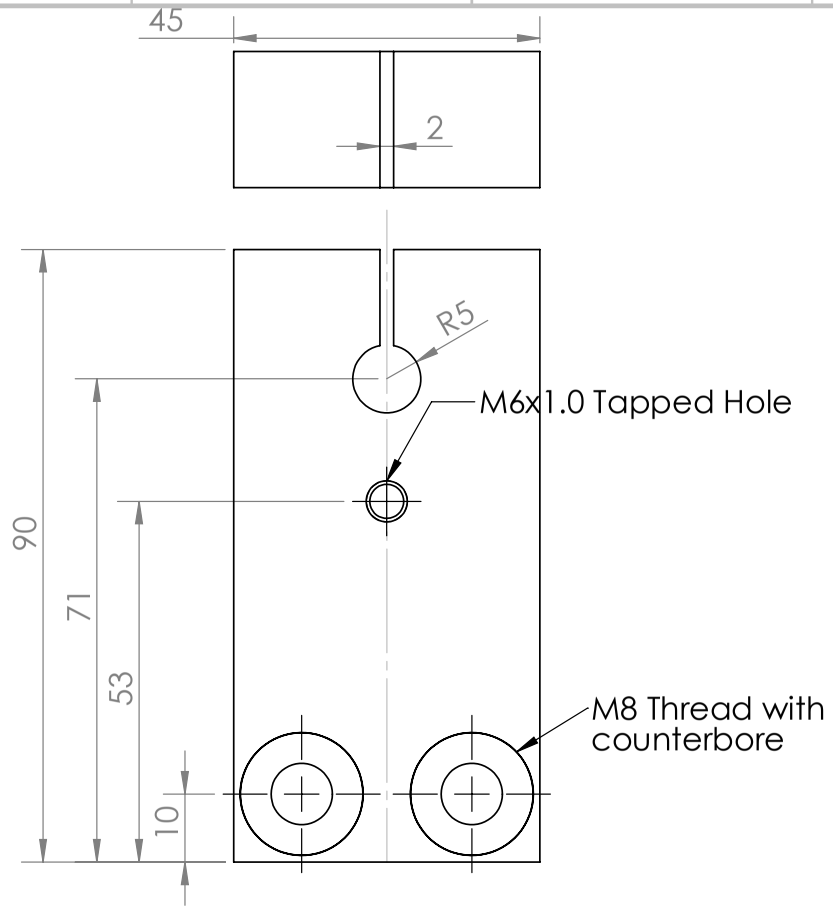

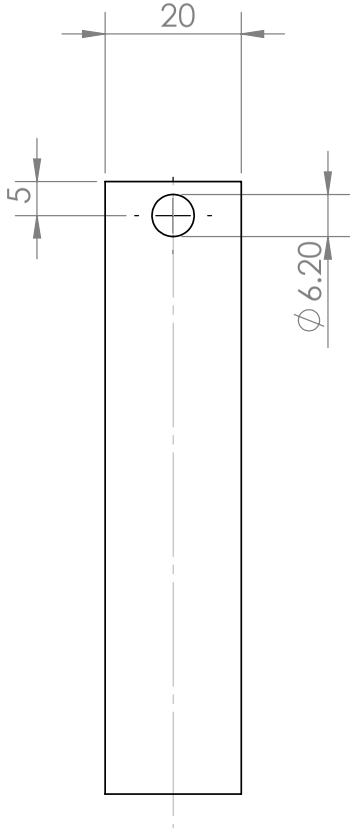

UNLESS OTHERWISE SPECIFIED: DIMENSIONS ARE IN MILLIMETERS SURFACE FINISH: TOLERANCES: LINEAR: ANGULAR:		FINISH:			DEBURR AND BREAK SHARP EDGES	DO NOT SCALE DRAWING	REVISION
	NAME	SIGNATURE	DATE			TITLE: Distance Sensor Calibration - Counter micrometer screw and aluminium plate mount	
DRAWN	Akash Mankar						
CHK'D							
APPV'D							
MFG							
Q.A				MATERIAL:		DWG NO. counter_screw_mount	A4
				WEIGHT:		SCALE:1:1	SHEET 1 OF 1

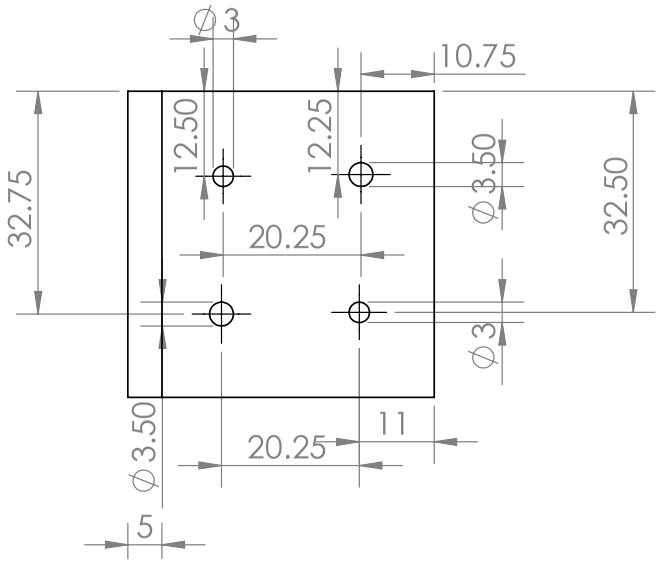

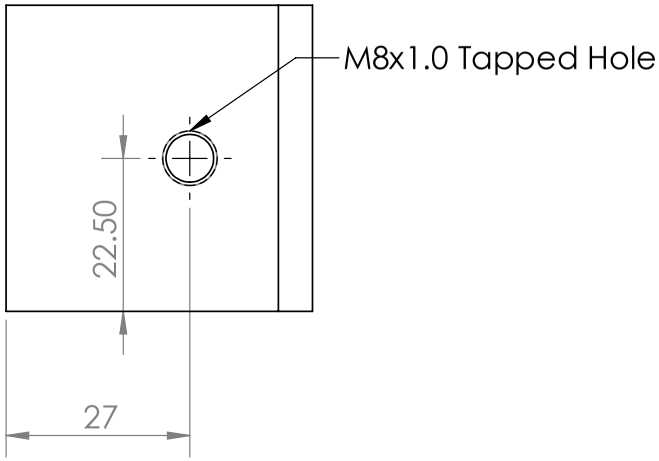

UNLESS OTHERWISE SPECIFIED: DIMENSIONS ARE IN MILLIMETERS SURFACE FINISH: TOLERANCES: LINEAR: ANGULAR:		FINISH:		DEBURR AND BREAK SHARP EDGES		DO NOT SCALE DRAWING	REVISION
	NAME	SIGNATURE	DATE			TITLE: Distance Calibration Unit - Distance Sensor mount for microtranslation stage	
DRAWN	Akash Manka						
CHK'D							
APP'V'D							
MFG							
Q.A				MATERIAL:		DWG NO. L_plate	A4
				WEIGHT:		SCALE:1:1	SHEET 1 OF 1

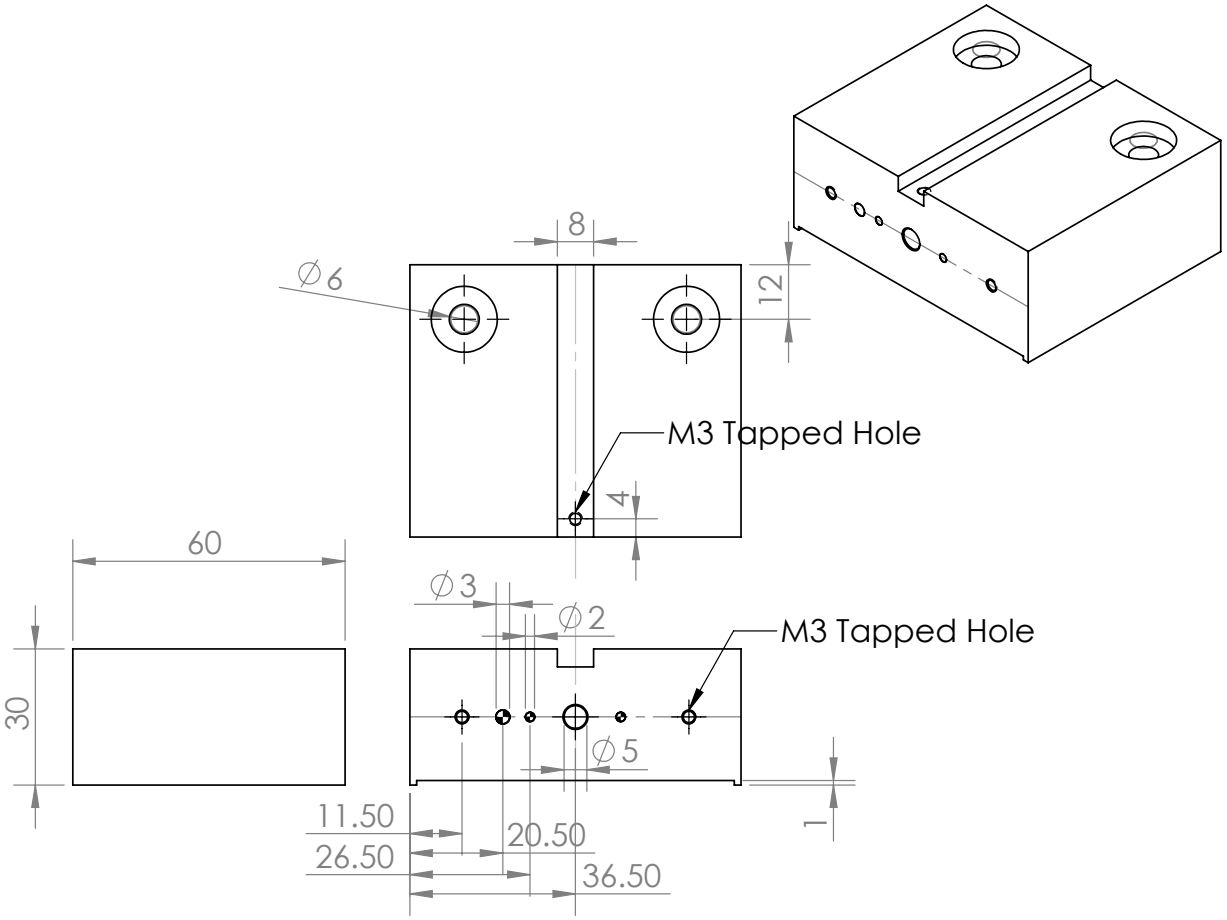

UNLESS OTHERWISE SPECIFIED: DIMENSIONS ARE IN MILLIMETERS SURFACE FINISH: TOLERANCES: LINEAR: ANGULAR:		FINISH:				DEBURR AND BREAK SHARP EDGES	DO NOT SCALE DRAWING	REVISION
							Institute of Space Sytem (IRS)	
	NAME	SIGNATURE	DATE				TITLE:	
DRAWN	Akash Mankar						Force Sensor Mount KD40s-5N for SX3 thrust measurement	
CHK'D								
APPV'D								
MFG								
Q.A				MATERIAL:			DWG NO.	A4
				Aluminum			mount	
				WEIGHT:			SCALE:1:2	SHEET 1 OF 1

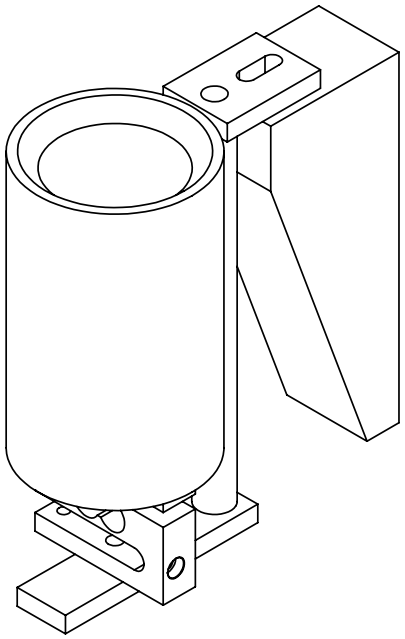

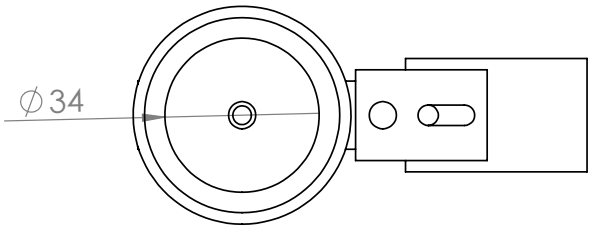

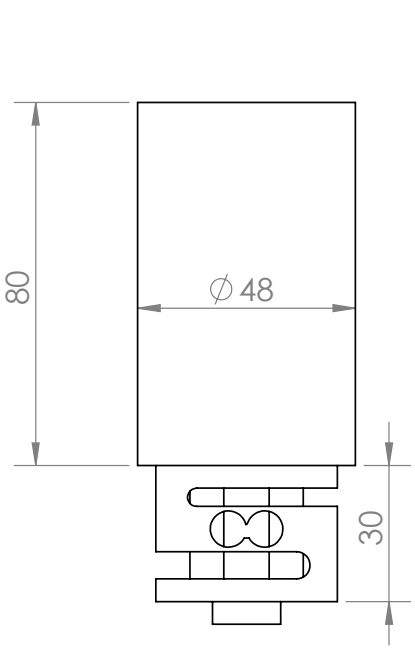

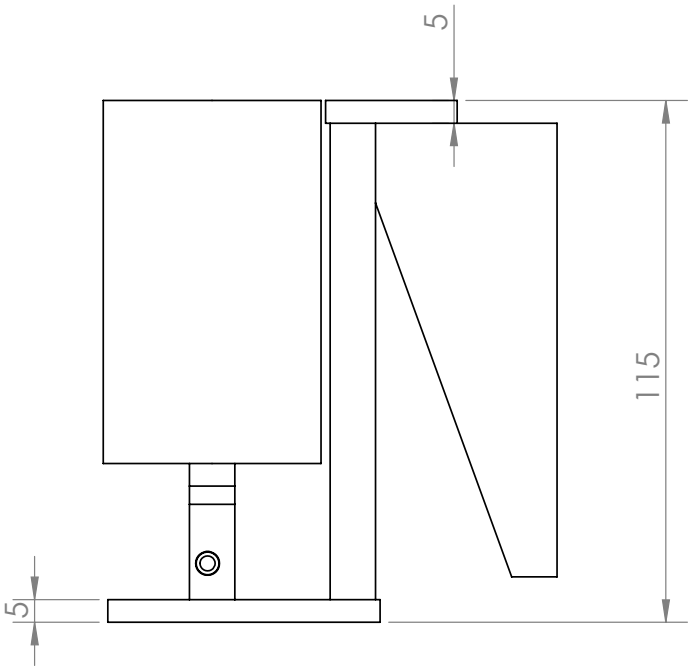

UNLESS OTHERWISE SPECIFIED: DIMENSIONS ARE IN MILLIMETERS SURFACE FINISH: TOLERANCES: LINEAR: ANGULAR:		FINISH:			DEBURR AND BREAK SHARP EDGES	DO NOT SCALE DRAWING	REVISION
						Institute of Space Spystem (IRS)	
	NAME	SIGNATURE	DATE			TITLE:	
DRAWN	Akash Mankar					Vertical Calibration Mount for SX3 calibration	
CHK'D							
APPV'D							
MFG							
Q.A				MATERIAL:		DWG NO.	A4
				PVC+Aluminum		vert_cal_assembly	
				WEIGHT:		SCALE:1:2	SHEET 1 OF 1

Annex F

Technical Datasheets

ME-Meßsysteme GmbH
Neuendorfstr. 18a
DE-16761 Hennigsdorf

Tel +49 (0)3302 8982 4 60
Fax +49 (0)3302 8982 4 69

Mail info@me-systeme.de
Web www.me-systeme.de

KD40s ±5N

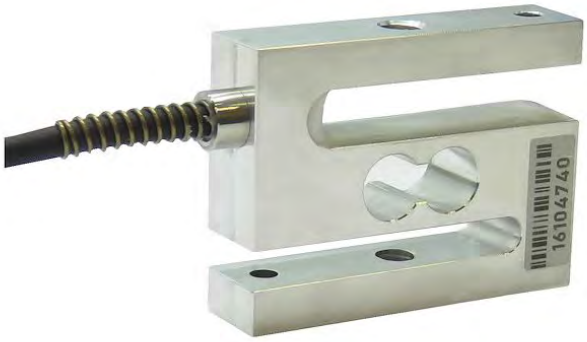

Description

The force sensor KD40S is very well suited for testing tasks in quality assurance as well as in materials testing due to its compact construction.
Inward and outward force transmission are arranged centrically.
The force sensors KD40S up to 100N are constructed as multi-range sensors. The accuracy of 0.1% is already reached at an rated output of 0.5 mV/V. This means that the zero-point stability is 4 times higher than in a sensor with the nominal output of 2 mV/V.
The force sensor KD40S can be used up to an output signal of 2 mV/V or four times the specified nominal force.
The force sensor KD40S (up to 100 N) should be installed in such way that the outgoing cables are assigned to the immobile side of the measuring construction. Thus forces from the connecting cable do not have an influence on measurement results.
From 500N upwards the force sensors KD40s have a nominal rated output of 1.0mV/V.
They can safely be overloaded up to 1.5x their nominal force.
The cable output can be found in the middle of the two force transmission beams.
For force transfer there exists one thread M5 (up to 100N) and M6 (from 500N) in the top and bottom side of the force sensor.
Additionally there is a thread M6 (from 500N) that can be used as anti-twist protection.
The force sensor from a nominal force of 1000N has a height of 34 mm.

ME-Meßsysteme GmbH
Neuendorfstr. 18a
DE-16761 Hennigsdorf

Tel +49 (0)3302 8982 4 60
Fax +49 (0)3302 8982 4 69

Mail info@me-systeme.de
Web www.me-systeme.de

Dimensions

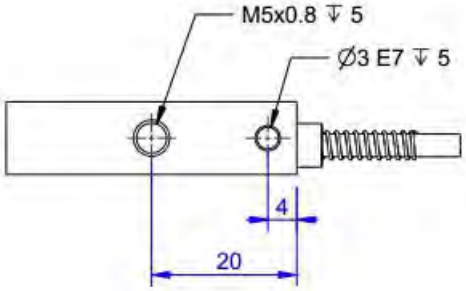

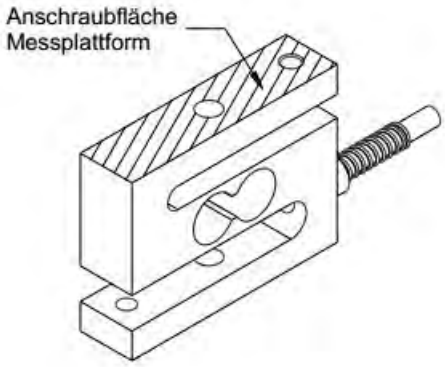

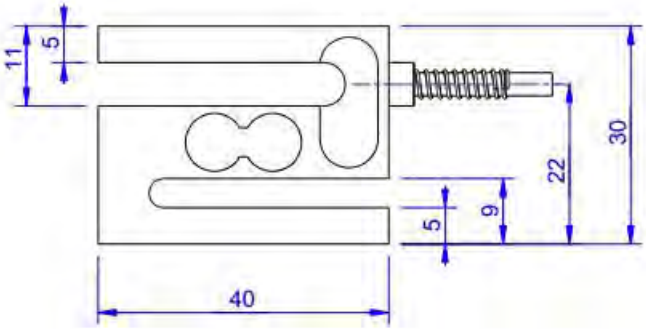

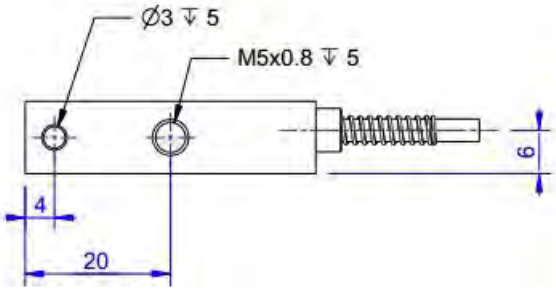

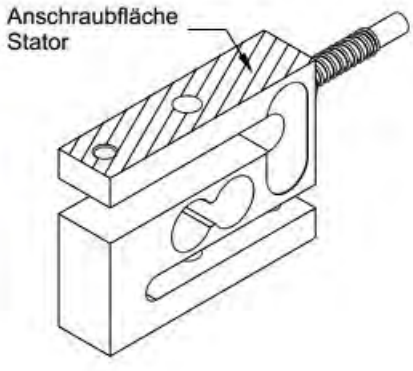

ME-Meßsysteme GmbH
Neuendorfstr. 18a
DE-16761 Hennigsdorf

Tel +49 (0)3302 8982 4 60
Fax +49 (0)3302 8982 4 69

Mail info@me-systeme.de
Web www.me-systeme.de

Technical Data

Electrical Data

Input resistance	390	Ohm
Tolerance input resistance	40	Ohm
Output resistance	350	Ohm
Tolerance output resistance	5	Ohm
Insulation resistance	2	GOhm
Rated range of excitation voltage f	2.5 ... 5	V
Operating range of excitation voltage f	1 ... 10	V
Zero signal	0.05	mV/V
Rated output	0.5	mV/V / FS
characteristic value range min	0.5	mV/V / FS
characteristic value range max	1	mV/V / FS

Precision

Accuracy class	0,1%	
Relative linearity error	0.02	%FS
Relative zero signal hysteresis	0.02	%FS
Temperature effect on zero signal	0.02	%FS/K
Temperature effect on characteristic value	0.01	%RD/K
Relative creep	0.1	%FS

Connection Data

Connection type	4 conductor open	
Name of the connection	ME-SYSTEME.DE / 24-4 PUR	
Cable length	3	m

Temperature

Rated temperature range f	-10 ... 70	°C
Operating temperature range f	-10 ... 85	°C
Storage temperature range f	-10 ... 85	°C
Environmental protection	IP65	

Force sensor

Type	Force sensor	
Force direction	Tension / Compression	
Rated force Fx	5	N
Force introduction	Inner thread	
Dimension 1	M5x0,8	
Sensor Fastening	Inner thread	
Dimension 2	M5x0,8	
Operating force	400	%FS
Rated displacement	0.2	mm
Lateral force limit	100	%FS
Material	Aluminium alloy	
Natural frequency	2	kHz

ME-Meßsysteme GmbH
Neuendorfstr. 18a
DE-16761 Hennigsdorf

Tel +49 (0)3302 8982 4 60
Fax +49 (0)3302 8982 4 69

Mail info@me-systeme.de
Web www.me-systeme.de

Pin Configuration

Symbol	Description	Wire colour
+Us	positive bridge supply	brown
-Us	negative bridge supply	white
+Ud	positive bridge output	green
-Ud	negative bridge output	yellow

Screen - transparent.

Pressure load : positive output signal

Prüfprotokoll

Typ	KD40s 5N
Nennlast (FS)	5N
Seriennummer	18207484
Nullsignal	0.000812 mV/V
Kennwert	0.4914 mV/V
Sensor-Widerstand	452.25 Ohm
Prüfdatum:	20.09.2018

Isolationsprüfung

Prüfung	Prüfergebnis
Schirm / Anschlussleitung	i.O.
Verformungskörper / Anschlussleitung	i.O.
Schirm / Verformungskörper	i.O.

braun/weiß/grün/gelb freies Kabelende

Symbol	Beschreibung	Farbe	PIN
+Us	positive Brückenspeisung	braun	
-Us	negative Brückenspeisung	weiß	
+Ud	positiver Brückenausgang	grün	
-Ud	negativer Brückenausgang	gelb	

Schirm / shield: transparent

Diana Zeretzke, 20.09.2018

ME-Meßsysteme GmbH
Neuendorfstr. 18a
16761 Hennigsdorf

Tel.: +49 (0)3302 78620 60
Fax.: +49 (0)3302 78620 69

Mail: info@me-systeme.de
Web: www.me-systeme.de

Datasheet F-201CV

Mass Flow Controller for Gases

EL-FLOW *Select* Mass Flow Controller model F-201CV

> Introduction

Bronkhorst High-Tech model F-201CV Mass Flow Controllers (MFCs) are suited for precise control of virtually all conventional process gases. The MFC consists of a thermal mass flow sensor, a precise control valve and a microprocessor based PID controller with signal and fieldbus conversion. As a function of a setpoint value, the flow controller swiftly adjusts the desired flow rate. The mass flow, expressed in normal litres or millilitres per minute or per hour, is provided as analog signal or digitally via RS232 or fieldbus. The flow range, wetted materials and orifice size for the control valve are determined depending of the type of gas and the process conditions of the application.

Although all specifications in this datasheet are believed to be accurate, the right is reserved to make changes without notice or obligation.

> Technical specifications

Measurement / control system

Accuracy (incl. linearity) (Based on actual calibration)	: ± 0,5% Rd plus ± 0,1% FS
Turndown	: 1 : 50 (in digital mode up to 1:187,5)
Multiple fluid capability	: • storage of max. 8 calibration curves • optional Multi Gas / Multi Range functionality up to 10 bar
Repeatability	: < ± 0,2% Rd
Settling time (controller)	: 1…2 seconds; option: down to 500 msec
Control stability	: ≤ ± 0,1% FS (typical for 1 l_n/min N_2)
Max. Kv-value	: 6,6 x 10^{-2}
Temperature range	: -10…+70°C
Temperature sensitivity (nominal range)	: zero: < ± 0,05% FS/°C; span: < ± 0,05% Rd/°C
Leak integrity (outboard)	: < 2 x 10^{-9} mbar l/s He
Attitude sensitivity	: max. error at 90° off horizontal 0,2% FS at 1 bar, typical N_2
Warm-up time	: 30 min. for optimum accuracy 2 min. for accuracy ± 2% FS

Mechanical parts

Material (wetted parts)	: stainless steel 316L or comparable
Pressure rating	: 64 bar abs
Process connections	: compression type or face seal male
Seals	: standard : Viton; options: EPDM, Kalrez
Ingress protection (housing)	: IP40

Electrical properties

Power supply	: +15…24 Vdc ±10%		
Power consumption	: Supply	at voltage I/O	at current I/O
(based on N/C valve)	15 V	290 mA	320 mA
	24 V	200 mA	215 mA
Extra for fieldbus: (if applicable)	PROFIBUS DP: add 53 mA (15 V supply) or 30 mA (24 V supply) EtherCAT®: add 66 mA (15 V supply) or 41 mA (24 V supply) DeviceNet™: add 48 mA (24 V supply)		
Analog output	: 0…5 (10) Vdc, min. load impedance > 2 kΩ; 0 (4)…20 mA (sourcing), max. load impedance < 375 Ω		
Analog setpoint	: 0…5 (10) Vdc, min. load impedance > 100 kΩ; 0 (4)…20 mA, load impedance ~250 Ω		
Digital communication	: standard RS232; options: PROFIBUS DP, DeviceNet™, EtherCAT®, Modbus RTU/ASCII, FLOW-BUS		

> Ranges (based on Air)

Model	minimum	nominal	maximum
F-201CV-020	0,16…8 ml_n/min	0,16…20 ml_n/min	0,16…30 ml_n/min
F-201CV-050	0,4…20 ml_n/min	0,4…50 ml_n/min	0,4…75 ml_n/min
F-201CV-100	0,8…40 ml_n/min	0,8…100 ml_n/min	0,8…150 ml_n/min
F-201CV-200	1,6…80 ml_n/min	1,6…200 ml_n/min	1,6…300 ml_n/min
F-201CV-500	4…200 ml_n/min	4…500 ml_n/min	4…750 ml_n/min
F-201CV-1K0	8…400 ml_n/min	8…1000 ml_n/min	8…1500 ml_n/min
F-201CV-2K0	16…800 ml_n/min	16…2000 ml_n/min	16…3000 ml_n/min
F-201CV-5K0	0,04…2 l_n/min	0,04…5 l_n/min	0,04…7,5 l_n/min
F-201CV-10K	0,08…4 l_n/min	0,08…10 l_n/min	0,08…15 l_n/min
F-201CV-20K	0,16…8 l_n/min	0,16…20 l_n/min	0,16…25 l_n/min

Intermediate ranges are available

Bronkhorst®
HIGH-TECH

Datascan Analog Measurement Processors 7320 & 7321

General Description

The Datascan 7300 series is a series of intelligent distributed input/output modules designed for real time measurement, data collection and communication. Ideal for factory industrial and scientific applications, the Datascan 7300 combines the cost saving benefit of distributed I/O with the flexibility of local channel expansion.

Main Features

- Direct Sensor connection for DC voltages, thermocouples strain gauges RTD's resistance and 4-20mA converters
- 16 inputs on board expandable locally to 256 channels (1000 over network)
- Integral network interface for distribution over 1.2 Km (4Km with extension unit)
- I6 bit measurement performance with 0.625µV sensitivity
- Serial Port isolated to 500 VDC
- Wide range of compatible analog and digital input/ output modules for expansion
- Local measurement speed up to 400 readings/sec 1000/sec over the network
- Individual channel programming of sensor type and speed
- Multi Vendor Software Support
- Compact Rugged DIN rail mounted
- Network Port isolated to 500 VDC

The **7300** series is designed to provide a simple, reliable, accurate and cost effective means of connecting plant sensors to standard computers for real time monitoring and data acquisition. The Datascan can be used universally with any type of computer as the data interface is by means of a standard serial port.

The **7300** series is the most recent addition to the range of measurement processors and is completely compatible with the previous series of products. The 7300 series can be used with any of the 26 Datascan channel expansion modules in the range.

The **7300** series can be used autonomously or alternatively as part of a total distributed network. Each 7300 can support up to 256 channels of local inputs or outputs using the units local expansion bus. Alternatively it can become part of a distributed network of up to 1000 channels spanning a distance of up to 4 Km (15000 ft). Each 7300 incorporates a programmable 16 bit ADC, an isolated serial interface, an isolated token passing network interface, on board non volatile memory for storing unit configurations, 8 or 16 inputs depending on model type, and an expansion port for channel extension. The unit is packaged in a compact DIN rail mounted carrier making it simple to install.

Specification

Model Type	No of Inputs	Sensor Types	Resolution	Input Impedance
7320	**16** (3 pole) expandable to 256 channels	DC Voltage, Thermocouples, 4-20 mA	16 bits @ 40 rdgs/sec 14 bits @ 400 rdgs/sec	30M ohms
7321	**8** (6 pole) with pulsed energisation expandable to 256 channels	DC Voltage, Thermocouples, Resistance Thermometers, Strain Gauges, 4-20 mA, Resistance	16 bits @ 40 rdgs/sec 14 bits @ 400 rdgs/sec	30M ohms

The 7320/21 are analog input measurement processors. The 7320 is a 16 channel unit whereas the 7321 provides a total of 8 channels.

Both units provide direct sensor connection for Thermocouples, DC voltages, 4-20 mA inputs and current.

The 7321 provides direct sensor energisation for strain gauges and resistance thermometers. Both models have integral CJC for direct Thermocouple measurement.

Sensor	Range	16 bit	14 bit	Accuracy
DC voltage (7320/21)	10 V 1.3V 150mV 20mV Auto	320 µV 40 µV 5 µV 0.625µV	1.28 mV 160 µV 20 µV 2.5 µV	+/-0.02%rdg+0.01%range+1bit +/-0.02%rdg+0.01%range+1bit +/-0.02%rdg+0.01%range+1bit 16bit(+/-0.02%rdg+0.01%range+5µV) 14bit(+/-0.02%rdg+0.01%range+10µV)

Calibration period 12 months. Calibration termperature 20°C.All quoted errors are worst case.

Temperature coeff <30 ppm / °C (CJC Error 0.6 °C)

Each channel can be individually programmed for specific sensors speed and measurement range.

The high performance 16 bit ADC (Analog to digital converters) offers sensitivities as high as 0.625 µV.

The integrating technique of conversion provides very high immunity to mains borne noise.

Software support

Datascan can be used with a wide range of standard software products available from several third party vendors.

Other details

Common/series mode rejection

DC common mode : 100 dB's
AC common mode : 120 dB's
AC series mode : 60 dB's

Overload Protection

+/- 30V continuous

+/- 200V transient <0.1s

RS232 Port

Baud Rates : 4800, 9600, 19.2K, 38.4K
Isolation : 500V DC

Network Specifications

Electrical Specification : RS485
Media : Twisted Pair
Maximum Length : 1.2Km
Data Rate : 1000 results / sec
Isolation : 500V DC
Total channels / network : 1000

Sensor Type Thermocouple 7320/21	Ranges	Sensitivity 16 bit resolution	Sensitivity 14 bit resolution	Limits of Error
K Type	-100 to 500 °C 500 to 1200 °C	0.02 °C 0.20 °C	0.1 °C 1.0 °C	0.3 °C 0.6 °C
J Type	-50 to 360 °C 360 to 800 °C	0.02 °C 0.20 °C	0.1 °C 1.0 °C	0.3 °C 0.5 °C
N Type	-200 to 100 °C 100 to 580 °C 580 to 1300 °C	0.10 °C 0.05 °C 0.10 °C	0.4 °C 0.2 °C 0.4 °C	0.6 °C 0.4 °C 0.6 °C
T Type	-150 to 400 °C	0.02 °C	0.1 °C	0.3 °C
R Type	0 to 1600 °C	0.10 °C	0.4 °C	1.4 °C
S Type	0 to 1700 °C	0.10 °C	0.4 °C	1.4 °C
E Type	-50 to 290 °C 290 to 1000 °C	0.02 °C 0.10 °C	0.1 °C 0.4 °C	0.3 °C 0.7 °C
B Type	200 to 1600 °C	0.50 °C	2.0 °C	4.4 °C
Resistance thermometers PT100 (7321 only)	-50 to 300 °C -150 to 500 °C	0.02 °C 0.20 °C	0.1 °C 1.0 °C	0.25 °C 0.50 °C
Strain Gauges Full 1/2 1/4 bridge (7321 only)	0-10,000 µe	0.62 µe	3.0 µe	10 µe
4-20 mA (7320/21)	4-20 mA			+/-0.15%

Power	Dimensions	Weight	Op temp	Humidity
Supply 24V DC consumption <2 Watts @ 24V	W 230 mm H 123 mm D 80 mm	750 grams	-10 to 60°C storage -20 to 80°C	RH 90% Non-Condensing

Your Local Distributor

Measurement Systems Ltd
16 Kingfisher Court
Newbury
Berkshire
RG14 5SJ UK
Tele: +44 (0)1635 576800
Fax : +44 (0)1635 31023

Issue 2.2 5/96

Welcome to Teensy® 3.6

32 Bit Arduino-Compatible Microcontroller

To begin using Teensy, please visit the website & click Getting Started.

www.pjrc.com/teensy

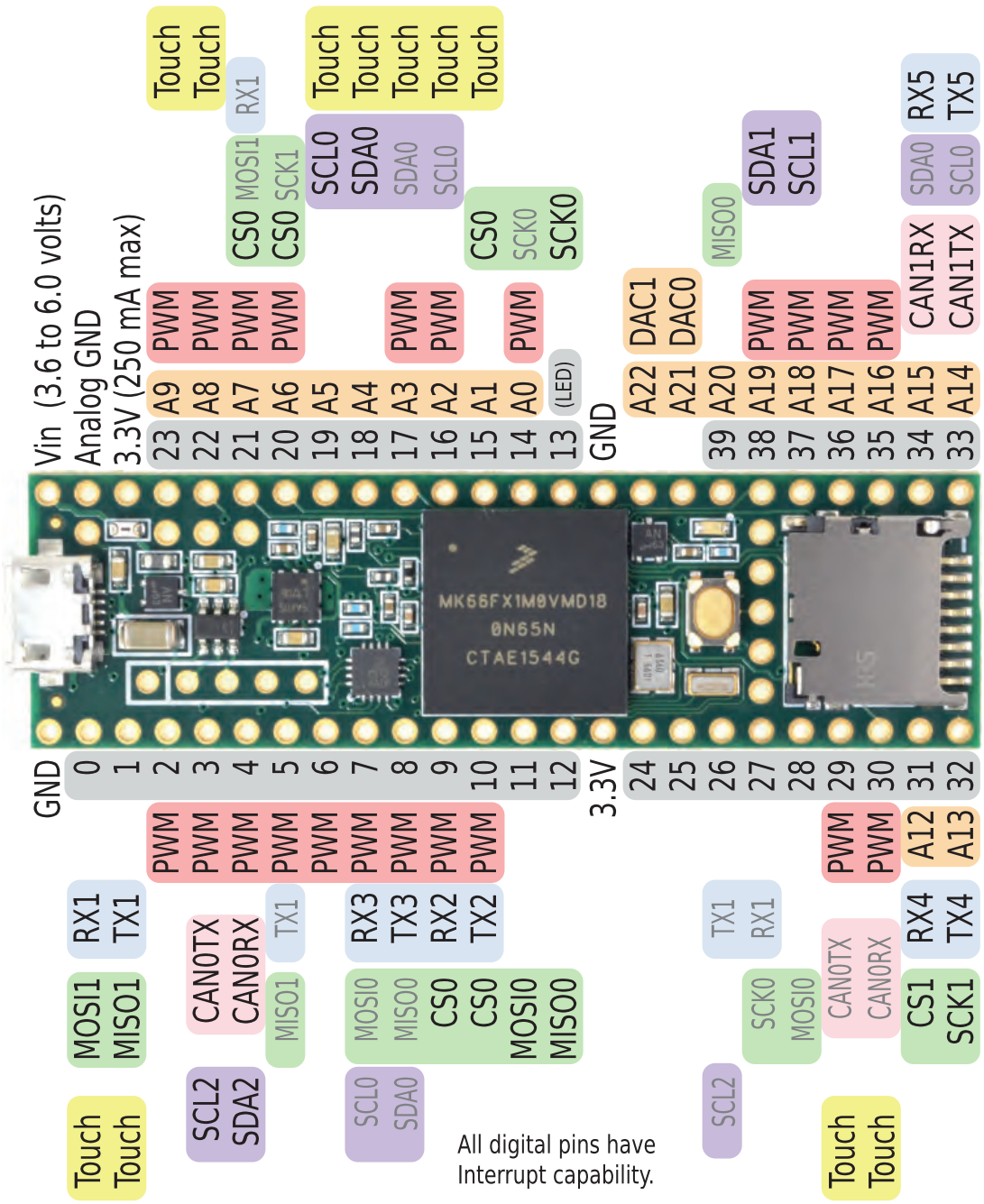

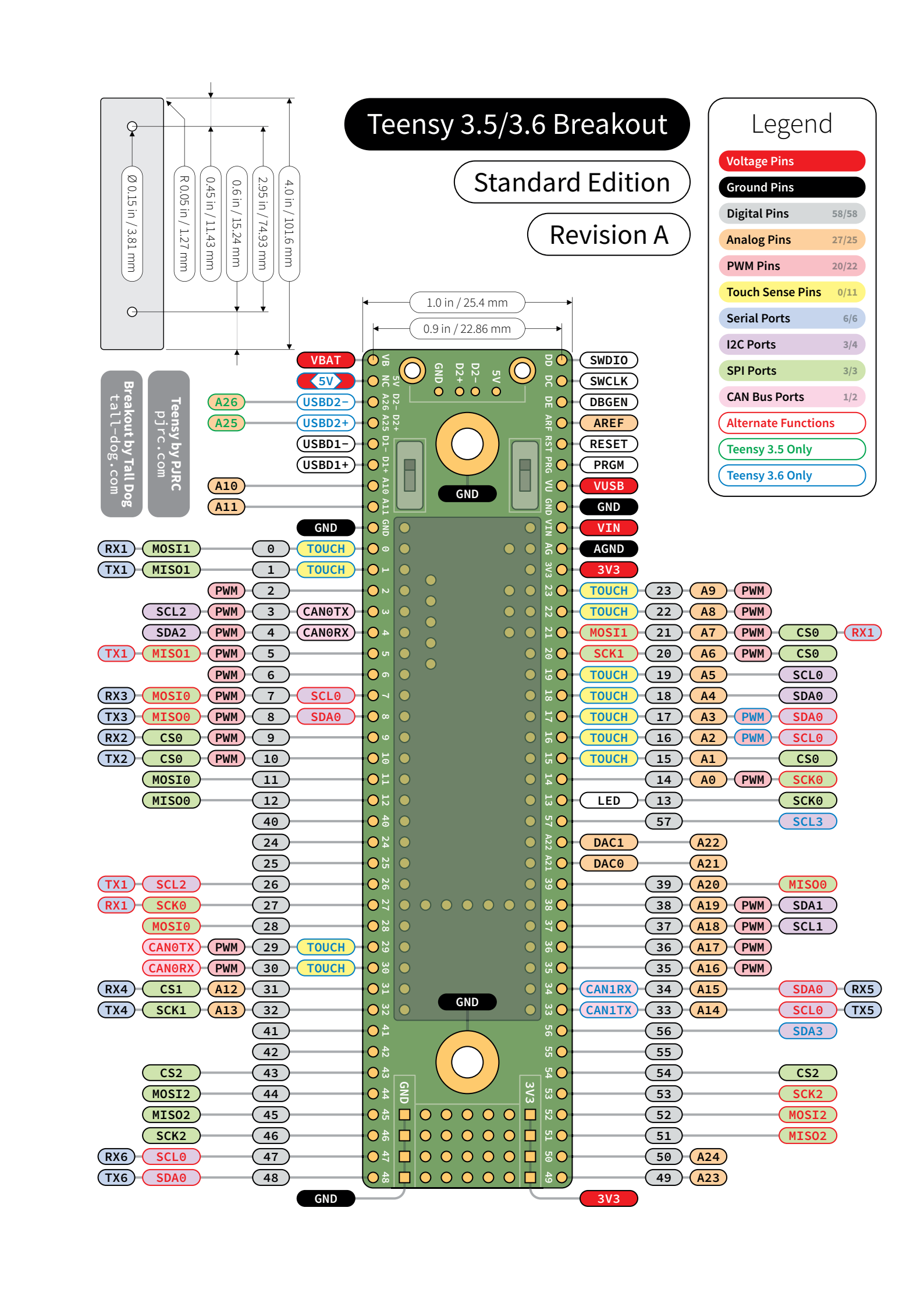
Teensy 3.5/3.6 Breakout
Standard Edition
Revision A
Legend
Voltage Pins
Ground Pins
Digital Pins 58/58
Analog Pins 27/25
PWM Pins 20/22
Touch Sense Pins 0/11
Serial Ports 6/6
I2C Ports 3/4
SPI Ports 3/3
CAN Bus Ports 1/2
Alternate Functions
Teensy 3.5 Only
Teensy 3.6 Only
Ø 0.15 in / 3.81 mm
R 0.05 in / 1.27 mm
0.45 in / 11.43 mm
0.6 in / 15.24 mm
2.95 in / 74.93 mm
4.0 in / 101.6 mm
1.0 in / 25.4 mm
0.9 in / 22.86 mm
Breakout by Tall Dog
tall-dog.com
Teensy by PJRC
pjrc.com
VBAT
5V
A26 USBD2−
A25 USBD2+
USBD1−
USBD1+
A10
A11
GND
VUSB
GND
VIN
AGND
3V3
SWDIO
SWCLK
DBGEN
AREF
RESET
PRGM
GND
GND
RX1 MOSI1 0 TOUCH
TX1 MISO1 1 TOUCH
PWM 2
SCL2 PWM 3 CAN0TX
SDA2 PWM 4 CAN0RX
TX1 MISO1 PWM 5
PWM 6
RX3 MOSI0 PWM 7 SCL0
TX3 MISO0 PWM 8 SDA0
RX2 CS0 PWM 9
TX2 CS0 PWM 10
MOSI0 11
MISO0 12
40
24
25
TX1 SCL2 26
RX1 SCK0 27
MOSI0 28
CAN0TX PWM 29 TOUCH
CAN0RX PWM 30 TOUCH
RX4 CS1 A12 31
TX4 SCK1 A13 32
41
42
CS2 43
MOSI2 44
MISO2 45
SCK2 46
RX6 SCL0 47
TX6 SDA0 48
GND
TOUCH 23 A9 PWM
TOUCH 22 A8 PWM
MOSI1 21 A7 PWM CS0 RX1
SCK1 20 A6 PWM CS0
TOUCH 19 A5 SCL0
TOUCH 18 A4 SDA0
TOUCH 17 A3 PWM SDA0
TOUCH 16 A2 PWM SCL0
TOUCH 15 A1 CS0
14 A0 PWM SCK0
LED 13 SCK0
57 SCL3
DAC1 A22
DAC0 A21
39 A20 MISO0
38 A19 PWM SDA1
37 A18 PWM SCL1
36 A17 PWM
35 A16 PWM
CAN1RX 34 A15 SDA0 RX5
CAN1TX 33 A14 SCL0 TX5
56 SDA3
55
54 CS2
53 SCK2
52 MOSI2
51 MISO2
50 A24
49 A23
3V3

MEAN WELL

200W Single Output Switching Power Supply

LRS-200 series

(Note.9)

Features

- AC input range selectable by switch
- Withstand 300VAC surge input for 5 second
- Protections: Short circuit / Overload / Over voltage / Over temperature
- Cooling by free air convection
- 1U low profile
- Withstand 5G vibration test
- LED indicator for power on
- No load power consumption<0.75W
- 100% full load burn-in test
- High operating temperature up to 70℃
- Operating altitude up to 5000 meters (Note.8)
- High efficiency, long life and high reliability
- 3 years warranty

Applications

- Industrial automation machinery
- Industrial control system
- Mechanical and electrical equipment
- Electronic instruments, equipments or apparatus

Description

LRS-200 series is a 200W single-output enclosed type power supply with 30mm of low profile design. Adopting the input of 115VAC or 230VAC (select by switch), the entire series provides an output voltage line of 3.3V, 4.2V, 5V, 12V, 15V, 24V, 36V and 48V.

In addition to the high efficiency up to 90%, the design of metallic mesh case enhances the heat dissipation of LRS-200 that the whole series operates from -25℃ through 70℃ under air convection without a fan. Delivering an extremely low no load power consumption (less than 0.75W), it allows the end system to easily meet the worldwide energy requirement. LRS-200 has the complete protection functions and 5G anti-vibration capability; it is complied with the international safety regulations such as UL 60950-1.

LRS-200 series serves as a high price-to-performance power supply solution for various industrial applications.

Model Encoding

LRS - 200 - 3.3

- 3.3 — Output voltage
- 200 — Output power
- LRS — Series name

MEAN WELL

200W Single Output Switching Power Supply LRS-200 series

SPECIFICATION

MODEL		LRS-200-3.3	LRS-200-4.2	LRS-200-5	LRS-200-12	LRS-200-15	LRS-200-24	LRS-200-36	LRS-200-48
OUTPUT	DC VOLTAGE	3.3V	4.2V	5V	12V	15V	24V	36V	48V
	RATED CURRENT	40A	40A	40A	17A	14A	8.8A	5.9A	4.4A
	CURRENT RANGE	0 ~ 40A	0 ~ 40A	0 ~ 40A	0 ~ 17A	0 ~ 14A	0 ~ 8.8A	0 ~ 5.9A	0 ~ 4.4A
	RATED POWER	132W	168W	200W	204W	210W	211.2W	212.4W	211.2W
	RIPPLE & NOISE (max.) Note.2	150mVp-p	150mVp-p	150mVp-p	150mVp-p	150mVp-p	150mVp-p	200mVp-p	200mVp-p
	VOLTAGE ADJ. RANGE	2.97 ~ 3.6V	3.6 ~ 4.4V	4.5 ~ 5.5V	10.2 ~ 13.8V	13.5 ~ 18V	21.6 ~ 28.8V	32.4 ~ 39.6V	43.2 ~ 52.8V
	VOLTAGE TOLERANCE Note.3	±3.0%	±4.0%	±3.0%	±1.5%	±1.0%	±1.0%	±1.0%	±1.0%
	LINE REGULATION Note.4	±0.5%	±0.5%	±0.5%	±0.5%	±0.5%	±0.5%	±0.5%	±0.5%
	LOAD REGULATION Note.5	±2.5%	±2.5%	±2.0%	±1.0%	±0.5%	±0.5%	±0.5%	±0.5%
	SETUP, RISE TIME	1300ms, 50ms/230VAC 1300ms,50ms/115VAC at full load							
	HOLD UP TIME (Typ.)	16ms/230VAC 12ms/115VAC at full load							
INPUT	VOLTAGE RANGE	90 ~ 132VAC / 180 ~ 264VAC by switch 240 ~ 370VDC (switch on 230VAC)							
	FREQUENCY RANGE	47 ~ 63Hz							
	EFFICIENCY (Typ.)	83%	86%	87%	87.5%	88%	89.5%	89.5%	90%
	AC CURRENT (Typ.)	4A/115VAC 2.2A/230VAC							
	INRUSH CURRENT (Typ.)	COLD STAR 60A/115VAC 60A/230VAC							
	LEAKAGE CURRENT	<2mA / 240VAC							
PROTECTION	OVER LOAD	110 ~ 140% rated output power							
		Protection type : Hiccup mode, recovers automatically after fault condition is removed							
	OVER VOLTAGE	3.8 ~ 4.45V	4.6 ~ 5.4V	5.75 ~ 6.75V	13.8 ~ 16.2V	18 ~ 21V	28.8 ~ 33.6V	41.4 ~ 46.8V	55.2 ~ 64.8V
		Protection type : Hiccup mode, recovers automatically after fault condition is removed							
	OVER TEMPERATURE	Hiccup mode, recovers automatically after fault condition is removed							
ENVIRONMENT	WORKING TEMP.	-25 ~ +70℃ (Refer to "Derating Curve")							
	WORKING HUMIDITY	20 ~ 90% RH non-condensing							
	STORAGE TEMP., HUMIDITY	-40 ~ +85℃, 10 ~ 95% RH							
	TEMP. COEFFICIENT	±0.03%/℃ (0 ~ 50℃)							
	VIBRATION	10 ~ 500Hz, 5G 10min./1cycle, 60min. each along X, Y, Z axes							
SAFETY	SAFETY STANDARDS	UL60950-1, BSMI CNS14336-1, EAC TP TC 004 approved							
	WITHSTAND VOLTAGE	I/P-O/P:3KVAC I/P-FG:2KVAC O/P-FG:0.5KVAC							
	ISOLATION RESISTANCE	I/P-O/P, I/P-FG, O/P-FG:100M Ohms / 500VDC / 25℃/ 70% RH							
	EMC EMISSION	Compliance to BSMI CNS13438, EAC TP TC 020							
	EMC IMMUNITY	Compliance to EAC TP TC 020							
OTHERS	MTBF	347.5K hrs min. MIL-HDBK-217F (25℃)							
	DIMENSION	215*115*30mm (L*W*H)							
	PACKING	0.66Kg; 15pcs/10.9Kg/0.78CUFT							

NOTE

1. All parameters NOT specially mentioned are measured at 230VAC input, rated load and 25℃ of ambient temperature.
2. Ripple & noise are measured at 20MHz of bandwidth by using a 12" twisted pair-wire terminated with a 0.1uf & 47uf parallel capacitor.
3. Tolerance : includes set up tolerance, line regulation and load regulation.
4. Line regulation is measured from low line to high line at rated load.
5. Load regulation is measured from 0% to 100% rated load.
6. Length of set up time is measured at cold first start. Turning ON/OFF the power supply very quickly may lead to increase of the set up time.
7. The 150% peak load capability is built in for up to 1 second for 12~48V.LRS-200 will enter hiccup mode if the peak load is delivered for over 1 second and will recover once it resumes to the rated current level(115VAC/230VAC).
8. The ambient temperature derating of 5℃/1000m is needed for operating altitude greater than 2000m(6500ft).
9. This power supply does not meet the harmonic current requirements outlined by EN61000-3-2. Please do not use this power supply under the following conditions:
   a) the end-devices is used within the European Union, and
   b) the end-devices is connected to public mains supply with 220Vac or greater rated nominal voltage, and
   c) the power supply is:
      - installed in end-devices with average or continuous input power greater than 75W, or
      - belong to part of a lighting system

   Exception:
   Power supplies used within the following end-devices do not need to fulfill EN61000-3-2
   a) professional equipment with a total rated input power greater than 1000W;
   b) symmetrically controlled heating elements with a rated power less than or equal to 200W